ISBN 978-82-471-3322-4 (printed ver.)
ISBN 978-82-471-3323-1 (electronic ver.)
ISSN 1503-8181

NTNU
Norwegian University of
Science and Technology

Doctoral theses at NTNU, 2012:30

Muhammad Hamid Rafiq

Experimental Studies and Modeling of Synthesis Gas Production and Fischer-Tropsch Synthesis

Muhammad Hamid Rafiq
Doctoral Thesis

NTNU
Norwegian University of
Science and Technology
Thesis for the degree of
Philosophiae Doctor
Faculty of Engineering Science and Technology
Department of Energy and Process Engineering

NTNU
Norwegian University of
Science and Technology

Doctoral theses at NTNU, 2012:30

NTNU

Muhammad Hamid Rafiq

Experimental Studies and Modeling of Synthesis Gas Production and Fischer-Tropsch Synthesis

Thesis for the degree of Philosophiae Doctor

Trondheim, January 2011

Norwegian University of
Science and Technology
Faculty of Engineering Science and Technology
Department of Energy and Process Engineering

NTNU
Norwegian University of
Science and Technology

NTNU
Norwegian University of Science and Technology

Thesis for the degree of Philosophiae Doctor

Faculty of Engineering Science and Technology
Department of Energy and Process Engineering

ISBN 978-82-471-3322-4 (printed ver.)
ISBN 978-82-471-3323-1 (electronic ver.)
ISSN 1503-8181

Doctoral Theses at NTNU, 2012:30

Printed by Tapir Uttrykk

To Allah We Belong and to Whom We Return,

and to His Most Beloved Person Whom He Sent as a Mercy to the All Worlds

Preface

This thesis is submitted to the Norwegian University of Science and Technology (NTNU) for partial fulfillment of the requirements for the degree of philosophiae doctor.

This doctoral work was carried out between August 2008 and August 2011 at the Department of Energy and Process Engineering under the guidance of Professor Johan E. Hustad, and was financed by the Research Council of Norway and NTNU, Trondheim, Norway.

Abstract

Indirect route can be used to convert abundant natural resources such as natural gas (NG), coal and biomass to synthetic fuels (referred to as gas-to-liquid (GTL), coal-to-liquid (CTL) and biomass-to-liquid (BTL)). It is currently one of the most effective solutions to the problem of finding suitable substitutes for liquid clean fuels. In this work, an investigation on the production of synthetic fuel from gaseous hydrocarbons (HCs)/bio-HCs and liquid bio-HCs on a small-scale unit has been carried out. The research project consists of two major parts, a modified version of a plasma-assisted catalytic partial oxidation (CPO) gliding arc (GlidArc) reactor and a thermally stable single-tube fixed-bed Fischer−Tropsch (FT) reactor.

The potential for the CPO of methane to produce synthesis gas (syngas) was studied both experimentally and thermodynamically at a fixed pressure (1 bar) and electric power (0.3 kW). The investigations were performed in a partially adiabatic plasma-assisted (non-thermal) GlidArc reactor, using a Ni-based catalyst. Two cases were studied: in the first, normal air (molar ratio of O_2/N_2=21/79) was used, whereas enriched air (O_2/N_2=40/60) was utilized in the second. The individual effect of the O_2/CH_4 molar ratio, gas hour space velocity (GHSV) and bed exiting temperature (T_{exit}) was studied for both cases. The main trends of the CH_4 conversion, the syngas (H_2 and CO) yield and the thermal efficiency of the reactor based on the lower heating value (LHV) were analyzed and compared.

A numerical investigation of the CPO of methane to syngas using a GlidArc reactor was also studied. A 2D heterogeneous plug-flow model with radial dispersion and no gradients inside the catalyst pellet are used, including the transport equations for the gas and solid phase and reaction rate equations. The governing equations of this model formed a set of stationary differential algebraic equations coupled with the non-linear algebraic equations, and were solved numerically using in-house MATLAB code. Model results of CPO of methane were compared to previous experimental data with the GlidArc reactor found in the literature. A close match between the calculated and experimental results for temperature, reactant (CH_4 and O_2) conversion, H_2 and CO yields and species mole-fraction were obtained. The developed model was extended to predict and quantify the influence of the GHSV as well as determine the influence of the reactor energy density (RED), the O_2/CH_4 molar ratio and the O_2/N_2 molar ratio. The predicted behaviors for the species mole-fraction, reactants conversion, H_2 and CO yields and temperature along the length of the reactor have been analyzed.

Furthermore, FT synthesis of a model biosyngas (33% H_2, 17% CO and 50% N_2) in a single tube fixed-bed FT reactor was investigated. The FT reactor consisted of a shell and tube with high-pressure boiling water circulating throughout the shell. A spherical unpromoted cobalt catalyst was used with the following reaction conditions: a wall temperature of 473 K, a pressure of 20 bars and a GHSV of 37 to 180 NmL/(g_{cat}.h). The performance of the FT reactor was also validated by developing a 2D pseudo-homogeneous model that includes transport equations and reaction rate equations. Good agreement between the model predictions and experimental results were obtained. This developed model was extended to predict and quantify the influence of the FT kinetics as well as determine the influence of the tube diameter and the wall temperature. The predicted behaviors for CO and H_2 conversion, productivity of HCs (mainly CH_4 and C_5^+) and fluid temperature

along the axis of the reactor have been analyzed.

In addition, the initial tests results are presented for the conversion of waste cooking oil (WCO) to biosyngas by CPO over a granular Ni-based catalyst. Additionally, autothermal reforming (ATR) of propane with water and normal air was also carried out. The investigations were performed in a partially adiabatic plasma-assisted (non-thermal) GlidArc reactor at fixed pressure (1 bar) and electric power (0.3 kW). Detailed axial temperature distributions, product concentrations, reactant conversions, H_2 and CO yield, H_2/CO ratio and thermal efficiency, as a function of the cold and hot WCO flow rate, the water flow rate and the time on stream were studied. Propane and normal air were used as oxidizing components to maintain autothermal operation.

Finally, an investigation of the influence of process conditions on the production of syngas from model biogas (molar ratio of CH_4/CO_2=60/40) through partial oxidation over a granular Ni-based catalyst was explored. The investigations were performed in a partially adiabatic plasma-assisted (non-thermal) GlidArc reactor in a transitional flow regime at a fixed pressure (1 bar) and electric power (0.3 kW). The emphasis of this investigation was on an experimental study and a comparative thermodynamic analysis. The equilibrium compositions were calculated using a Lagrange multiplier and resulted in the development of systems of non-linear algebraic equations, which were solved numerically using the MATLAB function "fmincon". Two cases were studied: normal air (molar ratio of O_2/N_2=21/79) and enriched air (O_2/N_2=40/60). The individual effects of the O_2/CH_4 molar ratio and the T_{exit} were studied in both cases. The main trends of the CH_4 conversion, the syngas yield, the H_2/CO ratio and the thermal efficiency of the reactor were analyzed.

Acknowledgments

Firstly, all praise to Allah Almighty for the blessings and successes He bestowed in my life and career. I always admired His influential saying that:

"And among His signs is the creation of the heavens and the earth, and the diversity of your languages and colors, Verily, in that are indeed signs for those who possess sound knowledge". Al Quran 30:22

I wish to express my sincere gratitude and warmest thanks to my advisor Professor Johan E. Hustad, for his large dedication and enthusiasm for the project. Though I was given freedom to pursue paths I thought best, the door was never closed. I would also like to thank Dr. Farshid Owrang for his contributions regarding the experimental set up and especially for the close cooperation during work on the plasma-assisted gliding arc reactor and single-tube Fischer−Tropsch reactor.

I am also thankful for help and encouragement from Professor Hugo A. Jakobsen, Professor Anders Holmen and Professor Edd A. Blekkan at the Chemical Engineering Department, NTNU. I would further like to express my warmest thanks to Professor Rudolf Schmid at the Department of Chemistry, NTNU. I would also like to thank my office-mates and colleagues from the Department of Energy and Process Engineering, NTNU. It has been inspiring to work with you during the last three years.

The time spent in Trondheim was memorable due to enjoyable company of my Pakistani friends. I would just say, thanks to all of you. Either it was family gatherings, the BBQs or the sports, I enjoyed each of them. I will cherish the moments spent and would wish you best of luck with your careers and life. I would further like to thank my other national and international friends with whom I shared many cultural and travel related experiences.

Pakistan has been through a lot in my life and with my parents and close family back home, sometimes it was difficult to concentrate on work. Still, I am indebted to my parents who were always supportive and encouraging to achieve my career goals. A lot of thanks to my sister and brothers who have been supporting and praying for my well-being and success. My in-laws also deserve special thanks for their continuous support and encouragement throughout my PhD.

Lastly, there are no words to thank my wife Ayesha with whom I started the journey almost simultaneously as the PhD. She has been a pillar of support for me during tough times and always provided objective solutions and suggestions. She's been catered for my duties many times, so I could focus on work.

List of papers

Journal papers

A **M.H. Rafiq**, J.E. Hustad, Synthesis Gas from Methane by Using a Plasma-Assisted Gliding Arc Catalytic Partial Oxidation Reactor, Industrial Engineering Chemistry Research, Volume 50, Issue 9, May 2011, Pages 5428-5439.

B **M.H. Rafiq**, H.A. Jakobsen, J.E. Hustad, Modeling and Simulation of Catalytic Partial Oxidation of Methane to Synthesis Gas by Using a Plasma-Assisted Gliding Arc Reactor, submitted to Fuel Processing Technology.

C **M.H. Rafiq**, H.A. Jakobsen, R. Schmid, J.E. Hustad, Experimental Studies and Modeling of a Fixed Bed Reactor for Fischer−Tropsch Synthesis Using Biosyngas, Fuel Processing Technology, Volume 92, Issue 5, May 2011, Pages 893-907.

D **M.H. Rafiq**, J.E. Hustad, Biosyngas Production by Autothermal Reforming of Waste Cooking Oil with Propane Using a Plasma-Assisted Gliding Arc Reactor, International Journal of Hydrogen Energy, Volume 36, Issue 14, July 2011, Pages 8221-8233.

E **M.H. Rafiq**, J.E. Hustad, Experimental and Thermodynamic Studies of the Catalytic Partial Oxidation of Model Biogas Using a Plasma-Assisted Gliding Arc Reactor, Renewable Energy, Volume 36, Issue 11, November 2011, Pages 2878-2887.

Conference proceedings

- **M.H. Rafiq**, J.E. Hustad, Production of Synthesis Gas by Reforming of Waste Cooking Oil with Propane Using a Plasma-Assisted Gliding Arc Reactor, 19^{th} European Biomass Conference and Exhibition, Berlin, Germany, 6 - 10 June, 2011.
- **M.H. Rafiq**, J.E. Hustad, Conversion of Model Biosyngas to Liquid Hydrocarbons via Fischer-Tropsch Synthesis, 7^{th} European Congress of Chemical Engineering (ECCE-7), Prague, Czech Republic, 28 August - 01 September, 2010.
- **M.H. Rafiq**, J.E. Hustad, Modeling of Single Tube Fischer-Tropsch Reactor Using Model Biosyngas as Reactant, Renewable Energy Research Conference; Trondheim, Norway, 7 - 8 June, 2010.
- **M.H. Rafiq**, F. Owrang, J.E. Hustad, Catalytic Partial Oxidation of Model Biogas Using a Plasma-Assisted GlidArc Reactor, 18^{th} European Biomass Conference and Exhibition, Lyon, France, 3 - 7 May, 2010.

- **M.H. Rafiq**, F. Owrang, J.E. Hustad, Synthesis Gas from Methane by Using Plasma Assisted GlidArc Catalytic Partial Oxidation Reactor, 1st Trondheim Gas Technology Conference, Trondheim, Norway, 21 - 22 October, 2009.
- **M.H. Rafiq**, F. Owrang, F. Guitard, J.E. Hustad, J. Olsson, J. Pedersen, A Preliminary Study of Single Tube Fischer-Tropsch Reactor, 1st International Conference on Polygeneration Strategies, Vienna, Austria, 01 - 04 September, 2009.
- F. Owrang, **M.H. Rafiq**, F. Guitard, J.E. Hustad, POX Steam Reforming in a Plasma-Assisted GlidArc Reformer, 1st International Conference on Polygeneration Strategies, Vienna, Austria, 01 - 04 September, 2009.
- F. Owrang, **M.H. Rafiq**, F. Guitard, J.E. Hustad, Conversion of Low Grade Bio-Oils to Biosyngas Using GlidArc-Assisted POX Reformer, 1st International Conference on Polygeneration Strategies, Vienna, Austria, 01 - 04 September, 2009.

Nomenclature

Latin letters

C_j	Concentration of the j species (kmol/m^3)
C_n	Hydrocarbon number of n component
C_p	Specific heat (J/kg/K)
D_{er}	Effective radial mass diffusion coefficient (m^2/s)
D_j	Diffusivity of the j species (m^2/s)
d_p	Average particle diameter of the catalyst (m)
d_t	Tube diameter (m)
f	Friction factor
h_p	Heat transfer coefficient at the catalyst particle (W/m^2/K)
k_j	Mass transfer coefficient of the j species (m/s)
L	Tube length (m)
M_j	Molecular weight of the j species (kg/kmol)
P	Pressure (bar or Pa)
R	Universal gas constant: 8.314×10^3 (J/kmol/K)
$S_{C_5^+}$	Carbon selectivity of $C_5{}^+$ hydrocarbons (%)
r	Radial position (m)
r_j	Rate of consumption or formation of the j species (kmol/kg$_{\mathrm{cat}}$/s)
r_p	Average particle radius of the catalyst (m)
T	Temperature (K)
T_w	Wall temperature (K)
U	Heat transfer coefficient at the tube wall (W/m^2/K)
u_z	Superficial velocity of the fluid in axial direction (m/s)
w_j	Mass fraction of the j species
y_j	Molar fraction of the j species in the pseudo-phase
z	Axial position in the tube (m)

Greek letters

α	Chain growth probability factor used in the ASF plots
$\Delta\mathrm{H_i}$	Heat of the ith reaction (J/kmol)
ε	Void fraction of the catalyst bed
λ	Thermal conductivity (W/m/K)
μ	Fluid viscosity (Pa.s)
ρ	Density (kg/m^3)

Superscript and subscript

b	Bulk
cat	Catalyst
er	Effective radial parameter
g	Gas
i	The ith reaction
j	Species j
p	Particle
w	Wall at the pseudo side

Abbreviations

ASF	Anderson-Schulz-Flory
bbd	Barrels per day
CFB	Circulating fluidized bed
CPO	Catalytic partial oxidation
DBD	Dielectric barrier discharge
DCM	Dichloromethane
FT	Fischer−Tropsch
GC	Gas chromatograph
FFB	Fixed fluidized bed
FID	Flame ionization detector
GHSV	Gas hour space velocity
GlidArc	Gliding Arc
GTL	Gas-to-liquid
HC	Hydrocarbon
HTFT	High-temperature Fischer−Tropsch
LHV	Lower heating value
LTFT	Low-temperature Fischer−Tropsch
MS	Mass spectrometry
MSR	Microstructured reactors
MW	Microwave
NG	Natural gas
O/C	Oxygen-to-carbon ratio
RED	Reformer energy density
RGA	Residual gas analyzer
SAS	Sasol advance synthol
S/C	Steam-to-carbon ratio
Syngas	Synthesis gas
T_{exit}	Bed exiting temperature
T_{max}	Maximum temperature
WCO	Waste cooking oil
WGS	Water gas shift

Contents

List of Tables

List of Figures

Chapter 1

Introduction

With the development of society, the consumption of fuels is increasing continuously and is likely to double between 2000 and 2050 [1]. In addition, rising crude oil prices have also made natural gas (NG), coal and biomass increasingly attractive feedstocks for synthetic fuels. Indirect conversion of these feedstocks into hydrocarbons (HCs) via Fischer−Tropsch (FT) synthesis, a part of XTL (gas-to-liquid (GTL), coal-to-liquid (CTL) and biomass-to-liquid (BTL)) technology, is currently one of the most promising and environmentally effective solutions to the problem of finding suitable substitutes for liquid clean fuels. These fuels are ultraclean; they contain no aromatics, no sulfur and no nitrogen-containing compounds.

The XTL technology is also regarded as an interesting option for the production of FT diesel fuels from small plants. Small-scale production units offer several advantages; it is a low risk business due to ease of build-up, requires less maintenance cost and have reduced transportation cost of the feed stock.

1.1 Background

A small-scale XTL system consists of four main parts; synthesis gas (syngas) production, gas cleaning and upgrading, FT synthesis and FT product workup. In this section, syngas production and FT synthesis are described on general basis. More details about these two parts are provided in chapter 2 and 3, respectively.

1.1.1 Synthesis gas preparation

Syngas (H_2 and CO) is prepared from a carbonaceous feedstock. The term carbonaceous implies the presence of carbon. The essential requirement is that feedstock contains carbon as well as hydrogen since this will increase the efficiency with which it can be converted to HCs products. If the feed is deficient in hydrogen,

water is used to obtain the hydrogen, which requires the energy to split the water molecules. NG is the most common feed used to prepare syngas for FT synthesis. Thus, most literature for reforming is based on NG as feedstock. In the entire XTL complex, the syngas preparation section is an important one. It is the most expensive of the four processing sections (syngas preparation, gas cleaning and upgrading, FT synthesis and product workup), and is also responsible for the largest part of the energy conversion in the XTL plant [2]. The technology used to prepare the syngas can be separated into two main categories, gasification and reforming. Gasification is used for heavy liquid or solid feedstock, while reforming is used for liquid or gaseous feedstock [2].

Syngas production processes are well established with the processes (i.e. partial oxidation, steam reforming, autothermal reforming (ATR) and dry reforming). Among them, syngas production via the catalytic partial oxidation (CPO) route proceeds through coupled exothermic oxidative reactions and endothermic reforming reactions in the same catalyst bed. This simultaneous occurrence of exothermic and endothermic reactions makes this process attractive since it offers the advantage of vastly reduced energy requirements. These well-established technologies were investigated under different operating conditions in the presence of various catalysts, and it would appear that almost all of the combinations have been evaluated and most of the strategies examined [3]. The shortcomings of the conventional reformers concern size, large investments, limitations on rapid response, the extreme operating conditions that limit the lifetime of a reactor, heat management (during the front end of the catalyst bed as the methane undergoes total oxidation), as well as safety and operability [4]. The alternative novel plasma reforming option could provide original responses to these drawbacks in terms of reactivity, compactness and efficiency. Different paths have been investigated for the last two decades using various plasma technologies and gliding arc (GlidArc) being one of them. In a plasma-assisted CPO GlidArc reactor, an electrical energy is dissipated directly in the process gas through a specific high-voltage discharge [3]. For the simplicity and economics reasons, air is used as an oxidant in CPO GlidArc reactor but it can be upgraded by adding oxygen enriched air to enhance the hydrogen and carbon monoxide content in the syngas.

The oxidation of gaseous HCs/liquid bio-HCs by air or an oxygen enriched air lead to formation of syngas/biosyngas. The reactants conversion, products yield and thermal efficiency of the reactor depends on the air to fuel ratio, composition of the feedstock, temperature and pressure of the reactor as well as the type of the catalyst used.

1.1.2 FT synthesis

The reaction between carbon monoxide and hydrogen on heterogeneous catalysis, yielding HCs and water, was discovered by Franz Fischer and Hans Tropsch in

1923 [6]. The FT reaction is a polymerization of carbon monoxide, and the products are paraffins and olefins with small proportion of oxygenates. The product distribution depends on the type of catalyst, and the process parameters such as temperature, pressure, residence time, etc.

The FT synthesis can be carried out at a low or high temperature, at low temperature higher HCs are formed. In general, the FT reaction is highly exothermic, and the average heat released per $(-CH_2-)$ formed is higher than the typical catalytic reactions used in the oil refining industry. This heat should be removed from the system by isothermal operation. The N_2 presence in the syngas plays a significant role in removing a large amount of heat generated by the exothermic FT reaction and in promoting the formation of diesel [6]. Jun et al. [7] and Lapidus et al. [8] have shown that most FT synthesis studies use pure syngas in reaction mixtures, and only limited papers studied the influence of reaction conditions on the productivity and selectivity in FT synthesis using a biosyngas mixture.

Fixed bed vs. Slurry bed

Various types of reactors, including fixed-bed, fluidized bed, ebullating bed and slurry phase, are used to efficiently control the heat produced by the FT reaction. A fixed-bed reactor is an appealing technology due to such attractive features as the absence of the requirement to separate the catalyst from the product and the ease of scale-up from a single tube to a pilot plant [9]. When a model that fits a single-tube reactor is developed, it is possible to implement it to a large-scale multi-tubular reactor containing thousands of tubes. A difficulty with this type of reactor is to get sufficient heat removal from the tubes due to the exothermic process (temperature runaway). On the other hand, it is easier to remove the heat from slurry reactors. However, one major drawback with slurry reactors is that impurities in the feedstock can deactivate the whole catalyst mass, whereas, for fixed-bed reactor only the upper part of the catalyst is deactivated and the rest of catalyst bed remains unaffected. So, it is more economical to use slurry phase reactors with pure syngas [10]. In addition, slurry reactors are relatively too large and have twice the volume of a fixed-bed reactor for same operating conditions [10]. Additionally, they are too expensive and required qualified technicians for maintenance [10]. Therefore, slurry reactors are not suitable for small-scale FT plants.

1.2 Specific objectives

The aim of this thesis is to investigate the potential of a small-scale research plant for the production of synthetic fuel from gaseous HCs/bio-HCs and liquid bio-HCs. The thesis consists of two main parts: (1) a modified version of a patented plasma-assisted CPO GlidArc reactor for producing syngas/biosyngas by using different types of gaseous HCs/bio-HCs and liquid bio-HCs feed stocks and (2) a thermally stable single-tube fixed-bed FT reactor for achieving practical experience of

producing liquid fuel from produced syngas/biosyngas. Within this context, the present thesis aims to contribute to fundamental insights into:

- Production of syngas/biosyngas from different types of gaseous HCs/bio-HCs and liquid bio-HCs by using a plasma-assisted GlidArc reactor.
- Modeling and simulation of plasma-assisted CPO GlidArc reactor.
- Production of synthetic fuel by using a fixed-bed reactor for FT synthesis.
- Modeling and simulation of fixed-bed FT reactor.

1.3 Outline

The thesis comprises six chapters and five journal publications. The outlines of the chapters are as follows:

Chapter 2: It gives a technical background and discusses the technologies available for syngas production, specifically from reactor aspects. Further various plasma technologies are discussed. Finally the advantages of combined plasma and catalysts technology in fuel reforming are highlighted.

Chapter 3: It is a FT synthesis literature review. Since the research on FT synthesis is enormous, only a brief introduction of FT synthesis and different types of FT reactors are presented.

Chapter 4: It provides all the essential information for reproduction of experimental work for both plasma-assisted CPO GlidArc reforming system and fixed-bed FT synthesis setup. Further, an outline of the modeling framework is given with a procedure for solving the models.

Chapter 5: This is the main chapter representing the results from plasma-assisted CPO reforming and fixed-bed FT synthesis.

Chapter 6: It provides overall conclusions of the thesis and addresses unsolved issues and gives an outlook on future work.

The lists of five journal publications are provided as appendices.

Paper A: In this study, a plasma-assisted GlidArc reactor with a combination of catalysts is used to reform CH_4 with the aim of finding the conditions to give an H_2/CO ratio of 2.

Paper B: The aim of this study is to propose a 2D heterogeneous model for a CPO GlidArc reactor using intrinsic kinetics of a Ni-based catalyst. The model is validated with the previously reported, experimentally measured temperature profiles, together with data collected at the reactor exit reported in paper A. Finally, parametric sensitivity analysis with detailed numerical simulations are performed to

determine the effect of various parameters and to develop a good understanding of the behavior of the CPO GlidArc reactor system.

Paper C: The initiative of this study is to run the fixed-bed reactor with a model biosyngas at different GHSVs by keeping all other operating parameters constant. The modeling work is also performed, and the results of the simulations are compared and validated with the experimental work. Finally, parametric sensitivity analysis with detailed numerical simulations are performed to determine the effect of various parameters and to develop a good understanding of the behavior of the fixed-bed FT synthesis system.

Paper D: The purpose of this work is to investigate the production of biosyngas by the direct catalytic reforming of waste cooking oil (WCO) in the presence of propane and air. First, tests with propane using water is performed to find a maximum amount of water flow rate, suitable for stable operation and soot free syngas formation, after that the maximum amount of cold and hot WCO flow rate is found to obtain the same objective. It represents the operating capacity of the GlidArc reactor for water and WCO flow rates.

Paper E: Specifically, this work investigated the effects of process conditions upon syngas production from model biogas. Two cases are studied: (i) normal air (O_2/N_2 = 21/79) and (ii) enriched air (O_2/N_2 = 40/60). The oxygen addition from normal air/enriched air hinders the deposition of carbon on the Ni-catalyst surface. The individual effect of the operating parameters, such as the O_2/CH_4 molar ratio and the T_{exit}, is studied for both cases.

Chapter 2

Synthesis gas

Syngas, a mixture of carbon monoxide and hydrogen, is an important intermediate for various synthesizing chemicals and environmentally clean fuels, such as ammonia, methanol, methyl formate, acetic acid, dimethyl ether (DME), and methyl-tert-butyl ether (MTBE) and for the increasingly important production of synthetic liquid fuels by FT synthesis and similar processes [11]. Syngas with the desired composition ranging from the 3:1 mixture of hydrogen and nitrogen used for production of ammonia to the 1:1 mixture of hydrogen and carbon monoxide is preferred for production of DME, acetic acid or methyl formate [12]. Syngas can be produced from NG, petroleum coke, naptha, residual oil, coal and biomass, and even from organic wastes. Though significant quantities of syngas are being made from coal [13], NG is the largest source of syngas at present and its use for this purpose is growing because of its lowest cost routes and good environment performance [14]. In the recent years, the interest in the conversion of biomass derived resources to syngas and bio-oils has been increasing. These resources are currently being recognized as attractive options due to their renewable, reliable and CO_2-neutral features.

There are several processes available for syngas production depending on the feed stock, such as steam reforming, partial oxidation, autothermal reforming (ATR), gasification and a combination of them, which result in different H_2/CO ratio.

2.1 Steam reforming

Steam reforming is the conversion of HCs with steam into a mixture of carbon monoxides, hydrogen, methane and unconverted steam. Steam reforming is carried out in several different types of reactors. Each of these may be optimized for specific applications [12]. The reactions taking place for the steam reforming process are given in Table 2.1 along with the enthalpy of reaction. Reaction 1 (R1) and 3 (R3) in Table 2.1 are the steam and CO_2-reforming reactions, respectively, for methane and reaction 2 (R2) is the water gas shift (WGS) reaction, which takes

place simultaneously. Reaction 4 (R4) is the steam reforming reaction of higher HCs. The enthalpy is given for steam reforming of *n*-heptane [12].

Table 2.1: Key reactions in steam reforming [12].

Reactions	Reaction description	Standard enthalpy of reaction ($\Delta_R H^o_{298}, kJmol^{-1}$)	
$CH_4 + H_2O \rightleftharpoons CO + 3H_2$	Steam reforming	206	R1
$CO + H_2O \rightleftharpoons CO_2 + H_2$	WGS	-41	R2
$CH_4 + CO_2 \rightleftharpoons 2CO + 2H_2$	CO_2 reforming	247	R3
$C_nH_m + nH_2O \rightleftharpoons nCO + (n + m/2)H_2$	Higher HCs steam reforming	1175[a]	R4

[a]For *n*-C_7H_{16}.

The overall steam reforming is highly endothermic and it is carried out at high temperature (1173 K) and at pressure between 15 and 30 bar [15] over a Ni/Al_2O_3 catalyst [16]. However, higher H_2/CO ratio comes at the expense of high temperature requirements; methane is the most stable HC and requires energy input to react with steam. Methane steam reforming is thermodynamically favored at high temperatures and at high molar steam-to-carbon (S/C) ratios in the feed. Thermodynamic predictions estimate 90% methane conversion at ca. 923 K, 1 bar and at a S/C ratio of 3, and complete conversions are estimated at temperatures in excess of 1073 K [17]. Steam can be partially substituted by carbon dioxide to perform CO_2-reforming reaction (R3). This reduces the H_2/CO ratio in the product gas, which in cases may be more economical, especially if a source of low-cost carbon dioxide is available. Steam (and CO_2) reforming is always accompanied by the WGS reaction (R2) which is generally fast and may be considered in equilibrium at most conditions [2]. However, low S/C ratios lead to high methane concentration in the outlet. To compensate this, a higher temperature can be used [18]. In addition, carbon formation is a challenge in steam reforming processes. The potential for carbon formation is highest when S/C ratio is lower or under CO_2-reforming. In steam reforming processes carbon formation is avoided through proper design of the catalyst and specific process conditions [12].

Steam reforming can be described by a first-order reaction, irrespective of pressure. At high temperatures the overall rate can be limited by pore diffusion, but at lower temperatures the molecular diffusion rate is much higher than the reaction rate so that the catalyst activity can be fully used [19]. The overall rate in steam reforming is typically limited by the rate of heat transfer through the tubes, the rate of heat transfer through the gas film surrounding the catalyst pellets and mass transport restrictions including film and pore diffusional effects. The commercial Ni-catalysts are often in the form of thick walled Raschig rings, with 16 mm in diameter and height, and a 6-8 mm hole in the middle. If the heat load per unit area is too high, the limits of such catalyst will be reached, and hence small particles

will be necessary in order to make use of more of the catalyst. Smaller particle will however lead to increase pressure drop [19].

2.2 Catalytic partial oxidation

The production of syngas based on heterogeneous catalytic reactions is normally referred to as CPO. The principle of CPO is illustrated in Fig. 2.1. The HC feed and the oxidant are mixed in an inlet zone upstream the catalyst bed. Syngas production via the CPO route proceeds through coupled exothermic oxidative reactions and endothermic reforming reactions in the same catalyst bed. This simultaneous occurrence of exothermic and endothermic reactions makes this process attractive since it offers the advantage of vastly reduced energy requirements. Possible reactions for methane CPO are summarized in Table 2.2:

Table 2.2: Reactions in the HC partial oxidation system [20].

Reactions	Reaction description	Standard enthalpy of reaction ($\Delta_R H^o_{298}, kJmol^{-1}$)	
$CH_4 + 2O_2 \rightarrow CO_2 + 2H_2O$	Combustion	-802.6	R5
$2CH_4 + O_2 \rightarrow 2CO + 4H_2$	Partial oxidation	-71.4	R6
$CH_4 + O_2 \rightarrow CO_2 + 2H_2$		-318.6	R7
$CO + H_2O \rightleftharpoons CO_2 + H_2$	WGS	-41	R2
$CH_4 + H_2O \rightleftharpoons CO + 3H_2$	Steam reforming	206	R1
$CH_4 + CO_2 \rightleftharpoons 2CO + 2H_2$	CO_2 reforming	247	R3
$CO + H_2 \rightleftharpoons C + H_2O$		-131.3	R8
$CH_4 \rightleftharpoons C + 2H_2$	Methane decomposition	74.9	R9
$2CO \rightleftharpoons CO_2 + C$	Boudouard	-172.4	R10
$2CO + O_2 \rightleftharpoons 2CO_2$	Oxidation of CO	-566	R11
$2H_2 + O_2 \rightleftharpoons 2H_2O$	Oxidation of H_2	-483.6	R12

Partial oxidation reaction (R6) in Table 2.2 can be seen as an example of direct route to syngas, and the question of whether it is possible to catalyze only R6 has been a keynote in the research on methane partial oxidation. Considering only R6, it is theoretically possible to produce pure syngas at all temperatures where methane and oxygen are activated. It is, however, typically observed that the remaining 10 overall reactions (R1-R3, R5, R8-R12) in Table 2.2 play important roles in the CPO of methane and the product composition is therefore governed by or limited by the global thermodynamic equilibrium of all possible species [20]. In the indirect mechanism, at the top of the bed, all oxygen is consumed by the exothermic reaction with a portion of the methane in the feed. This region can be on the order of 10% of the total bed and is controlled by the O/C ratio and temperature. A temperature spike as well as localized hot spots promotes the formation of combustion products. The remaining methane is converted in the bottom portion of the catalyst bed

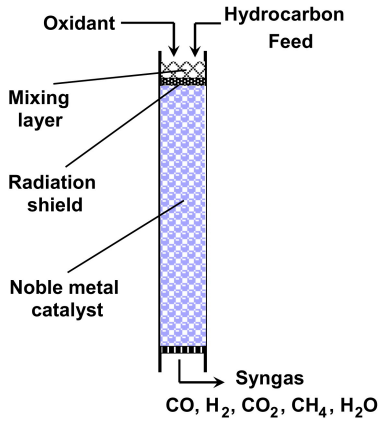

Figure 2.1: CPO principle [12].

through endothermic secondary reforming reactions with the unreacted methane and water produced in the first region [21]. Gas compositions indicating higher conversions than thermodynamic equilibrium most likely reflects the temperature of the catalyst.

CPO has been investigated extensively for many years. Before 1992, most studies were carried out at moderate or low-space velocities at a residence time of 1s or above [22]. However, during the later years CPO has been carried out at least in the laboratory at very short contact times between 0.1 and 10 ms in some cases without preheating the feedstock and with no steam addition. Additional information regarding research, mainly of fundamental nature, can be found for example in a series of paper by L.D. Schmidt and co-workers [[23],[24],[25],[26],[27]]. Both air and oxygen may in principle be used as oxidant in a CPO reactor. Experiments with CPO and air as oxidant have been conducted at the Topsoe pilot plant in Huston, Texas. In all cases, the methane conversion corresponds closely to the equilibrium of the methane steam reforming reaction [12]. Another feature of CPO is related to the start-up period which requires pre-mixing of HC-oxygen mixtures at high temperatures, which calls for careful selection of operating and design parameters to suppress the risk of possible explosions [28].

2.3 Autothermal reforming

ATR has received a considerable attention. Lower capital cost, relative compactness, greater potential for economies of scale and its flexibility with respect to the product composition made ATR a very good alternative to steam reforming [29]. From last decades, hydrogen-rich and carbon monoxide-rich syngas has been produced using ATR. Autothermal reformers were used to produce synthesis gas for

ammonia production and methanol in 1950s and 1960s [12]. Low S/C ratio is beneficial for the production of carbon monoxide-rich syngas as feed for e.g., methanol or FT synthesis. S/C operation with a ratio of 0.6 has been demonstrated on pilot [[29],[12]] and industrial scale [12]. ATR is an adiabatic reactor where combined combustion and catalytic process is carried out as illustrated in Fig. 2.2. The ATR reactor consists of a burner, a combustion chamber and a catalyst bed, all of which are contained in a refractory lined pressure shell.

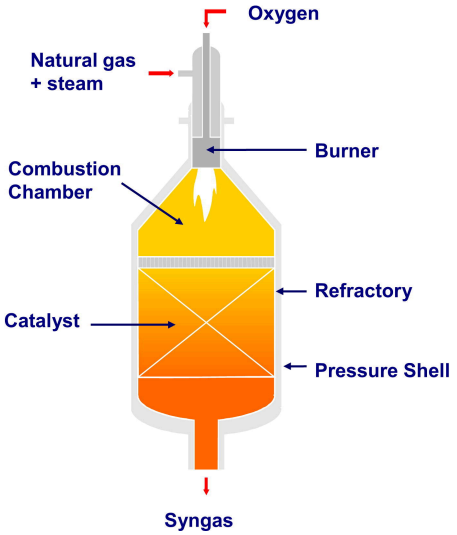

Figure 2.2: Illustration of an ATR reactor [30].

NG and steam mixture is partially converted by pressurized combustion in the combustion chamber under fuel-rich conditions. The temperature is about 1100-1300 °C in the combustion chamber near the catalyst bed and more than 2500 °C [12] in the flame core depending upon the process conditions. Due to high temperature, steam reforming and WGS reactions also take place non-catalytically in the combustion chamber. Practically, a lot of chemical reactions take place in the combustion chamber including radicals and combustion reactions. General reactions which are often used to represent the combustion chamber are shown in Table 2.3.

Table 2.3: Simplified reactions in the combustion chamber of ATR [12].

Reactions	Reaction description	Standard enthalpy of reaction ($\Delta_R H^o_{298}, kJmol^{-1}$)	
$CH_4 + 3/2O_2 \rightarrow CO + 2H_2O$	Combustion	-519	R13
$CH_4 + H_2O \rightleftharpoons CO + 3H_2$	Steam reforming	206	R1
$CO + H_2O \rightleftharpoons CO_2 + H_2$	WGS	-41	R2

Combustion reactions quantitatively consume the oxygen. However, the methane conversion is incomplete in the combustion chamber and final conversion takes place in the catalyst bed according to described reactions (R1) and (R2) in Table 2.3. The syngas is at chemical equilibrium and leave the ATR reactor typically around 850-1100 °C [12]. There are three zones in the reactor: (a) combustion zone, (b) thermal zone and (c) catalytic zone. Mixing and burning of the feed streams take place in a turbulent diffusion flame in combustion zone. "Mixed is burnt" principal is valid, since the combustion reactions are exothermic and very fast. Combustion is sub-stoichiometric with overall oxygen to HC ratio of 0.55-0.6 in ATR but presented as a one-step model in a simplified way. Single reaction of CH_4 to CO and H_2O with an O_2/CH_4 ratio of 1.5 (reaction (R13) in Table 2.3) take place in the flame zone. The local stoichiometry will vary from very fuel-lean to very fuel-rich in the flame zone [12]. The conversion of HCs takes place via homogeneous gas-phase reactions in thermal zone. Homogeneous gas-phase steam methane reforming and shift reaction (R1 and R2 in Table 2.3) are the main overall reactions taking place in the thermal zone. The methane steam reforming reaction (R1) does not proceed to equilibrium in the thermal zone [12]. HCs are finally converted via heterogeneous catalytic reactions in fixed-bed catalytic zone. Gas mixture will be in equilibrium with respect to steam methane reforming (R1) and shift reaction (R2) at the exit temperature and pressure of the catalytic zone. ATR operation is soot-free under normal circumstances. The fuel rich combustion takes place in a turbulent diffusion flame and intensive mixing is required to prevent soot formation. The exit gas contains only methane as HC. Soot formation is avoided which would reduce the carbon efficiency of the process whereas soot particles would need to be removed from the syngas [12].

2.4 Gasification

Gasification is one of the most promising technologies for converting coal and biomass into an easily transportable and usable fuel. Transformation of biomass fuels into high quality energy carriers and other commercial products can be efficiently achieved via either biological or thermochemical processes [31]. Among various biomass conversion technologies within thermochemical and biochemical platforms, biomass gasification has received the highest interest since it offers high conversion efficiency and significant environmental benefits. In addition, it also increases options for combination with various high efficiency power generation systems using gas engines, gas turbines and fuel cells. Gasification is the formation of syngas from carbonaceous materials like coal and biomass by reaction with a gasifying agent like H_2O, H_2 or CO_2 [[15],[32],[33]]. The main gasification reactions are endothermic and the heat required to sustain the gasification is typically supplied by combustion of part of the carbonaceous material (so-called autothermic gasification) [15]. In the known processes converting solid, carbonaceous feedstocks into fuel chemicals, the

production and conditioning of the syngas does in fact constitute the dominant part of the plant cost. For the production of synthetic diesel fuel from coal in the FT process, the systems for syngas production entering the reactor compose 70% of the plant investment cost [2]. Tables 2.4 and 2.5 summarize, respectively, the dominant heterogeneous and homogeneous reactions taking place in the gasifier.

Table 2.4: Major heterogeneous reactions taking place in the gasifier [[15],[32],[33],[34]].

Reactions	Reaction description	Standard enthalpy of reaction ($\Delta_R H^o_{298}, kJmol^{-1}$)	
$C + CO_2 \rightleftharpoons 2CO$	Reverse boudouard	172.4	R14
$C + H_2O \rightleftharpoons CO + H_2$		131.3	R15
$C + 2H_2 \rightleftharpoons CH_4$	Methane formation	-74.9	R16
$2C + O_2 \rightleftharpoons 2CO$	Oxidation of CO	-221	R17
$C + O_2 \rightleftharpoons CO_2$	Coke gasification/oxidation of CO	-393.6	R18

Table 2.5: Major homogeneous reactions taking place in the gasifier [[15],[32],[33],[35]].

Reactions	Reaction description	Standard enthalpy of reaction ($\Delta_R H^o_{298}, kJmol^{-1}$)	
$2CO + O_2 \rightleftharpoons CO_2$	Oxidation of CO	-566	R11
$2H_2 + O_2 \rightleftharpoons 2H_2O$	Oxidation of H_2	-483.6	R12
$CO + H_2O \rightleftharpoons CO_2 + H_2$	WGS	-41	R2
$CO + 3H_2 \rightleftharpoons CH_4 + H_2O$	Methanation/hydrogenation	-206	R19
$CH_4 + 2O_2 \rightarrow CO_2 + 2H_2O$	Combustion	-802.6	R5

For the reactions in Table 2.4 the carbonaceous material is simply represented as "C". In addition to the reactions in Tables 2.4 and 2.5, thermal gas phase cracking of tar (larger HCs) and small HCs will also occur in the reactor [[33],[32]]. These cracking reactions will to some extent be facilitated by the gasification agent [[33],[32]]. During biomass gasification, several parameters such as gasifier type, reaction temperature, biomass fuels properties, bed materials and gasifying agent have a substantial influence on product gas composition, carbon conversion efficiency and tar formation.

The reactors used for biomass gasification are quite diverse of which the design ultimately determines other parameters such as gasification temperature and the properties of the biomass used [36]. The most important gasifier types are: (a) fixed-bed (updraft or downdraft fixed-beds), (b) fluidized bed and (c) entrained flow gasifiers.

Fixed-bed gasifiers have been in use since the beginning of the gasification industry. Somewhat confusingly, these gasifiers are sometime also referred to as moving

bed gasifiers. The solid feed moves downward through gasifiers but the various zones within the gasifiers are "fixed" in locations. These gasifiers have maintained a strong position in the broad range of reactor types used for coal gasification [2]. They are suitable for small scale applications and generally operated at temperature around 1000 °C [37]. The size of the fixed-bed reactors are below 1 MW in most designs. Increasing the reactor diameter might cause problems in establishing the required high temperature zones to crack the tar content in the product gas [38]. These reactors are further classified according to the flow direction of the gasification agent into updraft, downdraft and crossdraft gasifiers.

Fluidized bed gasification has been used for coal gasification for many years [37] and is regarded as the best design option for biomass gasification. Therefore, current development activities on large scale biomass gasification have been mainly devoted to fluidized bed technologies, since fluidized bed gasifiers have excellent heat and mass transfer between the gas and solid phases with the best temperature distribution and they meet the challenges of wide variations in fuel quality with a broad particle size distribution. The gasifying agents for fluidized bed biomass gasification can be either air, steam, pure oxygen or their combination [39]. Air is the mostly used agent nowadays at demonstration or commercial scale because of its extensive low-cost availability. However, the product gas from fluidized bed air-blown biomass gasification normally containing 50 vol.% N_2 has a low heating value (4-7 MJ/Nm^3) and it can be used only for electricity production or heat generation [40]. Steam gasification can produce a medium calorific value gaseous fuel (10-14 MJ/Nm^3) with relatively high hydrogen content and this has been deeply studied experimentally by many researchers [[41],[42]]. However, steam gasification is a more complex endothermic process, which requires heat input as the heat necessary to the process is not directly supplied by the partial combustion of the feedstock during the gasification process at temperatures in excess of 800 °C. One easy way for supplying heat is to add some air or oxygen to the gasifier, so that an autothermal gasification process can be achieved [[39],[44],[45],[46]]. However, due to the high price of the oxygen, the product gas distribution under different operating conditions for steam/oxygen mixtures as oxidizer has been less studied. Gil et al. [39] pointed out that the concentration of hydrogen in the raw gas ranges between 14 and 30 vol.% depending on the operational conditions. Lv et al. [44] generally reported that a higher reactor temperature, proper oxygen to biomass stoichiometric ratio, steam to biomass ratio and smaller biomass particle size will contribute to increase the hydrogen production. Siedlecki et al. [46] reported that the use of magnesite as bed material can significantly increase the concentration of hydrogen compared with normal sand as bed material.

The entrained flow type of gasifiers is the most widely used design [2]. The gasifiers are co-current, plug flow reactors. Finely ground feed, in the case of solids, or liquid feed is introduced into the gasifier along with the oxidant and steam or liquid water as moderator. Coal/biomass and gases flow co-currently at high speed. As a result, very short gas residence times are experienced, and the gasification

yields high temperatures in the gasifiers (1600-2200 K). The coal/biomass has to be pulverized at high temperatures to ensure high carbon conversion. Zhou et al. [47] reported that higher temperature favored H_2 and CO production and an introduction of oxygen to the gasifier improved the carbon conversion, but lowered the H_2/CO ratio of the syngas. However, according to Higman and Van der Burgt [32], entrained-flow gasifiers generally operated at high temperature, therefore requiring a very small biomass particle size of 100 μm or less to promote mass transfer and high oxygen for maintaining operation temperature. In addition, the fuel feeding allows for high pressure gasification and large capacities (> 100 MW). All entrained flow gasifiers are of the ash slagging type [2]. Typical operating parameters of these gasifiers are provided in Table 2.6.

Table 2.6: Comparison of typical operating conditions for the 3 three types of gasifiers, used for coal gasification [[15],[32],[33],[48]].

Type	Pressure (bars)	Reactor temp. (K)	Exit temp. (K)	O_2 addition (kg/kg coal)	Particle diameter (mm)	Ash condition
Moving bed[a]	25-30	1250-1350	700	0.5	20-50	Dry/slagging
Entrained flow	20-40	1600-2200	1300	0.9	<0.1	Slagging
Fluidized bed	10-30	1250-1400	1150	0.7	<.5−6	Dry/ agglomerating

[a]Counter current operation.

2.5 Plasma reforming

The above-mentioned well-established processes were investigated under different operating conditions in the presence of various catalysts, and it would appear that almost all of the combinations have been evaluated and most of the strategies examined [3]. The shortcomings of the conventional reformers concern size, large investments, limitations on rapid response, the extreme operating conditions that limit the lifetime of a reactor, heat management (during the front end of the catalyst bed as the methane undergoes total oxidation), as well as safety and operability [4]. The alternative novel plasma reforming option could provide original responses to these drawbacks in terms of reactivity, compactness, and efficiency. Recently, plasmas have been investigated for their potential to exhibit catalytic effects primarily because of complex interactions of their excited species (electrons, ions, radicals) in fuel conversion reactions. Some evidence has been found for the plasma catalysis effect in lowering the required ignition temperatures for combustion systems [49]; however, more work is needed to elucidate the catalytic effects in fuel-rich syngas production systems [50].

Plasma is often described as the fourth state of matter and this refers to the chemical, thermal or electrical breakdown of a gas, often forming a luminous ionized

state comprised of a mix of particles: positive and negative ions, electrons, radicals and neutral gas atoms and molecules [50]. Plasma reforming is electrically assisted reforming of fuel in which electrical energy is dissipated directly in the process gas through a specific high-voltage discharge [51]. Depending on the energy, temperature and ionic density, plasma reactors are classified as thermal or non-thermal (cold). A thermal plasma in a local thermodynamic equilibrium has an electron temperature (>10,000 K) in each small volume of plasma that is equal to the gas temperature, excluding the radiation temperature. In a non-thermal plasma, the electron temperature is not in the local thermodynamic equilibrium, and the electrons can reach a temperature of 10^4 to 10^5 K, while the temperature of the gas can be as low as room temperature (300 to 3000 K) [[52],[53]].

Different paths have been investigated for the last two decades using various plasma technologies such as gliding arc [[54],[55],[56],[57],[58]], dielectric barrier discharge (DBD) [[52],[59]], corona [53] and microwave (MW) [[60],[61],[62]] to reform HCs such as methane [[4],[55],[63],[64],[65]], diesel [66] and bio fuels [[54], [67], [68], [69]].

2.5.1 Dielectric barrier discharge

The DBD is a well known type of non-thermal plasma discharge. It is commonly used to generate the low-temperature plasma at atmospheric pressure, which has been successfully used to many industrial processes related to the surface treatments of materials such as polymers and textiles [70], ozone generation [71] and air sterilization in heating, ventilation and air conditioning (HVAC) systems [72]. In addition, some recent publications discuss the influence of DBD on pure methane [73] and mixtures of methane with air, oxygen [74] and carbon dioxide [75], and aim mainly on the production of syngas, methanol or higher HCs. Furthermore, some basic studies dealing with methane steam reforming using DBD have been performed [76].

DBD plasmas have a layered electrode structure in which two metal electrodes are separated by a thin layer of dielectric material, often made from ceramic, quartz, or glass (Fig. 2.3). The dielectric barrier acts to limit current flow once the plasma discharge is ignited and prevents the discharge from transitioning into a plasma spark, which can result in much higher gas temperatures, shock waves and noise. DBD plasmas typically operate with either an AC frequency (0.5-500 kHz) or in a pulsed DC mode and most often have a non-uniform, filamentary structure consisting of a series of micro discharges. DBD plasmas are often used in basic research studies because they are weakly ionized, yet strongly non-equilibrium, and are relatively easy to construct [50].

The conversion of reactants was reported low and also the selectivity of the main products such as carbon monoxide and hydrogen was low compared to the

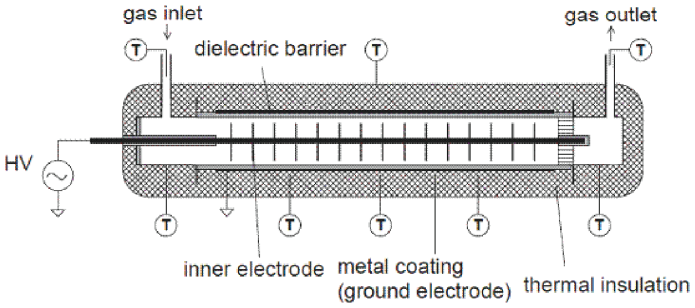

Figure 2.3: Dielectric barrier discharge plasma [85].

conventional catalysis method [[74],[77],[78]] This is mainly because of their low power density due to their limited current and low gas temperatures. Since CPO and steam reforming reactions require an elevated initial temperature to proceed (800-1100 K), non-thermal DBD systems usually require additional energy to be spent for reactant preheating in order to be effective. In addition, the irregular structure of DBD plasmas is not ideal for uniform gas treatment within fuel conversion systems [50]. However, many reports showed that the discharge can effectively lower the temperature range of the optimum catalyst performance [[79],[80],[81],[82],[83],[84]].

2.5.2 Corona discharge

The corona discharge is another type of strongly non-equilibrium, yet weakly ionized plasma that can be found in nature during electrical storms near sharp edges, points, or thin wires (i.e., near regions of high electric field strength) [50]. They are actively studied in connection with their possible use for various plasma chemical applications such as ozone generation from air and oxygen, removal of toxic agents from flue gases and polluted air [86].

Corona discharge (Fig. 2.4) is an inhomogeneous discharge with low current density [87]. It could be generated at atmospheric pressure and has high electric field intensity for ionizing or decomposing feed gas particles. Corona discharge usually involves two asymmetric electrodes; one high curvature, such as a small diameter wire or even a sharp tip and the other low curvature, such as a plate or a cylinder. When a voltage applied exceeds a certain value, the electric breakdown is caused near the high curvature electrode locally, and the corona discharge is brought on. The electron temperature of corona plasma is in the range of 3.5-5 eV while the gas temperature is less than 400 K and the electron density is about 10^{15}-10^{19} m^{-3} [88]. However, high electron density mainly occupies the region around the high curvature electrode. The corona discharge can become unstable if additional voltage or current is applied causing breakdown between electrodes and forming a strong

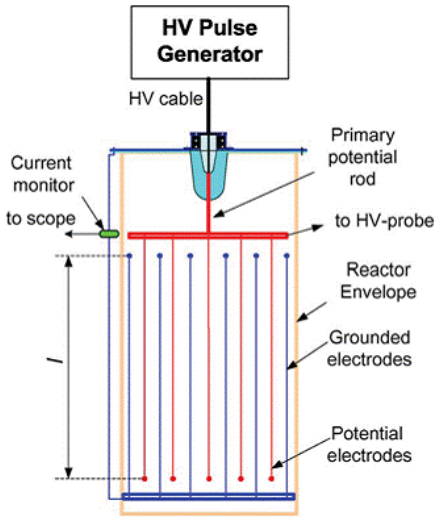

Figure 2.4: Schematic diagram of corona discharge reactor [89].

plasma channel, known as a spark. Spark formation should be avoided because it causes local overheating of the gas as well as non-uniformity of treatment, which is undesirable for many applications [50].

2.5.3 Microwave discharge

MW discharges offer significant advantages as plasma sources. When properly designed, they are very stable and the efficiency of MW power transfer to plasma can achieve almost 100%. They allow obtaining plasmas of high purity. As a rule, MW plasmas are characterized by high density of electrons and active species, such as ions and free radicals [90]. Due to these features MW plasmas find applications in spectroscopy, technological processes like surface treatment, carbon nanotubes synthesis and sterilization [91]. Special interest find MW discharges in different kind of gas processing, such as purification of gases, abatement of gases containing fluorinated compounds, decontamination of chemical warfare agents [92].

Fig. 2.5 shows the configuration of MW plasma reactor. These reactors have the unique advantage that the plasma does not need to be in direct contact with the electrodes. Electrode-less operation is often preferred for extremely high temperature reforming applications because it can eliminate the need for complicated electrode cooling. Initiating high-frequency plasmas is more challenging than DC plasmas because they require complex and somewhat more expensive power supplies that include a high frequency generator. More importantly, the plasma must be coupled and matched as a load in the power circuit [50]. In MW plasmas, the

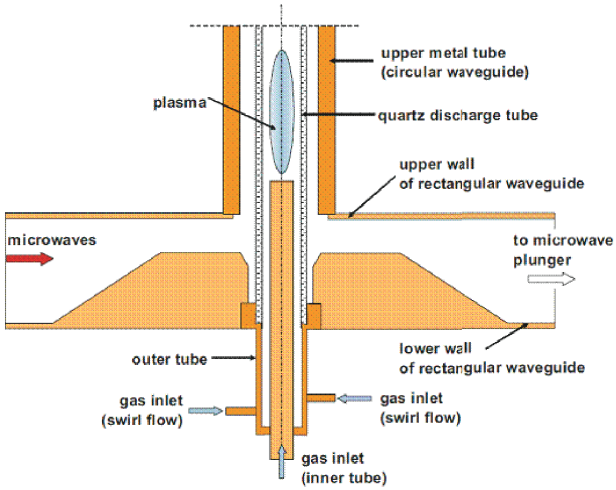

Figure 2.5: Schematic diagram of microwave plasma reactor [92].

wavelengths are very small, on the order of centimeters and approach the dimensions of the reactor itself. Often, waveguides are used to collect and concentrate the electromagnetic waves within the reactor. Not all of the wave power is dissipated in the discharge, however; typically about half is absorbed, a quarter of it is transmitted through the discharge and another quarter is reflected. The benefit of using complex discharges, such as MW plasmas, is that the high degree of coupling between the electromagnetic field and the discharge creates conditions that are strongly non-equilibrium with a high degree of ionization. This is much better than the other non-thermal plasmas, where energy density is low and ionization is weak, with only a small fraction of high energy electrons created. MW plasmas can be operated in a wide range of pressures from milliTorr to near atmospheric; however, at higher pressures, the discharge tends to contract and behave similar to thermal plasma [50].

2.5.4 Gliding arc discharges

The principle of the GlidArc discharge was was developed by Czernichowski [3]. It (Fig. 2.6) consists of two or more diverging metallic electrodes. The electrical arc form between the two knives is powered by a single-phase transformer; the discharges are formed at the closest points of the electrodes, had a very short contact time and are spread by gliding along the edges of the electrodes. The arc disappears at the end of the knives and a new discharge immediately re-formed at the initial locations. The high-voltage, self-maintained discharges struck directly across the gas flow. The electrodes are not cooled, so all of the electrical energy is directly and completely

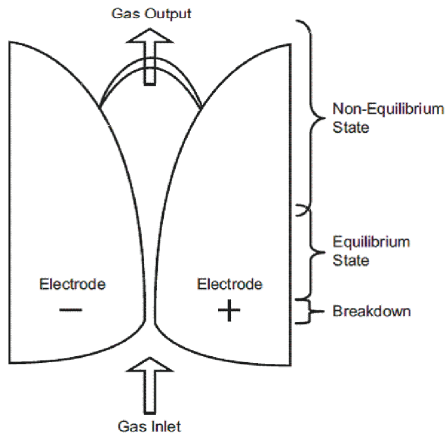

Figure 2.6: Schematic of the planar gliding arc showing how the discharge is pushed and elongated by the gas flow, causing a transition from equilibrium to non-equilibrium state [50].

transferred to the processed gas.

2.6 Advantages of plasma-catalytic process in fuel reforming system

In general terms, plasma reactors without catalysts have lower performances than catalytic reactors, which can be explained by the early stage of research on non-thermal plasma reforming. More complementary studies have been performed and have shown that these technologies are able to achieve performances comparable to catalytic reforming technologies [142]. As a new technology, the plasma-catalytic process has been widely applied for volatile organic compounds removal [94] and HC reforming for hydrogen production [95]. Czernichowski [3] studied plasma reforming of heavy NG by using inert ceramic particles in the post-plasma zone and the results revealed that quite a bit of ethylene and acetylene was produced. In addition, he performed tests under similar conditions but with no plasma discharges and without modifying any of the initial settings and found that the reactor became quite massive and cooled slowly and that the reactant conversion and product selectivities were slightly decreased. The temperature in the post-plasma zone increased to a maximum and then dropped quickly to a threshold value, below which the conversion stopped. A synergistic effect may be obtained through the combination of non-thermal plasma with a desirable catalyst. This catalysis-plasma process simultaneously has the advantage of high selectivity of the product from the thermal catalysis and fast startup from the plasma technique [96]. Sobaci et al. [53] proved

that the use of a catalyst in a plasma reforming process usually allowed for the lowering of operating temperatures while increasing hydrogen yields, thereby providing higher efficiencies and reducing production costs. The after treatment with catalysts investigated by Bromberg et al. [54] has yielded the best results. Experiments were conducted at atmospheric pressure by using a catalyst on a ceramic, honeycomb frame or a metallic catalyst on different fuels (diesel, methane, ethanol, soybean oil), with the results demonstrating that the efficiency of the plasma-assisted reforming system was much better when coupled with the catalyst (approximately an extra 15% for both efficiency and conversion rate results). Kappes et al. [59] used a combination of DBD with catalyst; good yields and efficiency at high temperature (400 to 600 °C) were observed, with the activation energy provided by the plasma. Furthermore, Bromberg et al. [[64], [97]] used a Ni-based catalyst on an alumina support to decrease the specific power consumption of plasma. The results indicated that hydrogen yield, methane conversion and productivity increased, while the specific energy was reduced. Chao et al. [98] used the combination of plasma with a catalyst in a series for hydrogen production. A Ni-based catalyst was packed in the post plasma zone and hydrogen was produced by the partial oxidation of methane, indicating good energy efficiency with a high hydrogen yield and an elevated methane conversion. Horng et al. [99] investigated the effect of energy saving techniques on producing hydrogen from methane using a plasma-catalyst hybrid converter. They discovered that the energy saving systems reduced the O_2/C ratio and prevented the oxidation of hydrogen and carbon monoxide. Marques et al. [100] reformed methane using a γ-alumina catalyst hybrid reactor with DBD, and methane conversion occurred in the temperature range between 300 to 500 °C, compared to above 425 °C with only a catalyst. Recently, Tao et al. [101] studied the plasma enhanced catalytic reforming of toluene. They found that the introduction of plasma prior to the catalyst bed significantly enhanced the conversion rate of toluene because the plasma activated the HCs to the radical state, resulting in the accelerated decomposition of toluene to form CO and H_2.

Chapter 3

FT synthesis

FT technology can be briefly defined as the means used to convert syngas containing hydrogen and carbon monoxide to HC products. In principle, any carbon source can be used as a raw material for syngas production. In view of decreasing oil reserves and rising oil prices, FT synthesis have gained importance for the production of synthetic fuels and petrochemical base materials from NG, coal and biomass [2]. In the long term, a CO_2-neutral way could be the production of syngas from biomass and its subsequent conversion by FT synthesis.

The synthesis of HCs from the hydrogenation of carbon monoxide over transition metal catalysts was discovered in 1902 by Sabatier and Sanderens. They produced methane from hydrogen and carbon monoxide mixtures over nickel, iron and cobalt catalysts. In 1923, Fischer and Tropsch reported the use of alkalized iron catalysts to produce liquid HCs rich in oxygenated compounds [102]. In FT synthesis, the reaction of H_2 and CO on the surface of the catalyst in situ can be regarded as a surface polymerization reaction. First, monomer units are formed from the reagents. Then, a wide product spectrum of HCs (mainly paraffins) is formed by the successive addition of C_1 units to growing chains on the surface of the catalyst. The main reaction of the FT synthesis is represented by [2]:

$$\mathrm{nCO} + 2\mathrm{nH_2} \rightarrow (\text{-}\mathrm{CH_2}\text{-})_\mathrm{n} + \mathrm{nH_2O} \quad \Delta_R H^o_{298} = -152 kJmol^{-1} \qquad \text{R20}$$

where the term $(-CH_2-)$ represents a methylene group, which is a building block for the longer HCs. The main reaction (R20) is highly exothermic with a reaction enthalpy of -152 kJ per mole converted CO. Undesirable side reactions such as the formation of methane (R19) and alcohols (R21) are represented by:

$$\mathrm{CO} + 3\mathrm{H_2} \rightarrow \mathrm{CH_4} + \mathrm{H_2O} \quad \Delta_R H^o_{298} = -206 kJmol^{-1} \qquad \text{R19}$$

$$\mathrm{nCO} + 2\mathrm{nH_2} \rightarrow \mathrm{C_nH_{2n+2}O} + \text{(n-1)}\mathrm{H_2O} \quad \Delta_R H^o_{298} = -124 kJmol^{-1} \qquad \text{R21}$$

In addition, the co-product, H_2O, can be converted with CO to carbon dioxide and hydrogen by the WGS reaction (R2). The reaction stoichiometry is expressed as:

$$CO + H_2O \rightleftharpoons CO_2 + H_2 \quad \Delta_R H^o_{298} = -41 kJmol^{-1} \qquad \text{R2}$$

Since FT synthesis is considered as an ideal polymerization reaction, it is often assumed that the relative probability of chain growth and chain termination, denoted by α and 1-α, respectively, is independent of chain length. Following this approach, the carbon number distribution of FT product can be represented by a simple Anderson-Schulz-Flory (ASF) distribution model (3.1):

$$W_n = n\,(1-\alpha)^2\,\alpha^{n-1} \tag{3.1}$$

where W_n is the weight fraction of product containing n carbon atoms and α is the chain growth probability.

Fig. 3.1 shows the theoretical product distribution of HCs as a function of α. In general, α is largely determined by the type of catalyst and the specific process conditions. In accordance with the above equation methane will always be the largest single product at α=0; however, by increasing α to one (i.e., α=1), the total amount of methane formed can be minimized compared to the sum of all of the various long-chained products. For all other values of α, a wide range of HCs exists. In reality, significant deviations from the ideal polymerization behavior are observed. Usually the methane selectivity is higher, while the ethane/ethene selectivities are lower than calculated.

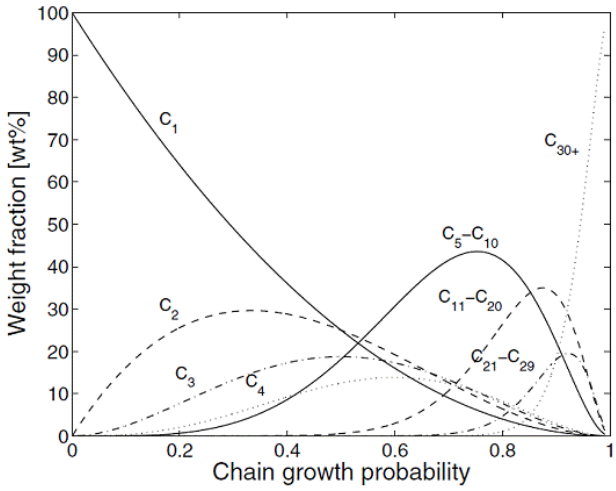

Figure 3.1: Product distribution in FT synthesis as a function of chain growth probability.

Cobalt, iron, nickel and ruthenium are the main catalysts employed for the FT synthesis [[103],[104]]. Ruthenium has a limited availability and high cost, whereas the nickel-based catalyst has high activity but produces too much methane and additionally have poor performance at high pressure due to the production of volatile carbonyls. This leaves only cobalt and iron as practical catalysts with industrial relevance. A disadvantage of iron catalysts is the kinetic inhibition by the co-product water, whereas an advantage is the activity for WGS reaction that allows the use of carbon dioxide containing or hydrogen depleted syngas mixtures [105]. However, the WGS reaction could lead to a loss of carbon monoxide by formation of carbon dioxide. Compared to iron, cobalt catalysts are already active at lower reaction temperatures and have a durability of up to 5 years on stream compared to about 6 months in the case of iron [106]. In addition, cobalt-based catalysts generally produce a high yield in the production of long chain HCs [107]. This behavior has been attributed to the ability of the catalyst to readsorb the formed olefins on the metallic centers, thus increasing the chain length. This increase is accomplished by the decrease in the hydrogenation of the C=C bond and in isomerization reactions [108]. On the other hand, cobalt is more expensive than iron. In addition to the active component, different promoters (Pt, Pd, Ru, Re, K) can be employed [109]. As carrier materials, alumina, silica, and titania − in earlier catalysts also ZnO − can be utilized. Typical chain growth probabilities are 0.5−0.7 for iron and 0.7−0.8 for cobalt [110]. Currently, the development of cobalt catalysts is aimed at maximizing the chain growth probability to values of up to 0.95 [111].

3.1 Types of FT reactor

There are currently two FT operating modes [[13],[104]], either a low-temperature FT (LTFT) or a high-temperature FT (HTFT) process, with temperatures ranging between 200 and 240 °C for LTFT and 300-350 °C for HTFT. One can distinguish between the so-called HTFT process, where gaseous products are formed in moving bed reactors and the LTFT process, in which liquid products are also present under reaction conditions. The HTFT uses iron-based catalysts with the aim to produce gasoline and linear low molecular mass olefins. In addition, significant amounts of oxygenates are also produced. Diesel may be produced by oligomerization of the olefins. The LTFT uses either iron or cobalt-based catalysts to produce high amounts of paraffins and linear products. In addition, the selectivity to high molecular mass linear waxes can be very high. The hydrocracking of the waxes yields excellent diesel fuel. The primary gasoline cuts needs further treatment to obtain a high octane number. Most of the modern FT processes for the production of liquid fuels are LTFT processes, where syngas, liquid products and solid catalysts are present.

Generally, various types of reactors are suitable for performing the highly exothermic FT synthesis. They have already been proven on laboratory, pilot plant and

industrial scale [106].

3.1.1 Fixed bed reactors

The configuration of fixed-bed reactors is quite straight forward and involves tubes or a vessel packed with a definite amount of catalyst (Fig. 3.2). Mostly, tubular fixed-bed reactors are operated in a LTFT mode. Originally, the FT synthesis was carried out in packed bed reactors with catalyst placed inside the tubes and cooling medium (water) on the shell side. A fixed-bed reactor is an appealing technology due to such attractive features as the absence of the requirement to separate the catalyst from the product and the ease of scale-up from a single tube to a pilot plant [9]. However, multitubular reactors exhibit disadvantages. The combination of narrow tubes, high gas velocities and small particles gives rise to high differential pressure over the reactor. To minimize the pressure drop, the catalyst dimension should be chosen between 1 and 3 mm [111]. This leads to a decrease of catalyst utilization and to undesirable effects on product selectivity. In addition, catalyst loading and unloading may be difficult with narrow tubes. Furthermore, in tubes with diameters of several centimeters, as used in the industry, hot spot formation (i.e., axial and radial temperature gradients) will occur which may lead to higher production of methane, lower selectivity to long chain HCs and a shorter catalyst life. To prevent damage of the catalyst, the temperatures of both feed and cooling medium have to be chosen significantly lower than the maximal possible temperature. This gives rise to a decrease in reactor productivity [105].

Ruhrchemie developed the first industrial FT process in third decade of 20^{th} century. A fixed-bed reactor under atmospheric pressure and cooled by evaporating water was used in this process. There was great interest in further development of FT synthesis after World War II. Ruhrchemie and Lurgi developed a five multitubular fixed-bed reactors based on iron catalysts. In 1955, these so-called ARGE reactors were installed for the first time in Sasolburg, South Africa. These are still operated at a pressure of 27 bars and temperature of 230 °C [[2],[106]]. There are 2052 parallel tubes with diameters of 5 cm [[106], [108]]. The length of entire reactor is 12.8 m, 2.95 m diameter and a catalyst inventory of 40 m^3. Each reactor has a production capacity of 21000 t/year. In 1987, an additional reactor was installed which is operated at 45 bars. Comparing with early German multitubular reactor technology, operation of ARGE reactors is with a recycle of unconverted syngas to support the internal heat removal. This gives 25 times higher production capacity along with the combination of higher reaction temperatures and pressures [112]. Shell began the development of the Shell Middle Destillate Synthesis (SMDS) in 1973 that is based on fixed-bed reactor technology and employs cobalt-based catalysts. This technology was developed from Gulf based work, where tubular reactors with a diameter of 2.54 cm and a length of 12.2 m were successfully operated for several months [106]. A FT synthesis plant with a production capacity of 12500 bpd was

placed into operation in Bintulu, Malaysia [111]. That is based on natural gas.

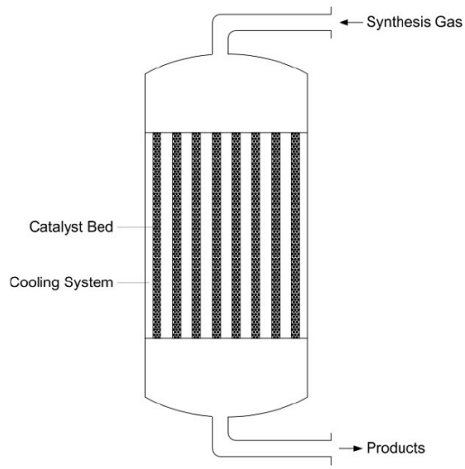

Figure 3.2: Multitubular fixed-bed reactor.

3.1.2 Slurry phase reactors

Slurry reactor system is considered to be suitable for the production of waxes at LTFT operations. The Slurry phase reactor as shown in Fig. 3.3, consists of a shell in which cooling coils are present for steam generation. The syngas is fed to the bottom of the reactor and it rises through the slurry. The slurry consists of liquid HCs (mainly waxes) with catalyst particles suspended in it. The reactant gases diffuse through the liquid phase to the catalyst particles. The heavier products forms part of the slurry and the lighter gaseous products and water diffuse through the liquid. The gaseous products and unreacted reactants pass through the slurry to the freeboard above the slurry bed and then to the gas outlet [113].

In slurry bubble columns, fine catalyst powders with dimensions of 10 to 200 μm are used [2]. Thus, the influence of internal mass transfer resistances are negligible and optimal activity and selectivity can be achieved. Internals assure efficient heat removal from the reactor that allows for a nearly isothermal operation. Even though the achievable catalyst fraction of up to 25 vol.% is lower than in fixed-bed reactors (up to 60 vol.%), the reactor productivity of a slurry bubble column should be higher due to the enhanced catalyst utilization and the higher average reactor temperature. Nevertheless, two aspects decelerated the commercialization of slurry bubble columns for FT synthesis. Both separation of the solid catalyst from the liquid products and the scale-up of these reactors are major challenges for industrial use of slurry bubble columns. Generally, time and cost intensive pilot-plant studies

with reactors of different diameters have to be conducted for a successful scale-up. Only recently, adequate models for FT synthesis in slurry bubble columns have been developed that may facilitate scale-up in the future [[112],[114],[115]].

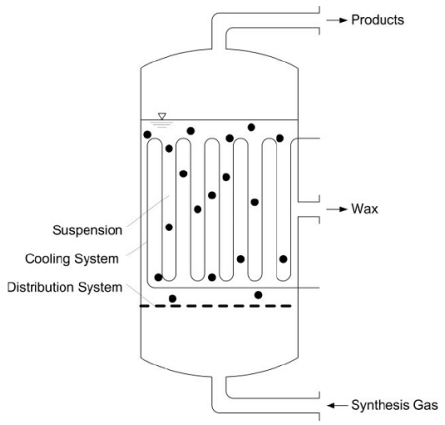

Figure 3.3: Slurry bubble column reactor.

These reactors were tested in different parts of the world (Germany, United Kingdom and U.S.A) in 1950's and 1960's, but were not upscaled to commercial units. Sasol started the development of iron-based slurry bubble column reactors in 1980's [2]. Since the early nineties, a cobalt-based catalysts commercial plant (with 5 m diameter and 22 m length) with a production capacity of 2500 bpd has been operated in South Africa. Exxon Mobil has also developed 200 bpd capacity slurry reactor based on cobalt (with 1.2 m dia). Sasol and Qatar Petroleum commissioned a plant with a capacity of 70000 bpd in June 2006 in Qatar [105]. Further large-scale industrial plants (one in Escravos, Nigeria by SasolChevron and other in Qatar by Shell, Qatar Petroleum) are under construction. These will increase worldwide capacity for FT synthesis fuels to almost 30 Mt/a in 2010 [105].

3.1.3 Two phase fluidized bed reactors

Fixed-bed or slurry bed reactors can not be employed in HTFT processes for the production of lighter HCs (alkenes) and/or gasoline. Two-phase fluidized bed reactors are used for this purpose. On commercial scale, two types of fluidized bed reactors are in operation: (i) the circulating fluidized bed (CFB) and (ii) the turbulent fixed fluidized bed (FFB) [2].

Circulating fluidized bed reactors

These reactors are known as Synthol reactors and operate at a pressure of 20 bars and temperature between 330 and 350 °C. They uses a promoted iron catalyst powder in circulating entrained flow design, as shown in Fig. 3.4 and have two phases of fluidized catalyst: dense and lean. The combined feed gas (fresh and recycled) enters at the bottom of the reactor and entrains catalyst (dense-phase) that is flowing down the standpipe and through the slide valve. The high gas velocity carries the entrained catalyst into the reaction zone (lean-phase), where heat is removed through heat exchangers. Product gases and catalyst are then transported into a large-diameter catalyst hopper where the catalyst settles out and the product gases exit through a cyclone [102]. In order to avoid that the feed gas goes up the standpipe, the differential pressure over the standpipe must always exceed that of the reaction zone. During operation at high temperature, carbon is deposited on the catalyst particles which lower the bulk density of the catalyst and hence the differential pressure over the standpipe. Therefore, it is not possible to raise the catalyst loading in the reaction section for compensating the normal catalyst deactivation with time on stream [2]. The Synthol reactors have been successfully used for many years but there are a number of limitations. They are physically very complex reactors that involve circulation of large amounts of catalyst that lead to considerable erosion in particular regions of the reactor. The first industrial CFB reactor was developed by Sasol in the 1950's. The second generation CFB reactors were installed in Secunda and Mossel Bay and operated at 2.5 MPa with 8000 bpd of production.

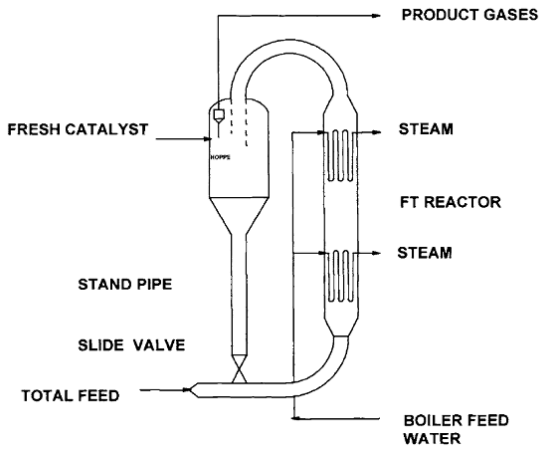

Figure 3.4: Synthol circulating fluidized bed (CFB) reactor.

Turbulent fluidized bed reactors

The FFB reactor known as Sasol Advanced Synthol (SAS) reactor is shown in Fig. 3.5. A vessel containing a fluidized bed consists of reduced, fused iron oxide catalyst. Syngas is bubbled through the bed where it is catalytically converted to HCs that are in the vapor-phase at the process conditions of about 340 °C and 25 bars. The heat produced from the exothermic conversion reaction is removed by passing water through tube coil installed inside the reactor, which also produces heated steam needed for the reaction. The major advantages of the (SAS) reactor over the (CFB) reactor are simplicity, ease of operation and low operating cost due to elimination of the catalyst recycle. Catalyst consumption is reduced to about 40% and maintenance costs to about 15% that of the CFB system. In general, higher conversions are obtained at higher gas loads. The Synthol CFB system disadvantages are eliminated by using SAS reactor that makes use of conventional solid-gas fluidization. For that reason, over the period 1995 to 1999, the sixteen second generation CFB reactors at Secunda plant were replaced by eight SAS reactors. Four of these had diameters of 8 m with capacities of 11000 bpd each and four of 10.7 m diameter each with a capacity of 20000 bpd [2].

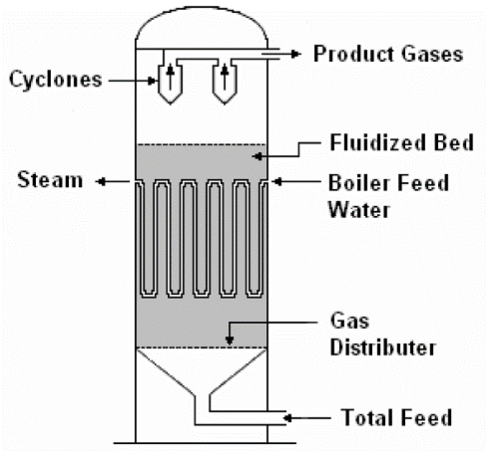

Figure 3.5: Sasol advanced synthol (SAS) reactor.

3.1.4 Microstructured reactors

Microstructured reactors (MSR) are used to overcome the case-specific drawbacks (severe heat and/or mass transfer limitations and selectivities) in conventional reactors. This could result poor control of reaction parameters and failure to meet the market quality demand [116]. Multiphase MSR generally have several advantages

like its large interfacial area allowing fast mixing and reduced transfer resistances, and reduced scales facilitate suppressing of hot spot formation and allow precise temperature control.

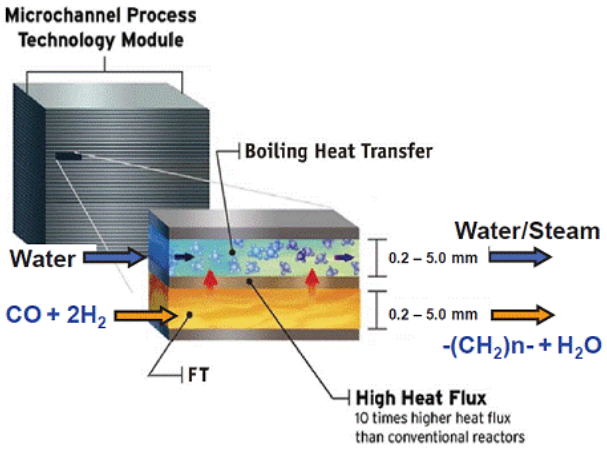

Figure 3.6: Microstructured reactor.

In recent decade, microstructured reactors were developed and proposed for the FT synthesis to fulfill the need of a compact and modular LTFT technology. Two sets of small, parallel channels were used in such reactors (Fig. 3.6): one for FT reaction and other for circulating cooling water to remove the reaction heat released by the FT synthesis. Heat transfer between the channels is highly efficient because of close spacing of channels and conductive wall material. As a result, isothermal operation is enabled even in the case of highly exothermic reactions. However, catalyst inventory may represent an issue due to the specific reactor design (reaction channels surrounded by cooling channels). Accordingly, coating of catalyst is generally done on the FT microchannel's walls. But, in order to increase the catalyst hold-up, configurations involving structured supports and even random packed beds filling each channel have been proposed [[117],[118]]. An acceptable compromise between pressure drops and catalyst inventory has to be sought in the latter case. Oxford Catalyst Group PLC (former Velocys Inc.) and CompactGTL are currently working to develop microchannel technology based on compact FT synthesis reactors. Petrobras (an oil company) seems to be more confident in this alternative. But until now, very few results have been reported on the use of MSR for FT synthesis. There is a major focus on catalyst development in scientific and patent literature [[119],[120]] and on the benefits of enhanced heat and mass transfer characteristics [121]. At the moment, main issues in implementing this technology on commercial scale are: (1) need of many reactors modules (to obtain the required overall capacity), (2) un-proved reliability (related both to the technical complexity and scarce expertise in operating and maintaining such kind of reactors) and (3) cost [122].

This new technology is especially promising for the production of liquid fuels for decentralized and mobile applications. However, this also has been proposed for large-scale plants with capacities up to 50000 bpd. It has been claimed that, using MSR at high conversions and low methane selectivity, capital cost can be reduced significantly [123].

Chapter 4

Materials and methods

This section is divided into two parts, i.e., experimental work and modeling work.

4.1 Experimental work

Two different types of reactors are used: (i) non-thermal plasma-assisted gliding arc catalytic reactor for syngas production and (ii) fixed-bed reactor for FT synthesis.

4.1.1 Non-thermal plasma-assisted gliding arc catalytic partial oxidation reactor

Fig. 4.1 shows the schematic diagram of the non-thermal plasma-assisted GlidArc reforming system designed and built for this research study. It consisted of a non-thermal plasma-assisted GlidArc reactor, gas supply lines, a liquid (water/WCO) supply line and measurement and analysis units.

The non-thermal plasma-assisted GlidArc reactor used in this study had a double-mantle structure. The inner silicon carbide (SiC) ceramic cylinder comprised the reaction chamber containing the granular Ni-based catalyst on the Al_2O_3 support (bulk density = 903 kg/m^3, void fraction = 0.68). The distance between the ceramic inner mantle and the outer steel mantle was 1 mm. The length of the high-voltage diverging electrodes (knives) was 6.1 cm. The vertical part of the GlidArc was partially insulated by a special, thin, multi-layered textile material. The electrical arc that formed between the two knives was powered by a single-phase transformer. The discharges were formed at the closest points to the electrodes, had a very short contact time and were spread by gliding along the edges of the electrodes. The arc

disappeared at the end of the knives, and a new discharge immediately re-formed at the initial locations. The high-voltage (15 kV, 20 mA) self-maintained discharges struck directly across the reactant flow. The electrodes were not cooled, so all of the electrical energy was directly and completely transferred to the processed gas. The temperature was measured with a K-type moveable thermocouple in a thin, hollow pipe in the GlidArc reactor at different places (i.e., from the plasma zone to the exit position of the catalyst bed).

Feed gases, enriched air and normal air were fed through the gas supply line. The feed gases and enriched air were contained in the gas cylinder, whereas the normal air (molar ratio of O_2/N_2=21/79) were supplied from the main line of an air compressor unit, and their flow rates were controlled with calibrated mass flow controllers (MFCs). The feed gas was directly injected from the top of the reaction chamber by MFC1 (Fig. 4.1) without preheating. The normal air/enriched air was first slightly preheated by passing it between the ceramic inner mantle and the outer steel mantle of the GlidArc reactor and was then mixed with feedgas. Its flow was controlled by MFC2.

For WCO reforming, the liquid flow rate (WCO/water) from the feed tank was controlled by the feed pump. The WCO was heated with an electric heater (4 V, 110 mA) before sending it to the GlidArc reactor, but the liquid water was slightly preheated along with normal air and mixed with feed gas before sending it to the GlidArc reactor.

The exhaust gases produced were analyzed off-line using a commercial residual gas analyzer (RGA) combined with a gas chromatograph (GC). Water was removed from the exhaust gas with silica gel (Fig. 4.1). The product gases (mainly H_2, O_2, N_2, CH_4, CO, CO_2, C_2H_4, C_2H_6, C_3H_8 and C_3H_6) from the exhaust pipe were obtained with a special gas syringe and then injected directly into the steel loop of the RGA/GC. Typically the GC was calibrated using typical standards. N_2 was used as an internal standard for the quantitative analysis. Each measurement was performed by the GC two to four times; the difference between each run did not exceed $\pm 2.5\%$.

The catalyst was reduced with a continuous flow of 4.0 NL/min H_2 mixed with 6.0 NL/min N_2 at 600 °C for 4 h at atmospheric pressure. The heat was provided externally by a hot air blower system with a programmable temperature controller. During the start-up period, the temperature in the GlidArc was increased by the complete stoichiometric burning of the propane with normal air. The heat released from the complete combustion of the propane quickly raised the catalyst bed temperature to a suitable temperature in just a few minutes. Thereafter, the flow rates of the feed gas and normal/enriched air were adjusted to the designated experimental values. The syngas produced was immediately flared.

The dry total molar flow of the gas product leaving the GlidArc reactor was defined through an elemental balance of N_2.

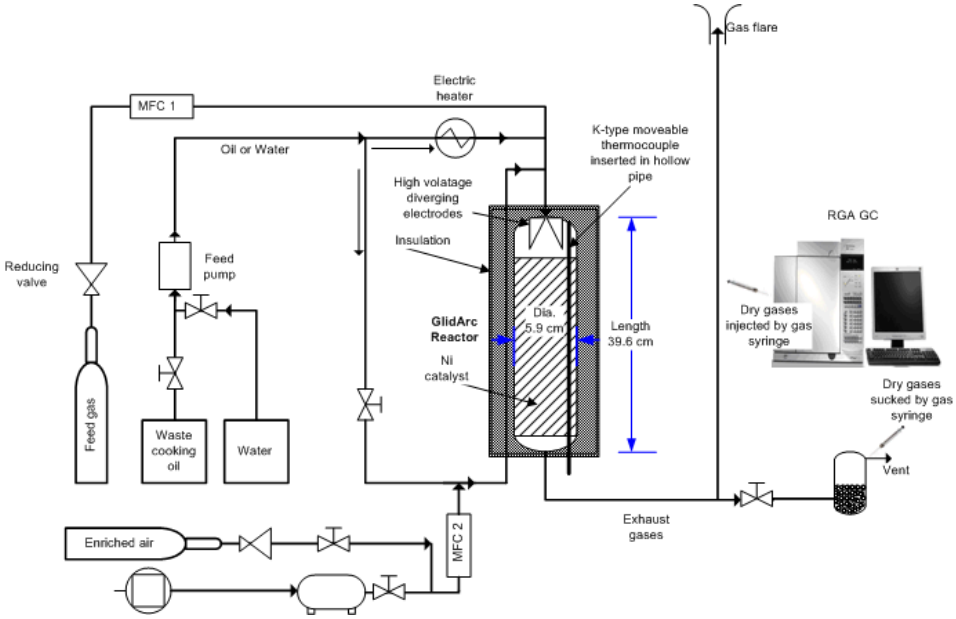

Figure 4.1: Schematic diagram of the non-thermal plasma-assisted GlidArc reforming system. The temperature was measured with a K-type moveable thermocouple in a thin, hollow pipe in the GlidArc reactor at different places.

$$F_{dry,out} = \frac{N_2, in}{y_{N_2,in}}. \tag{4.1}$$

The reactants conversion was defined as:

$$X_{i,in} = \frac{F_{i,in} - F_{i,out}}{F_{i,in}} \times 100. \tag{4.2}$$

where $F_{i,in}$ is the inlet molar flow (mol/min) of component i of the reactants and $F_{i,out}$ is the outlet molar flow (mol/min) of component i of the product gas. The yield of product i to form species j ($Y_{i,j}$) was defined with Equation (4.3) as:

$$Y_{i,j} = \frac{v_{i,j}.F_{i,out}}{\sum v_{i,k}.F_{k,in}} \times 100. \tag{4.3}$$

where $v_{i,j}$ is the stoichiometric amount of component i in species j. The denominator is the sum over all species k. The GlidArc reactor thermal efficiency (η) was defined as:

$$\eta = \frac{F_{syngas}.LHV_{syngas}}{(\sum (F_{i,in}.LHV_{i,in}) + \sum (E_{i,in}))} \times 100. \tag{4.4}$$

where F_{syngas} is the outlet molar flow of syngas (mol/min), LHV_{syngas} and $LHV_{i,in}$ are the lower heating values of the syngas and component i of the reactants, respectively (kJ/mol). $E_{i,in}$ is the sum of electric energy provided to the high-voltage diverging electrodes of the GlidArc and the heating of the electric heater (kJ/min).

4.1.2 Fixed bed FT reactor

A schematic diagram of the experimental setup is shown in Fig. 4.2. The setup consisted of a double-mantled single-tube fixed-bed FT reactor, a pressurizer, a steam supply line, a gas supply line and offline measurement systems for gaseous, liquid and wax products.

The length of the vertical FT reactor was 2 m, with an inner diameter of 27.2 mm and a wall thickness of 3.05 mm. The inner diameter of the mantle, i.e., the coolant jacket, which surrounds the FT reactor tube, was 82.8 mm. The coolant jacket was insulated with 15 cm of special textile material to minimize the heat loss to the surroundings. In general, the FT reaction is highly exothermic, and the average heat released per $(-CH_2-)$ formed is higher than the typical catalytic reactions used in the oil refining industry. This heat was removed from the system using pressurized boiling water, and its working principle is as follows. Initially, the coolant jacket and two-thirds of the pressurizer were filled with water. One-third of the pressurizer remained empty to be filled with steam. The steam (produced in a steam generator at a pressure of 16 bars and 200 °C) was injected directly into the water in the coolant jacket. The function of the pressurizer was to assure that the setup contained water all the time, i.e., the steam present above the water surface in the pressurizer placed the saturated water in the coolant jacket under high pressure. Steam flowed out in the form of water from the setup through the steam pot of the pressurizer. The steam pot regulated the flow of the steam by allowing only the condensed water to drain. The temperature of the outer surface of the reactor vessel was measured at seven different points (T_2 to T_8) with K type thermocouples.

Biosyngas/normal syngas, H_2 and N_2 were fed through the gas supply line. The flow rate of the gas was regulated by using a calibrated Bokhorst mass flow controller. The backflow of the gas was minimized by using backslash valves.

Prior to the reaction, cobalt catalysts were activated in situ for 24 h using pure H_2 at 1 to 4 bars and 400 °C. Liquid water was collected during this time. The linear gas velocity was kept relatively high to remove the water produced during the process. Water was regarded as an important factor because it sintered the cobalt catalyst in the FT reactor. After 24 h of reaction time, the catalyst bed was cooled to 170 °C, the system was pressurized to 20 bars, and the syngas/biosyngas

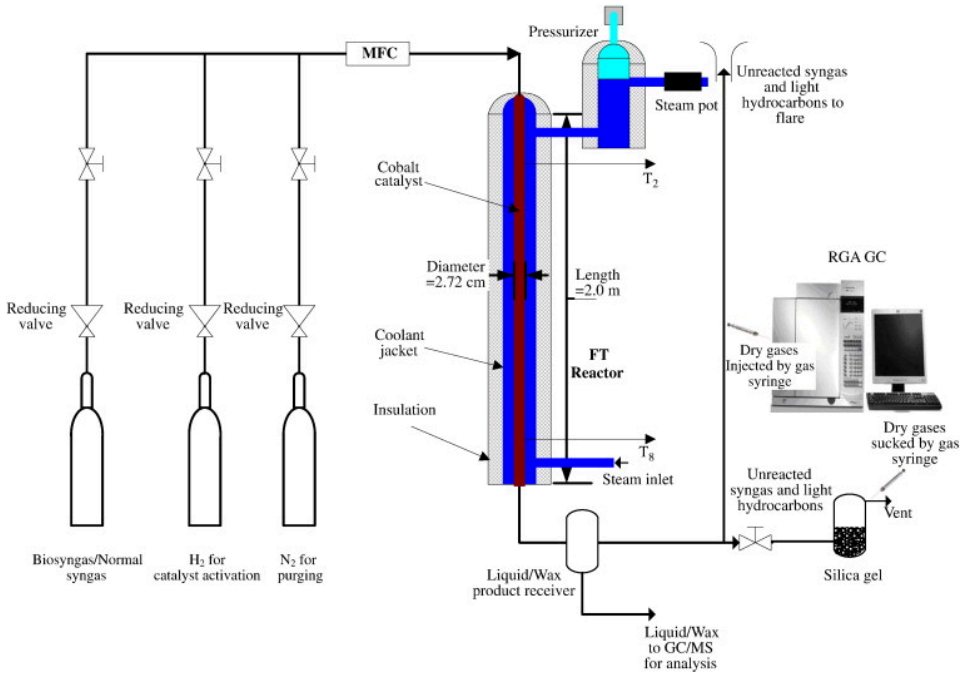

Figure 4.2: Schematic diagram of the FT system experimental setup.

was introduced into the reactor from the top. The temperature was then slowly increased to the desired start-up reaction temperature. Conversion, selectivities, productivities and α were measured over a minimum 10 h period before changing the parameters. In addition, the system was also purged with N_2 to minimize any previous effects before changing the parameters. Table 4.1 lists the specifications of the commercial spherical heterogeneous unpromoted cobalt catalyst used in this study.

Table 4.1: Specifications of the catalyst used in this study.

Property	Unit	Real content
Al_2O_3	weight %	87
Co	weight %	9.4
Surface area	m^2/g	260
Pore volume Hg	cm^3/g	0.34
Bulk density	kg/m^3	700
Water pickup	weight %	56
Diameter	mm	3
Voidage		0.44

The product stream form the FT reactor was split into three phases: gas, liquid and wax. After each interval of each experimental run, the liquid/wax products

collected in the traps were then separated into water and oil/wax phases. Hence, the FT products consisted of gaseous, aqueous, oil and wax phases. The formation of oxygenates over this catalyst was assumed negligible. The tail gases, mainly N_2, unreacted syngas and light HCs (C_1 to C_4), were analyzed offline from time to time, using a commercial residual gas analyzer (RGA) combined with a gas chromatograph (GC). Water was removed from the tail gases with silica gel, and the product gases were obtained with a special gas syringe and then injected directly into the steel loop of the RGA/GC. N_2 contained in the syngas was used as an internal standard to determine the CO and H_2 conversion. Liquid oil/wax product weights were calculated by overall mass balance. The CO and H_2 conversions were defined as:

$$X_{CO} = \frac{CO_{moles,in} - CO_{moles,out}}{CO_{moles,in}} \times 100, \tag{4.5}$$

$$X_{H_2} = \frac{H_{2moles,in} - H_{2moles,out}}{H_{2moles,in}} \times 100. \tag{4.6}$$

After performing the quantitative analyses of C_1 to C_4 HCs, the selectivity of $C_5{}^+$ ($S_{C_5^+}$) HCs is calculated as follows:

$$S_{C_5^+} = 100 - (S_{C_1} + S_{C_2} + S_{C_3} + S_{C_4} + S_{CO_2}) \tag{4.7}$$

For oil phase analysis, the samples were diluted 1:1000 with dichloromethane (DCM, "Purex analytical grade" SDS, Peypin, France) and analyzed on a Shimadzu GC-2010 gas chromatograph equipped with an AOC-20i/s auto-sampler by injecting 1.0 μL of sample into a split/splitless injector (split mode, split ratio of 1:20) at 280 °C. A fused silica capillary column (30-m length and 0.32-mm inner diameter) coated with a 0.25-μm nonpolar DB-5 liquid phase (Agilent JW, Agilent Technologies) was used with a temperature program that started at 50 °C and increased 5 °C/min until 275 °C was reached. The temperature was then held for 5 min. The carrier gas was H_2 at a constant inlet pressure of 0.7 bars. The flame ionization detector (FID) was operated at 275 °C using hydrogen (40 mL/min), air (400 mL/min), and nitrogen makeup gas (30 mL/min). Instrument control, data storage, and handling were performed with the Shimadzu GC solutions chromatographic data system (version 2.3). *n*-Alkane standard solutions for identification were prepared by diluting (approximately) 0.1% stock solutions in cyclohexane with DCM (1:10). All alkenes from *n*-C_{11} to *n*-C_{28} were available (most of them at purities >98%). For wax phase analysis, the collected samples were examined using Agilent gas chromatography/mass spectrometry (GC/MS). Calibration and reference mixtures were used as calibration standards. These samples were first dissolved in DCM (0.5 to 1.0 mass %) and then analyzed. A 60 m × 0.3 mm PLOT Q column was used in a HP GCD G1800A instrument with helium (He) as a carrier gas. For all three phase measurements, each measurement was taken by performing GC two

to four times; the difference between each run did not exceed ±2.5%. The offline analysis of oil and wax provided the distribution of the products, which were then used to calculate the selectivities of individual species on a carbon atom basis. The selectivity of all carbon species was calculated as:

"C_n" Selectivity of product(%) =No. of moles of product formed×No. of C atom present/No. of moles of CO consumed.(4.8)

4.2 Reactor modeling

4.2.1 2D Pseudo homogeneous reactor model

To obtain a good understanding of the behavior of the laboratory FT reactor, modeling and simulation studies were performed to enable the predictions concerning its behavior. These studies are of great interest for the optimization of the process and the scale-up of the reaction in the future. In general, the 1D model is not capable of predicting the temperature runaway within the FT reactor. Results by Marvast et al. [124] reveal that an error of 12 K in the radial direction was observed, indicating one of its drawbacks; hence, if all heat transfer data are available, the more accurate 2D model should be used. In this study, a 2D, gas solid, pseudo-homogeneous, steady-state plug flow model was used to investigate the effects of operating conditions on the behavior of a fixed-bed reactor for FT synthesis. The governing equations for a 2D pseudo-homogeneous model were formulated using cylindrical coordinates. Under typical low temperature FT conditions (20 bar, 493 K), more than 99 mol% of the reacting species were in the gaseous phase (thermodynamic equilibrium calculations), even though the process was aimed at producing a wax-phase product. Thus, a gas-solid system was assumed to estimate the main trends [125]. Based on the kinetic rate expressions given in the literature, it was assumed that external mass transfer limitations were neglected [126]. This assumption is important for the model presented below, which was of the pseudo-homogeneous type, according to Froment and Bischoff [127]. In this steady-state model, a radial dispersive plug flow was described by mass and energy balance equations: both presenting a convective term, a radial dispersive term and a reactive term. The plug flow regime was assumed with no channeling along the bed. The axial dispersion and axial effective thermal conductivity was ignored with constant porosity of the packing along the bed. The classical Ergun law was applied to calculate the overall pressure drop by assuming uniform packing. Several parameterizations for the friction factor (f) are given in the literature for this Ergun equation. It is valid for spheres over a relatively broad range of particle Reynolds numbers was used in this work [127]. In addition, the total density of the fluid changed with the length and

was calculated by applying the chain rule to the ideal gas law. Finally, gas velocity was computed from the continuity equation. Table 4.2 summarize the governing equations and list the boundary conditions applied to the fixed-bed FT reactor.

Table 4.2: 2D pseudo-homogeneous model equations and boundary conditions.

Gas phase	
Mass balance	$\rho_g \cdot u_z \cdot \frac{\partial w_j}{\partial z} = -\rho_g \cdot w_j \frac{\partial u_z}{\partial z} - w_j \cdot u_z \frac{\partial \rho_g}{\partial z}$ $+D_{er} \cdot \left(\frac{\partial \rho_g}{\partial r} \cdot \frac{\partial w_j}{\partial r} + \frac{\rho_g}{r} \cdot \frac{\partial w_j}{\partial r} + \rho_g \cdot \frac{\partial^2 w_j}{\partial r^2}\right) + r_j \cdot M_j \cdot \rho_b^{cat}$
Energy balance	$\rho_g \cdot u_z \cdot C_p^g \cdot \frac{\partial T}{\partial z} = \lambda_{er} \cdot \left(\frac{1}{r} \cdot \frac{\partial T}{\partial r} + \frac{\partial^2 T}{\partial r^2}\right) + \rho_b^{cat} \cdot \sum_i r_i \left(-\Delta H_i\right)$
Momentum balance	$\frac{\partial u_z}{\partial z} = -\frac{u_z}{\rho_g} \cdot \frac{\partial \rho_g}{\partial z}$
	$\frac{\partial \rho_g}{\partial z} = \frac{M}{R} \cdot \left(\frac{1}{T} \cdot \frac{\partial P}{\partial z} - \frac{P}{T^2} \cdot \frac{\partial T}{\partial z}\right)$
	$-\frac{\partial P}{\partial z} = f \cdot \frac{\rho_g \cdot u_z^2}{d_p}$
	$f = \frac{(1-\varepsilon)}{\varepsilon^3} \cdot \left(a + b \cdot \frac{1-\varepsilon}{Re}\right)$
	$a = 1.75$
	$b = 4.2Re$
Boundary conditions	
	$\left.\frac{\partial w_j}{\partial r}\right\|_{r=0} = 0$ for all z
	$\left.\frac{\partial w_j}{\partial r}\right\|_{r=R} = 0$ for all z
	$\left.\frac{\partial T}{\partial r}\right\|_{r=0} = 0$ for all z
	$\left.\frac{\partial T}{\partial r}\right\|_{r=R} = -\frac{U}{\lambda_{er}} \cdot \left(T\right\|_{r=R} - T_w)$ for all z
	$u_z = u_{z,in}$ for z=0

4.2.2 2D Heterogeneous reactor model

The interplay between chemical and physical processes has been acknowledged to be a fundamental issue in the modeling [[128],[129]] of fast, exothermic reactions. Plug flow reactor models are unsatisfactory for catalytic combustion applications due to the excessive simplifications in heat and mass transport; full computational fluid dynamics models or at least lumped models accounting for transport phenomena are required [[26],[130],[131]]. Thus, for the simulation of the CPO of methane to syngas on a Ni-based catalyst, a 2D, heterogeneous, steady-state model with no gradients inside the catalyst particle was formulated using cylindrical coordinates to investigate and validate the effects of the operating conditions [127]. Rafiq and

Hustad [132] reported that the catalyst particle was assumed to be isothermal, and the main transport resistances outside the catalyst pellet were due to mass and heat transfer. Intra-particle concentration and temperature gradients were not considered because the catalyst used was nonporous [133]. In addition, with the simulation hypotheses that the GlidArc reactor was assumed to be in thermodynamic equilibrium, the reformed gas composition was calculated by means of an intrinsic kinetics approach due to lack of sufficient kinetics data for the plasma zone. Minutillo et al. [134] and Benilov et al. [135] have shown that the use of standard kinetic schemes, without the inclusion of specific plasma processes, was sufficient for the simulation of syngas production in discharges with hot plasmas, specifically in low-current arc discharges.

Table 4.3: 2D heterogeneous model equations and boundary conditions.

Gas phase	
Mass balance	$\rho_g \cdot u_z \cdot \frac{\partial w_j}{\partial z} = -\rho_g \cdot w_j \frac{\partial u_z}{\partial z} - w_j \cdot u_z \frac{\partial \rho_g}{\partial z}$ $+D_{er} \cdot \left(\frac{\partial \rho_g}{\partial r} \cdot \frac{\partial w_j}{\partial r} + \frac{\rho_g}{r} \cdot \frac{\partial w_j}{\partial r} + \rho_g \cdot \frac{\partial^2 w_j}{\partial r^2}\right) - k_{g,j} \cdot a_v \left(w_j - w_{j,s}\right)$
Energy balance	$\rho_g \cdot u_z \cdot C_p^g \cdot \frac{\partial T}{\partial z} = \lambda_{er} \cdot \left(\frac{1}{r} \cdot \frac{\partial T}{\partial r} + \frac{\partial^2 T}{\partial r^2}\right) - h_{cat} \cdot a_v \left(T - T^s\right)$
Momentum balance	$\frac{\partial u_z}{\partial z} = -\frac{u_z}{\rho_g} \cdot \frac{\partial \rho_g}{\partial z}$
	$\frac{\partial \rho_g}{\partial z} = \frac{M}{R} \cdot \left(\frac{1}{T} \cdot \frac{\partial P}{\partial z} - \frac{P}{T^2} \cdot \frac{\partial T}{\partial z}\right)$
	$-\frac{\partial P}{\partial z} = f \cdot \frac{\rho_g \cdot u_z^2}{d_p}$
	$f = \frac{(1-\varepsilon)}{\varepsilon^3} \cdot \left(a + b \cdot \frac{1-\varepsilon}{Re}\right)$
	$a = 1.75$ $b = 4.2Re$
Solid phase	
Mass balance	$0 = k_{g,j} \cdot a_v \left(w_j - w_{j,s}\right) + r_j \cdot M_j \cdot \rho_b^{cat}$
Energy balance	$0 = h_{cat} \cdot a_v \left(T - T^s\right) + \rho_b^{cat} \cdot \sum_i r_i \left(-\Delta H_i\right)$
Boundary conditions	
	$\left.\frac{\partial w_j}{\partial r}\right\|_{r=0} = 0$ for all z
	$\left.\frac{\partial w_j}{\partial r}\right\|_{r=R} = 0$ for all z
	$\left.\frac{\partial T}{\partial r}\right\|_{r=0} = 0$ for all z
	$\left.\frac{\partial T}{\partial r}\right\|_{r=R} = 0$ for all z
	$u_z = u_{z,in}$ for z=0

The governing equations of a 2D heterogeneous adiabatic model are given in Table 4.3 with the corresponding list of boundary conditions. The gas phase mass and en-

ergy balances are coupled with equations of continuity between the catalyst particles and bulk phase. In other words, the mass and enthalpy for the gas phase and for the solid phase included axial convection, solid conduction, radial dispersion and gas-solid transport terms. In the gas phase, the transport mechanism in the axial direction is considered to be of the plug flow type with no channeling along the bed. The axial dispersion of heat and mass and the axial effective thermal conductivity was ignored with the constant porosity of the packing along the bed. The effect of plasma was included in the form of inlet temperature in a gas phase energy balance. The inlet temperature (T_{in}) was computed from the correlation $Q = m.c_p.(T_{in} - 298)$, where Q is the input plasma energy ($Q = Voltage(V) \times Current(I)$), m is the inlet mass flow and c_p is the inlet heat capacity of the gas mixture. The classical Ergun law was applied to calculate the overall pressure drop by assuming uniform packing. A pressure drop relation valid for spheres over a relatively broad range of particle Reynolds numbers was used in this work [127]. In addition, the total density of the fluid changed with the length and was calculated by applying the chain rule to the ideal gas law. Finally, the gas velocity was computed from the continuity equation.

Table 4.4 displays the important correlations of the physical properties for both individual and a mixture of species, such as viscosity, heat capacity, heat conductivity and average molecular mass. Other parameters, such as the overall heat transfer coefficient, effective radial conductivities, mass-transfer film coefficients between the solid and gas phases and the effective diffusivities, are also listed. The value of heat transfer coefficient (h_p) of the catalyst material used was 30,000 $\mathrm{W.m^{-2}.K^{-1}}$.

The governing equations of the above mentioned models formed a set of stationary differential algebraic equations coupled with the non-linear algebraic equations of the kinetic model. The finite difference approximation was applied to solve the set of equations. MATLAB programming language was used as application software for numerical simulation. Discretization routines dss020 and dss042 were applied to find the first and second derivatives in the radial direction, respectively. MATLAB function “fsolve” was used to solve the set of equations for the catalyst phase (i.e., heterogeneous model). Ode15s was applied to integrate the independent variable, the reactor length (z).

Table 4.4: Correlations of physical properties.

Parameters	Equations	Reference
Species heat capacity	$C_{pj} = A_j + B_j T + C_j T^2 + D_j T^3$	[136]
Mixture heat capacity	$C_p = \sum_j (y_j \cdot C_{pj})$	
Species conductivity	$\lambda_j = A_i + B_j T + C_j T^2 + D_j T^3$	[136]
Mixture gas conductivity	$\lambda g = \sum_j (y_j \cdot \lambda_j)$	
Species viscosity	$\mu_j = \frac{b_j \cdot T^{1.5}}{T + S_j}$	[137]
Mixture viscosity	$\mu_g = \sum_j (y_j \cdot \mu_j)$	
Average molecular mass	$M = \sum_j (y_j \cdot M_j)$	
Conversion from mass fraction to mole fraction	$y_j = \frac{\frac{w_j}{M_j}}{\sum_j \left(\frac{w_j}{M_j}\right)}$	
Reaction enthalpy	$\Delta H_{i,T} = \Delta H_{298K} + \frac{T-298}{1548-298} \cdot (\Delta H_{1548K} - \Delta H_{298K})$	[138]
Particle surface area	$a_v = \frac{3}{r_p} \cdot (1 - \varepsilon)$	
Heat coefficient	$\frac{1}{U} = \frac{1}{\alpha_w} + \frac{d_i}{2 \cdot \lambda_{st}} \ln \frac{d_o}{d_i}$	[139]
	$\alpha_w = \alpha_w^o + 0.444 \cdot Re \cdot Pr \cdot \frac{\lambda_g}{d_p}$	
	$\alpha_w^o = \frac{8.694}{d_i^{4/3}} \cdot \lambda_{er}^o$	
Mass coefficient	$k_j = u_z \cdot 1.17 \cdot \left(\frac{d_p \cdot u_z \cdot \rho_g}{\mu_g}\right)^{-0.42} \cdot \left(\frac{\mu_g}{\rho_g \cdot D_j}\right)^{-0.67}$	[136] &
	$D_j = \frac{10^{-4} \cdot \left(0.00143 \cdot T^{1.75}\right)}{P \cdot M_{j,b}^{0.5} \left(\left(\sum v_j\right)^{1/3} + \left(\sum v_b\right)^{1/3}\right)^2}$	[140]
	$M_{j,b} = 2 \cdot \left(\frac{1}{M_j} + \frac{1}{M_b}\right)^{-1}$	
Radial diffusivity	$D_{er} = \frac{1}{1.1 \cdot P_{er}^d} \left(\frac{1}{u_z \cdot d_p} - \frac{\rho_g \cdot \left(1 - \sqrt{1-\varepsilon}\right)}{Re \cdot \mu_g}\right)$	[141]
	$P_{er}^d = 8 \cdot \left[2 - \left(1 - \frac{2 \cdot d_p}{d_i}\right)^2\right]$	
	$Re = \frac{\rho_g \cdot u_z \cdot d_p}{\mu_g}$	
Radial gas conductivity	$\lambda_{er} = \lambda_{er}^o + 0.14 \cdot \lambda_g \cdot Re \cdot Pr$	[138]
	$\lambda_{er}^o = \lambda_g \cdot \left[\varepsilon \left(1 + \beta \cdot \frac{d_p \alpha_{rv}}{\lambda_g}\right) + \frac{\beta \cdot (1-\varepsilon)}{\frac{1}{\frac{1}{\phi} + \frac{\alpha_{rs} \cdot d_p}{\lambda_g}} + \gamma \cdot \frac{\lambda_g}{\lambda_s}}\right]$	
	$\alpha_{rv} = \frac{0.227 \cdot 10^{-3}}{1 + \frac{\varepsilon}{2(1-\varepsilon)} \cdot \frac{1-P}{P}} \left(\frac{T}{100}\right)^3$	
	$\alpha_{rs} = 0.2227 \cdot 10^{-3} \frac{P}{2-P} \left(\frac{T}{100}\right)^3$	
	$\gamma = \frac{2}{3}$	
	$\phi = 0.3$	
	$\lambda_s = 0.243 \frac{W}{m.K}$	

Chapter 5

Results and discussion

This chapter briefly summarizes the key results from this work. Complete results and more detailed discussions are given in Papers A to E.

5.1 Paper A: Synthesis gas from methane by using a plasma-assisted gliding arc catalytic partial oxidation reactor

In this work, the potential for the CPO of methane to produce syngas was studied both experimentally and thermodynamically at a fixed pressure (1 bar) and electric power (0.3 kW). The investigations were performed in a partially adiabatic plasma-assisted (non-thermal) GlidArc reactor, using a Ni-based catalyst. Two cases were studied: in the first, normal air (molar ratio of O_2/N_2=21/79) was used, whereas enriched air (O_2/N_2=40/60) was utilized in the second. The individual effect of the O_2/CH_4 molar ratio, GHSV and T_{exit} was studied for both cases. The main trends of the CH_4 conversion, the syngas yield and the thermal efficiency of the reactor based on the LHV were analyzed and compared.

Effect of O_2/CH_4 molar ratio

In general terms, the reforming was more sensitive to the O_2/CH_4 molar ratio than the GHSV and temperature terms [142]. As a result, it was decided to first focus on the influence of the O_2/CH_4 molar ratio and to more precisely perform the other two analyses afterwards. A series of reforming tests was performed under a fixed total GHSV of 1.8 NL/(g_{cat}.h) and a fixed discharge power by varying the O_2/CH_4 molar ratio from 0.3 to 1.5.

The equilibrium and experimental yields for hydrogen and carbon monoxide as a function of the O_2/CH_4 molar ratio are depicted in Figs. 5.1a and b, respectively. It can be seen that the syngas yields were significantly affected by the O_2/CH_4 molar ratio and passed through a maximum at approximately O_2/CH_4=0.8, after which the syngas yield decreased with increases in the ratio. This could be explained by the contribution of the combustion reaction because the higher the ratio, the more excessive the O_2 molecules, thus leading to the oxidation reactions.

Fig. 5.1c illustrates the reactor thermal efficiency based on LHV which corresponds to the O_2/CH_4 molar ratio. The solid dashed lines in the figure show the equilibrium thermal efficiency for two cases of: (a) normal air and (b) enriched air. As CH_4 oxidation dominates, the thermal efficiency generally remains between 30% and 70%. The highest equilibrium thermal efficiencies, equaling 70% and 66%, respectively, were obtained for O_2/CH_4 molar ratios of approximately 0.8 for both cases. This is because, at this value, a maximum amount of syngas (i.e. the highest yield at this value) is produced, and the thermal efficiency is strongly dependent on the amount of syngas produced. The experimental data did not completely approach the equilibrium values, indicating a lesser thermal efficiency of the reactor employed in this study.

The deviation of the experimental product composition from thermodynamic equilibrium points to a kinetic limitation within the system, particularly the well-known two-stage process for partial oxidation [[143],[144]], which may not have had sufficient time or energy to complete. The two-stage partial oxidation process begins with an initial rapid oxidation phase, in which all free oxygen is consumed to mainly produce H_2O and CO (and some CO_2) [[145],[146]]. This is then followed by a second but much slower endothermic reforming stage, in which mostly H_2O and some CO_2 react with residual CH_4 to further produce syngas. It is also possible that the secondary reforming stage did not reach completion because of heat losses in the post-plasma treatment zone or a too-limited amount of residence time [147]. In addition, for every case, the conversion, yield and efficiency for enriched air was less due to the fact that the T_{exit} difference for normal and enriched air was very small. The natural rise in temperature for enriched air was high, although the reactor was not fully adiabatic, so due to heat losses along the length of the reactor the temperature difference between them remained very low at the bed exiting temperature.

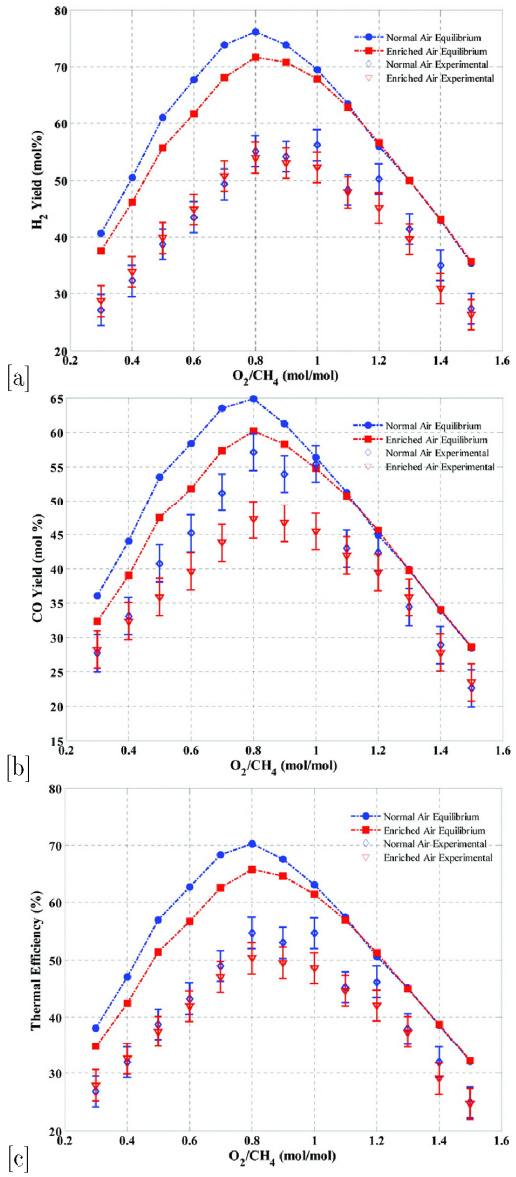

Figure 5.1: (a) Equilibrium and experimental H_2 yield, (b) equilibrium and experimental CO yield, (c) equilibrium and experimental thermal efficiency as a function of O_2/CH_4 molar ratio at GHSV=1.8 NL/(g_{cat}.h).

Effect of GHSV

It is interesting to note from Figs. 5.1a-c that the maximum H_2 and CO yields do not always occur at the O_2/CH_4 ratio of 0.5 as one would have thought. The O_2/CH_4 ratio for the maximum H_2 and CO yields move from 0.5 to a higher value as temperature decreases. At temperatures greater than 800 °C, this optimal O_2/CH_4 ratio remains at 0.5 [147]. Therefore, the O_2/CH_4 molar ratio, ranging from 0.6 to 0.8, is suggested to be appropriate for the partial oxidation reforming process as well as for this study, and no carbon soot was observed on the catalyst surface after each set of experiments. The optimum O_2/CH_4 molar ratio suggested in this study is close to 0.7 as recommended by Benilov et al. [135], who applied standard kinetic schemes to simulate the CH_4 reforming with low-current arcs [98].

Figs. 5.2a and b show the H_2 and CO yields, respectively. The equilibrium H_2 yields for normal air and enriched air increased from 34% to 86% and from 29% to 85%, respectively. The respective increases in H_2 yields for the experimental results are from 28% to 72% and from 26% to 69%, whereas the equilibrium CO yields for normal air and enriched air increased from 14% to 83% and from 11% to 82%, respectively. The respective increases in CO yields for the experimental results are from 11% to 65% and from 9% to 63%. Increases in the syngas yield with increases in GHSV may be due to increases in the temperature of the reforming system, which allows H and C atoms to further oxidize. The thermal efficiency of the GlidArc reactor is evaluated in Fig. 5.2c as a function of the GHSV. It compares the thermal efficiency from experimental and equilibrium calculations which correspond to the operating conditions described above. The experimental results are somewhat low, although there is an increasing trend similar to that of the equilibrium results with an increasing GHSV. In both cases, the thermal efficiency of the reactor is indicated by solid dashed lines. The thermal efficiency based on the equilibrium calculations shows that for normal and enriched air, there was an increase from 25% to 83% and from 21% to 82%, respectively, whereas for the experimental results the increase went from 20% to 68% and from 19% to 64%, respectively.

The results shown in Figs. 5.2a-c indicate that by increasing GHSV, a net increase of the energy release in the solid phase takes place because of the rise of both methane conversion, and the gas mass flow rate fed to the reactor [151]. Considering the partial oxidation operation, the increase in the temperature gradient at higher GHSVs suggests a well-known two-stage process with heat and mass transport limitations. The presence of internal or external diffusional limitations may be addressed by the Weisz and Prater [148] and Mears [149] criteria, respectively. In order to obtain a rough estimate of possible external diffusional limitations, the Mears criterion given by Eq.(5.1) was calculated assuming 50% O_2 conversion within 10 mm of the bed [150]:

$$N_{Mears} = \frac{-r_A \rho_b R n}{k_c C_{bA}} < 0.15. \tag{5.1}$$

where r_A is the rate of reaction (mol/(g.s)), ρ_B is the bulk density of the catalyst bed (g/cm^3), R is the particle size (m), n is the reaction order, C_{bA} is the bulk concentration of A (mol/cm^3) and k_c is the film mass transfer coefficient (m/s). Film mass transfer coefficient (k_c) was calculated to be 6.1×10^{-3} m/s (estimated from the correlation $Sh = (k_c d_t)/(D_M)$ where d_t is the reactor diameter (m), D_M is the diffusivity in the bulk gas (m^3/s) and Sh is the Sherwood number). The Sh number is given by the following correlations $\varepsilon.Sh = 0.357 Re_p^{0.641} Sc^{0.33}$, $Re_p = (G d_p)/\mu$ and $Sc = (\mu)/(\rho D_M)$. Using this and assuming the reaction order of oxygen to be in the range 0.5 to 2, according to reaction stoichiometrics for partial oxidation and total combustion, it was found that N_{Mears} was in the range 1.38 to 5.5 for a gas temperature of 1293 K at highest linear gas velocity (0.23 m/s). This indicates strong mass transfer limitations on oxygen in all our studies. The same conclusion was reached for methane assuming 30% conversion of methane within 10 mm of the bed.

Additionally, Froment and Bischoff [127] proposed a more rigorous criterion for determining the maximum possible temperature difference between the surface and gas phase $T_s - T$ using Eq.(5.2):

$$\Delta (T)_{max} = 0.7 \left[\frac{-\Delta H}{M_m C_p}\right] \left[\frac{ln\,(1 + \delta_A p_A/p_t)}{\delta_A}\right]. \tag{5.2}$$

where ΔH is the reaction enthalpy, M_m and C_p are the molar mass and heat capacity of the fluid, respectively, p_A is the partial pressure of A in the feed and p_t is the total inlet pressure. Assuming only partial oxidation is taking place, which is mildly exothermic with ΔH $=-25.9$ to -22.6 kJ/mol in the temperature range 673 to 1293 K, $(\Delta T)_{max}$ was found to be 100 to 115 K. However, considering the exothermicity of total combustion with $\Delta H \approx -803$ kJ/mol and taking into account the selectivity, ΔH was calculated to be about -120 kJ/mol for the overall reactions. This corresponds to a $(\Delta T)_{max}$ in the range 500 to 550 K. Comparing our estimate to some calculated literature values, the maximum surface temperature and outlet gas temperature in the range 300 to 400 K is calculated from the results reported by Chao et al. [98]. For higher GHSV Basini et al. [22] and Bizzi et al. [151] reported a temperature difference between maximum surface temperature and outlet gas temperature in the range 350 to 450 K for rhodium coated alumina.

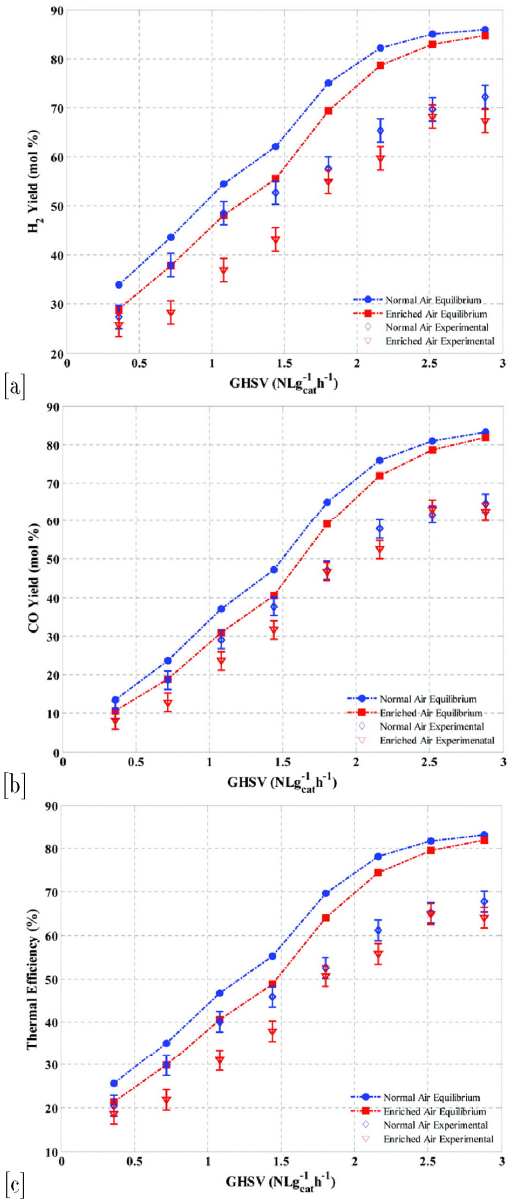

Figure 5.2: (a) Equilibrium and experimental H_2 yield, (b) equilibrium and experimental CO yield, (c) equilibrium and experimental thermal efficiency as a function of GHSV at O_2/CH_4 molar ratio=0.7.

Effect of temperature

Considering the above results, GHSVs for normal and enriched air in the range of 1.8 to 2.9 NL/(g_{cat}.h) seem to be a promising choice for achieving the goal of an H_2/CO ratio of 2. In the last part of the study, a series of experiments was performed to investigate the effect of T_{exit}. In this set of experiments, the values of the O_2/CH_4 molar ratio and GHSV were kept constant at 0.7 and 1.8 NL/(g_{cat}.h), respectively, for both cases. This GHSV value was selected because the flow of consumed CH_4 was lower here, and unstable discharges were also observed at higher GHSV values in the plasma zone. Additionally, the input power was kept constant. Partial oxidation is an exothermic reaction and therefore provides the energy that is needed to heat the catalyst to a certain temperature. Plasma also offers energy to the reaction gas. In other words, the catalyst temperature was self-maintained to an extent by both the elevated temperature of gas in the plasma region and the heat produced by the catalytic reactions [98]. Additionally, the rear side of the reactor was heated with a hot air blower system with a programmable temperature controller. After every 15 °C rise in T_{exit}, the product gas samples were analyzed.

Figs. 5.3a and b shows the H_2 and CO yields, respectively, for both normal and enriched air cases versus the exit bed temperature. The equilibrium and experimental results show that H_2 yields increased to maximum of 86% and 69%, respectively, for both normal and enriched air cases. The equilibrium CO yields for normal air and enriched air increased from 48% to 89% and from 41% to 89%, respectively. The respected increases in CO yields for the experimental results are from 38% to 67% and from 36% to 69%, respectively. As the temperature of the catalyst bed increased, oxidative reactions obviously become more active. The H_2 yield started to decrease at higher temperatures (i.e., >800 °C). In addition to oxidative reactions, endothermic reforming reactions, particularly a WGS reaction, also occurred in this process. The WGS reaction operates favorably at temperatures of 200 to 350 °C. In this study, the exit bed temperature ranged from 600 to 900 °C, which was significantly higher than the typical temperature for a WGS reaction. Accordingly, the WGS reaction reversed and shifted the equilibrium to the left at high temperatures [98]. This reversed WGS reaction produced more CO and increased the yield of CO. In addition, the H_2 yield also started to decrease after 800 °C, which was also attributed to the reverse WGS reaction. This WGS was highly desirable in our experiments because it consumed H_2 and simultaneously formed CO to lower the H_2/CO ratio to a value of 2.

Fig. 5.3c shows the effect of the T_{exit} temperature on the thermal efficiency of the reactor, and the CPO of CH_4 is represented with a solid dashed line for equilibrium values and is compared with the experimental results. At low temperatures, the thermal efficiency was low; as the temperature increased, the selectivity to CO and H_2 yield increased and the conversion of CH_4 also increased. This resulted in high yields of syngas, which in turn increased the thermal efficiency of the process.

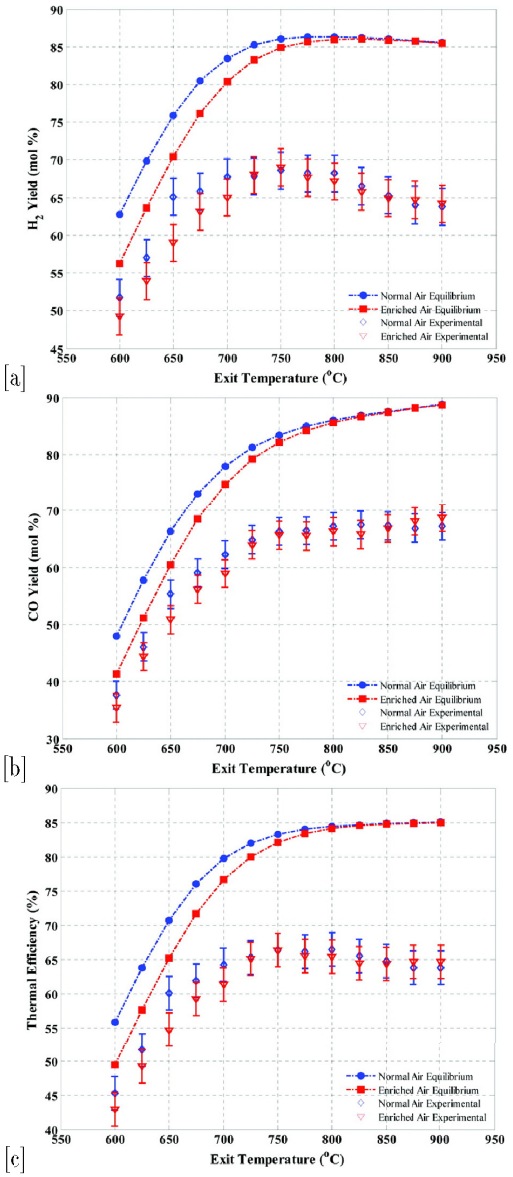

Figure 5.3: (a) Equilibrium and experimental H_2 yield, (b) equilibrium and experimental CO yield, (c) equilibrium and experimental thermal efficiency as a function of T_{exit} at O_2/CH_4 molar ratio=0.7 and GHSV=1.8 NL/(g_{cat}.h).

5.2 Paper B: Modeling and simulation of catalytic partial oxidation of methane to synthesis gas by using a plasma-assisted gliding arc reactor

In the present study, a numerical investigation of the CPO of methane to syngas using a GlidArc reactor is presented. A 2D heterogeneous plug-flow model with radial dispersion and no gradients inside the catalyst pellet are used, including the transport equations for the gas and solid phase and reaction rate equations. The governing equations of this model formed a set of stationary differential algebraic equations coupled with the non-linear algebraic equations, and were solved numerically using in-house MATLAB code. Model results of CPO of methane were compared to previous experimental data with the GlidArc reactor found in the literature. A close match between the calculated and experimental results for temperature, reactant (CH_4 and O_2) conversion, H_2 and CO yields and species mole-fraction were obtained. The developed model was extended to predict and quantify the influence of the GHSV as well as determine the influence of the reactor energy density (RED), the O_2/CH_4 molar ratio and the O_2/N_2 molar ratio. The predicted behaviors for the species mole-fraction, reactants conversion, H_2 and CO yields and temperature along the length of the reactor have been analyzed.

Table 5.1: Comparison between model results and experimental data.

	Case 1: normal air		Case 2: enriched air	
Paramters	Experiment	2D Model[a]	Experiment	2D Model[a]
O_2/CH_4 (mol/mol)	0.7	0.7	0.7	0.7
O_2/N_2 (mol/mol)	21/79	21/79	40/60	40/60
GHSV ($NL/g_{cat}.h$)	1.8	1.8	1.8	1.8
T_{max} (K)	1338	1343	1378	1400
T_{exit} (K)	1073	1053	1073	1107
syngas comp. (mol%)				
CH_4	0.5	0.54	1.2	0.85
CO_2	4	3.77	5.2	5.71
H_2	27.8	29.1	41.1	40.9
CO	13.7	13.9	20.3	20.7
N_2	53.6	52.6	32	31.7
O_2	0	0.029	0	0.078
H_2/CO (mol/mol)	2	2.1	2	1.98
X_{CH_4} (mol%)	98	97.3	96	97.1
X_{O_2} (mol%)	100	99.8	100	99.63
H_2 yield (mol%)	68	72.7	67	67.4
CO yield (mol%)	67	69.6	66	68.4
Reference	[132]	This study	[132]	This study

[a]Calculated using the dissipation term (Eq.(5.3)) in the heat balance of the gas phase to account for the heat loss.

To validate the 2D simulation model, the numerical results were compared with previously reported experimental results [132] obtained under the same conditions; these data are shown in Table 5.1. Table 5.1 compares the reactor performance of the 2D model with the experimental data for the normal air case. Additionally, the validity of the 2D model was confirmed against the experimental results for enriched air case in the same table. It is important to note that, in those experiments, the reactor was not perfectly adiabatic. A dissipation term (Eq.(5.3)) was integrated in the energy balance of the gas phase to account for the heat loss. A global heat transfer coefficient (h_r) was estimated by closely matching the modeled results to the experimental set for normal air and enriched air cases.

$$Q_{lost} = \int_{z_0}^{z_{out}} h_r.\left(T_{gas}\left(x\right) - T_{room}\right).\pi.d_r.dx. \tag{5.3}$$

From Table 5.1, the simulated results of methane and oxygen conversions are in good agreement with the experimental values for both cases. Moreover, the index of dry gas composition (i.e., CH_4, CO_2, H_2, CO, N_2 and O_2), H_2/CO molar ratio and H_2 and CO yields did not vary from the experimental data significantly. However, some deviations for temperature profiles such as T_{max} and T_{exit} were observed. The T_{exit} for the normal air case was slightly underestimated, whereas T_{exit} and T_{max} were overestimated for the normal air cases. The underestimation or overestimation of the temperature cannot, in principle, be ruled out due to experimental errors. Furthermore, the simulated temperature profiles along the reactor coordinates are shown in Figs. 5.4a and b, without and with heat loss models, respectively, for the normal air case. In the case of no heat loss model for the normal air case (Fig. 5.4a), the temperature initially increased due to the large amount of heat produced in the methane oxidation reaction. The temperature reached a maximum value of 1410 K. The temperature decreased consecutively as a result of the prevailing endothermic reforming reaction to the equilibrium temperature of 1350 K. The pronounced temperature increase and subsequent decrease toward equilibrium was characteristic of indirect CPO catalysts [[152],[153]]. The simulation results in the heat loss case model shown in Fig. 5.4b indicated that the catalyst temperature initially increased due to the prevailing methane combustion reaction to 1343 K. Subsequently, the temperature decreased along the length to 1053 K. This result was due to the prevailed endothermic reaction and significant heat loss.

The evolutions of the mole-fraction profiles of the species present in the operations of the CPO process are presented in Fig. 5.5a. The trends based on the solutions of the equations of the models without and with heat loss, respectively, are presented in this figure for the purpose of demonstrating the capability of representing the behavior of the process. The simulated data without heat loss are plotted as solid lines, and the heat loss data are plotted as symbols plus dotted lines. The calculated axial mole-fraction profiles averaged at each cross section (obtained in the case without the heat loss model) indicated that both the methane and oxygen mole fractions decreased rapidly. At z = 0.05 m, approximately 95% of methane

and oxygen had been converted. The reforming and oxidation reactions occurred in parallel; as a result, significant amounts of H_2 and CO were observed, with a trivial amount of CO_2 in the first part of the reactor. In the second part of the reactor, the calculated mole fractions became approximately constant as the equilibrium conditions were approached [154], with the exception of CO_2, which slightly decreased because it reacted with the residual methane to further produce syngas by the CO_2 reforming reaction.

Fig. 5.5a also represents the mole fraction profiles of the species (averaged at each cross section) with heat loss. The simulation results at exit for CH_4, H_2 and the

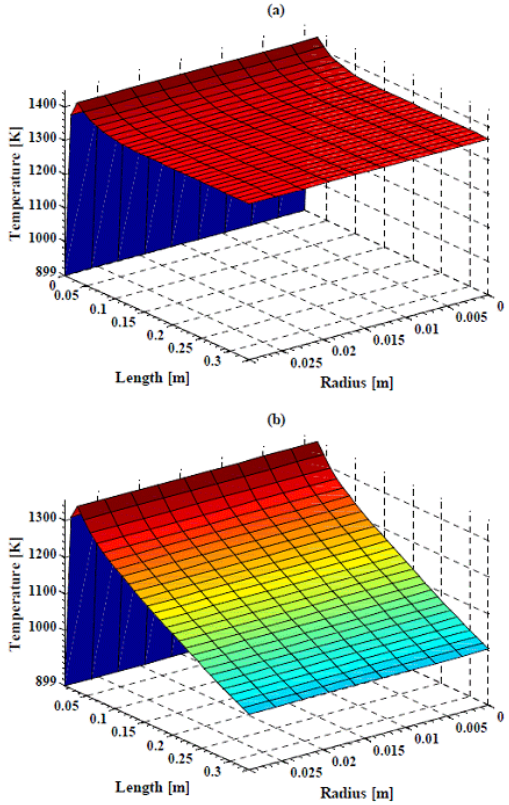

Figure 5.4: Calculated axial and radial temperature profiles along the reactor using a 2D heterogeneous model for syngas production. Reaction conditions: P=1 bar, RED=0.75 kJ/L and GHSV=1.8 NL/(g_{cat}.h). [(a) O_2/CH_4=0.7, O_2/N_2=21/79 for the normal air case without heat loss, (b) O_2/CH_4=0.7, O_2/N_2=21/79 for the normal air case with heat loss].

.

CO mole-fractions were slightly overestimated from the experimental results, and CO_2 was somewhat underestimated, as shown in Table 5.1. The H_2 mole-fraction continuously increased along the length of the reactor. This result was because H_2 was produced from the steam reforming and reverse WGS reactions at a moderate rate. The CO mole-fraction first showed an increasing trend and then decreased along the length, indicating that the steam reforming reaction rate was dominant in the first part, with the reverse WGS reaction being dominant in the second part. The CO_2 mole-fraction continued to increase, indicating the existence of a combustion reaction throughout the reactor length. By comparing the profiles without and with the heat loss model, the trend of species mole-fraction profiles changed.

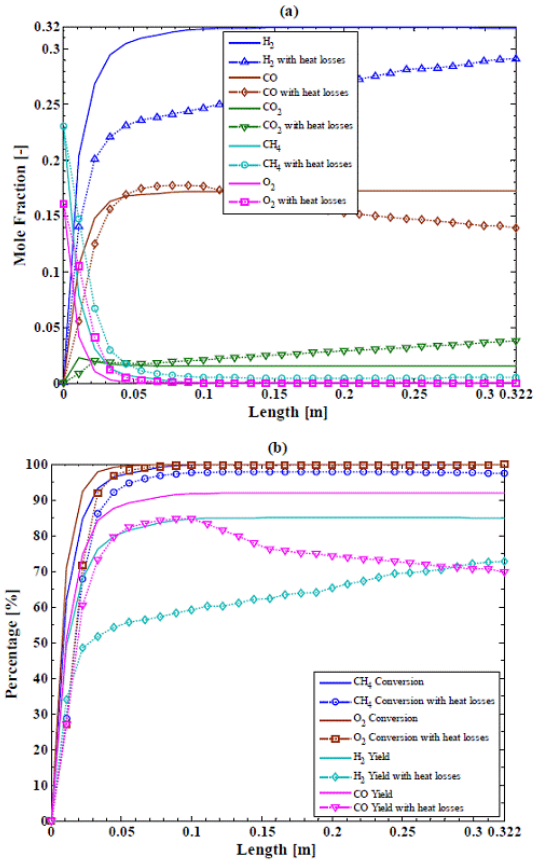

Figure 5.5: Calculated average cross-sectional 2D profiles of the 2D heterogeneous model for syngas production; P=1 bar, RED=0.75 kJ/L and GHSV=1.8 NL/(g_{cat}.h). [(a) species mole-fraction for the normal air case: O_2/CH_4=0.7, O_2/N_2=21/79, (b) reactant conversion and H_2 and CO yields for the normal air case: O_2/CH_4=0.7, O_2/N_2=21/79.]

Modeled (without and with heat loss) methane and oxygen conversion and H_2

and CO yields as a function of reactor length for normal and enriched air cases is depicted in Fig. 5.5b. Experimental data at the exit conditions for these parameters are also given in Table 5.1. It was observed that for both models, most of the methane and oxygen conversion occurred in the first part of the reactor, resulting from high kinetic rates of methane combustion and steam reforming and CO_2 reforming of methane to H_2 and CO. The H_2 yield without the heat loss model became approximately constant after the combustion zone, whereas with the heat loss model, it continued to increase along the reactor length. The CO yield for without the heat loss model also turned out to be stable after the combustion zone but started decreasing in the reformer zone with the heat loss model due to a possible WGS reaction.

5.3 Paper C: Experimental studies and modeling of a fixed bed reactor for Fischer−Tropsch synthesis using biosyngas

The aim of this work was to study the FT synthesis of a model biosyngas (33% H_2, 17% CO and 50% N_2) in a single tube fixed-bed FT reactor. The FT reactor consisted of a shell and tube with high-pressure boiling water circulating throughout the shell. A spherical unpromoted cobalt catalyst was used with the following reaction conditions: a wall temperature of 473 K, a pressure of 20 bars and a GHSV of 37 to 180 NmL/(g_{cat}.h). The performance of the FT reactor was also validated by developing a 2D pseudo-homogeneous model that includes transport equations and reaction rate equations. Good agreement between the model predictions and experimental results were obtained. This developed model was extended to predict and quantify the influence of the FT kinetics as well as determine the influence of the tube diameter and the wall temperature. The predicted behaviors for CO and H_2 conversion, productivity of HCs (mainly CH_4 and $C_5{}^+$) and fluid temperature along the axis of the reactor have been analyzed.

Table 5.2 compares the reactor performance of the 2D model with the experimental data for biosyngas. From this table, the simulated results of CO and H_2 conversions show reasonable agreement with the experimental values for both cases. Moreover, the index of C_1 to C_4, $C_5{}^+$, CO_2 and H_2O selectivity and productivity ($g_{product}$/(g_{cat}.h) did not vary from the experimental data significantly. However, some deviation for CO_2 selectivity at a high GHSV (i.e., 180 Nml/(g_{cat}.h)) was observed.

These experimental results, which were performed to investigate the effect of the GHSV on the performance of unpromoted cobalt catalyst for FT synthesis, show that water is a major product and that its productivity increased with the increase in the GHSV. These values for biosyngas are shown in Table 5.2, and are in agreement with

Table 5.2: Comparison between model results and experimental data for biosyngas as a feed.

	Run 1		Run 2		Run 3	
Paramters	Experiment	2D model	Experiment	2D model	Experiment	2D model
GHSV (NmL/g_{cat}.h)	37	37	74	74	180	180
X_{CO} (mol%)	80	81	52	56	22	27
X_{H_2} (mol%)	83	83	53	58	26	28
C_5^+ (g/g_{cat}.h)	2.46×10^{-3}	2.7×10^{-3}	3.23×10^{-3}	3.85×10^{-3}	3.05×10^{-3}	4.59×10^{-3}
CH_4 (g/g_{cat}.h)	2.24×10^{-4}	2.18×10^{-4}	2.03×10^{-4}	3.01×10^{-4}	2.62×10^{-4}	3.40×10^{-4}
C_2 (g/g_{cat}.h)	1.5×10^{-5}	4.12×10^{-5}	3.74×10^{-5}	5.74×10^{-5}	2.28×10^{-5}	6.59×10^{-5}
C_3 (g/g_{cat}.h)	1.18×10^{-4}	1.15×10^{-4}	1.58×10^{-4}	1.56×10^{-4}	8.95×10^{-5}	1.94×10^{-4}
C_4 (g/g_{cat}.h)	1.32×10^{-4}	1.23×10^{-4}	1.24×10^{-4}	1.74×10^{-4}	9.95×10^{-5}	2.12×10^{-4}
CO_2 (g/g_{cat}.h)	1.89×10^{-4}	1.98×10^{-4}	3.28×10^{-4}	1.92×10^{-4}	7.52×10^{-4}	1.93×10^{-4}
H_2O (g/g_{cat}.h)	4.02×10^{-3}	3.92×10^{-3}	5.27×10^{-3}	5.54×10^{-3}	5.25×10^{-3}	6.59×10^{-3}
% Selectivity						
CH_4	6.27	6.0	4.34	5.94	5.61	5.64
C_2	0.45	1.21	0.85	1.20	0.52	1.17
C_3	3.7	3.47	3.76	3.35	2.17	3.50
C_4	4.16	3.74	2.96	3.79	2.41	3.89
CO_2	1.93	1.98	2.55	1.38	5.87	1.17
C_5^+	83.49	83.60	85.54	84.34	83.42	84.63
ASF (α)	0.76	0.76	0.769	0.769	0.791	0.791

the results from high pressure integral studies [155]. Table 5.2 also shows that CO_2 selectivity increases with an increase in the GHSV for biosyngas. Normally, cobalt is not very active in the WGS reaction. The cobalt catalyst generally shows a low WGS activity at an optimal H_2:CO ratio [[156],[157]], but for a low H_2:CO ratio and N_2 diluted syngas, a small fraction of water produced might be subsequently converted to CO_2. Xu, D. et al. [158] confirmed this small WGS activity by performing WGS experiments over cobalt catalyst under typical FTS conditions. Other than this reaction, CO_2 formation may be possible by the disproportion reaction of CO on the surface of cobalt crystallites according to the Boudouard reaction [[159],[160]].

For biosyngas, CO and H_2 conversion as a function of the GHSV is given in Table 5.2 and shows that the catalyst activity in terms of CO and H_2 conversion was at a maximum (80% and 83%, respectively) at the lowest GHSV and at a minimum (22% and 26%, respectively) at the highest GHSV. Generally, a high GHSV is associated with a low residence time, which causes a decrease in the reactant conversion. These trends were similar to the work reported by Everson and Mulder [161]. Furthermore, Fig. 5.6 supports this explanation by showing the predicted cross-sectional average 2D CO and H_2 conversion profiles along the length of the reactor at different GHSV. The results revealed that at a low GHSV, the reactant conversion was high due to a high residence time. The conversion decreased with an increase in the GHSV.

Product selectivities are expressed as % carbon selectivities. The variations of methane, light HCs (C_2 to C_4) and C_5^+ with GHSV at 200 °C and 20 bars, given in Table 5.2, show that the selectivities of methane and light HCs (C_2 to C_4) decreased, whereas C_5^+ selectivity increased in general. In addition, the productivity of these HCs was found to increase. However, for some GHSVs, there was a slight increase in methane and selectivities of light gaseous products and the decline of C_5^+

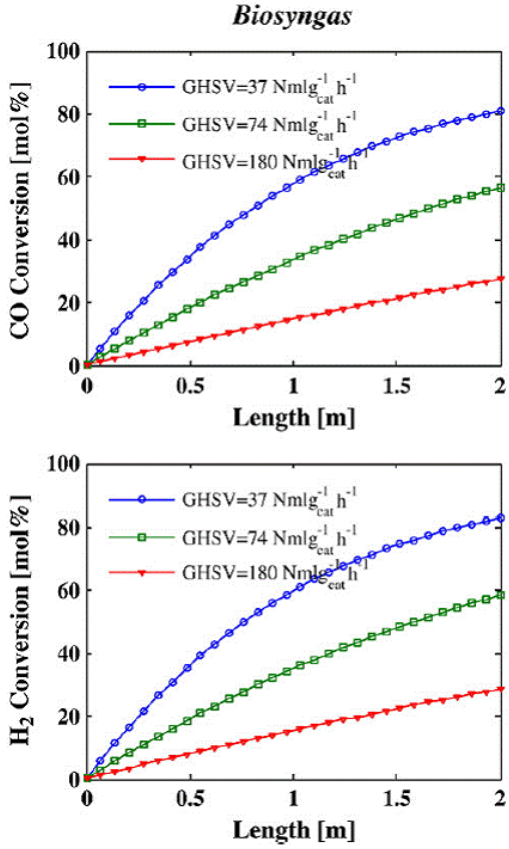

Figure 5.6: Average cross-sectional 2D CO and H_2 conversion profiles of the 2D homogeneous model for FT synthesis; reaction conditions: T_w=473 K, P=20 bar, and tube diameter=27.2 mm.

HCs. However, these changes were not significant compared to the general trends. With increasing GHSVs, diffusion plays a dominant role in the removal of HCs from the catalyst surface to eliminate the mass transfer limitations. Therefore, the selectivity of HCs, especially heavy ones (C_5^+), increased with increasing GHSVs [162]. Another proposed reason for the increase in C_5^+ is due to the presence of higher molecular mass products inside the pores, which would have longer residence time, thus enhancing α-olefin readsorption [163] and increase the partial pressure of water [[164],[165]].Furthermore, the predicted overall FT synthesis productivity of C_5^+ and CH_4 is shown in Fig. 5.7 for both cases. Notably, the desired product was C_5^+, and the undesired product was CH_4. This figure further shows that the increase in the GHSV has an increasing effect on the overall productivity of C_5^+ and CH_4 for both cases.

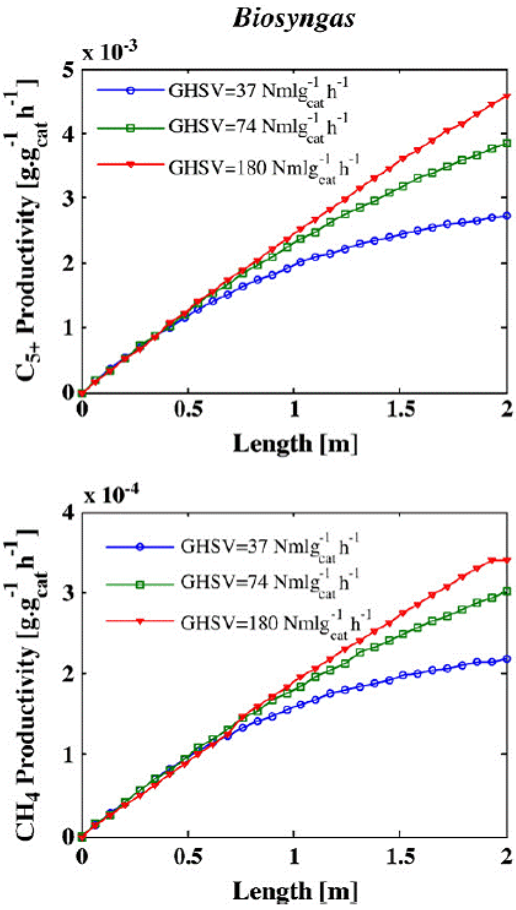

Figure 5.7: Average cross-sectional 2D C_5^+ and CH_4 production rate profiles of the 2D homogeneous model for FT synthesis; reaction conditions: T_w=473 K, P=20 bar, and tube diameter=27.2 mm.

The cross-sectional average 2D temperature profiles are shown in Fig. 5.8. The simulated results clearly indicate that in the low GHSV mode, the temperature along the length of the FT reactor sharply increased (i.e., creating a hot spot) to 476.2 K at the reactor entrance, but the temperature soon dropped close to the given wall temperature. The increase in temperature resulted from a strong contribution of highly exothermic methanation reactions followed by possible coke formation on the catalyst surface by the low GHSV of syngas [166]. In the case of the high GHSV of syngas, the temperature profiles were smoother without any sudden increase (hot spot) in the value, indicating the absence of catalyst deactivation and the occurrence of ongoing exothermic FT synthesis for HC chain growth [9]. The results using

biosyngas show that the increase in the temperature was not sharp, indicating the N_2 content of syngas plays a significant role in the removal of the reaction heat generated by the FT reaction [6].

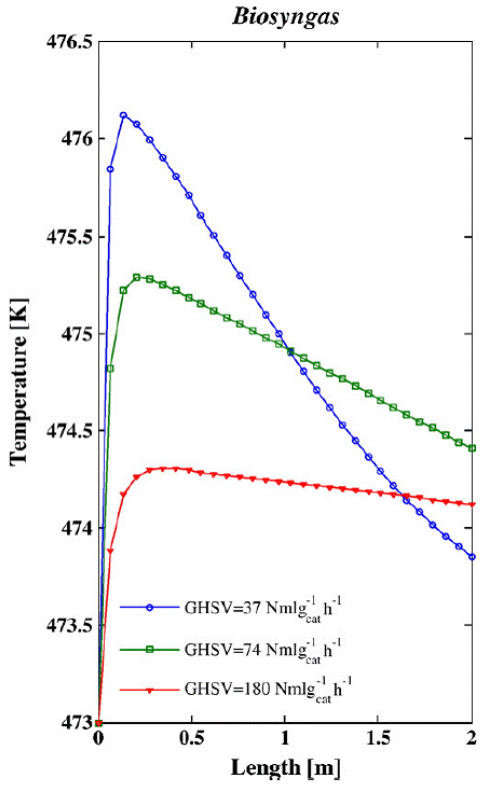

Figure 5.8: Average cross-sectional 2D temperature profiles of the 2D homogeneous model for FT synthesis: reaction conditions: T_w=473 K, P=20 bar, and tube diameter=27.2 mm.

5.4 Paper D: Biosyngas production by autothermal reforming of waste cooking oil with propane using a plasma-assisted gliding arc reactor

Biosyngas production from renewable sources such as biomass has no impact on atmospheric CO_2 levels. In this work, the initial tests results are presented for the conversion of WCO to biosyngas by CPO over a granular Ni-based catalyst. In addition, autothermal reforming of propane with water and normal air was also

carried out. The investigations were performed in a partially adiabatic plasma-assisted (non-thermal) GlidArc reactor at fixed pressure (1 bar) and electric power (0.3 kW). Detailed axial temperature distributions, product concentrations, reactant conversions, H_2 and CO yield, H_2/CO ratio and thermal efficiency, as a function of the cold and hot WCO flow rate, the water flow rate and the time on stream were studied. Propane and normal air were used as oxidizing components to maintain autothermal operation.

Autothermal reforming of propane, water and air

The experimental work was initiated to investigate the possibility of autothermal reforming of propane with air and water. Then tests were carried out to find out the maximum amount of the hot and cold WCO by exploring them in an autothermal reforming operation and by analyzing its characteristics.

First, the effect of the water flow rate on the temperature profiles, carbon conversion, O_2 conversion, CO and H_2 yield and thermal efficiency were investigated. The initial C/O molar ratio of 0.73 was chosen as an optimum ratio based on previously reported values [167]. The experiments were performed at atmospheric pressure and water flow rates between 27.66 and 884.4 mL/h and at a corresponding S/C ratio between 0.064 and 2.10. In addition, the C/O molar ratio was kept constant at 0.734 by fixing the flow rate of the propane and oxygen at 180.2 NL/h and 369.84 NL/h, respectively.

Fig. 5.9a shows the axial temperature profiles after 10 h of operation. In general, each temperature profile along the length of the GlidArc reactor showed that the temperature increased in the plasma zone and then decreased in the catalyst bed. However, by increasing the flow rate of water, the temperature in the plasma zone decreased. These profiles explain that with the increase in the flow rate of water and at a varying S/C ratio, the promotional effect of the plasma was less pronounced. This result can be explained by the loss of energy absorbed by the excess water, which has been confirmed by Tao et al. [101]. In practice, a high water flow rate required more energy for the water, and this was not desirable from an energy efficiency point of view. Moreover, these temperature profiles along the catalyst bed demonstrate that with the increased water flow rate, the temperature in the catalyst bed increased slightly. It is well accepted that oxidation reactions and reforming reactions appear to occur in varying predominance over the length of a GlidArc reactor. The temperature profiles, recorded for all the water flow rates, show clearly that the exothermic oxidation reactions tend to predominate in the initial part of the reactor, whereas the endothermic reforming reactions predominate in the downstream portion [168].

Examination of the effect of increasing the water flow rate at its corresponding S/C ratio on the carbon conversion to gaseous products, O_2, CO and H_2 yield and thermal efficiency of GlidArc is shown in Fig. 5.9b. It was observed that at a

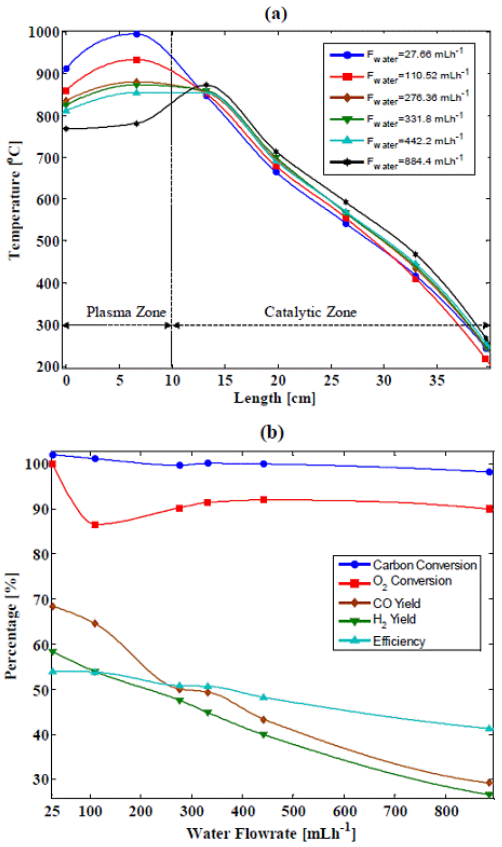

Figure 5.9: (a) The temperature profiles along the length of the GlidArc reactor, (b) the carbon conversion, O_2 conversion, thermal efficiency, and CO and H_2 yields as a function of the water flow rate.

preliminary water flow rate of 27.66 mL/h, S/C ratio of 0.064 and SV of 0.7532 NL/(g_{cat}.h), the carbon conversion, O_2 conversion, CO and H_2 yield and thermal efficiency were 102%, 100%, 68.4%, 58.4% and 54%, respectively. By increasing the water flow rate to 884.4 mL/h, S/C ratio to 2.01 and SV to 0.7547 NL/(g_{cat}.h), the carbon conversion, O_2 conversion, CO and H_2 yield and thermal efficiency were 98%, 90%, 29%, 27% and 41%, respectively. These results show that all of these parameters were high at the lowest water flow rate. The effect of increasing the water flow rate is apparent because as the S/C ratio increases, the carbon conversion, O_2 conversion, syngas yield and thermal efficiency decreases. The values greater than 100 for the conversion of carbon species were likely due to experimental error, although a small amount may also be attributable to the cleansing of some coke that was deposited before the GlidArc reactor achieved steady state. The values

less then 100 for the conversion of carbon species were likely due to an indication of coke formation.

Autothermal reforming of WCO, propane and air

In the second part of the study, a series of experiments were performed to explore the possibility of autothermal reforming of WCO a temperature of 350 °C. Further heating was avoided due to thermal cracking of the WCO. The experiments were performed at atmospheric pressure and WCO flow rates between 27.33 and 166.66 mL.h-1 at an equivalent C/O ratio between 0.782 and 1.026. The propane and oxygen flow rate were kept constant at 180.21 NL/h and 369.84 NL/h, respectively.

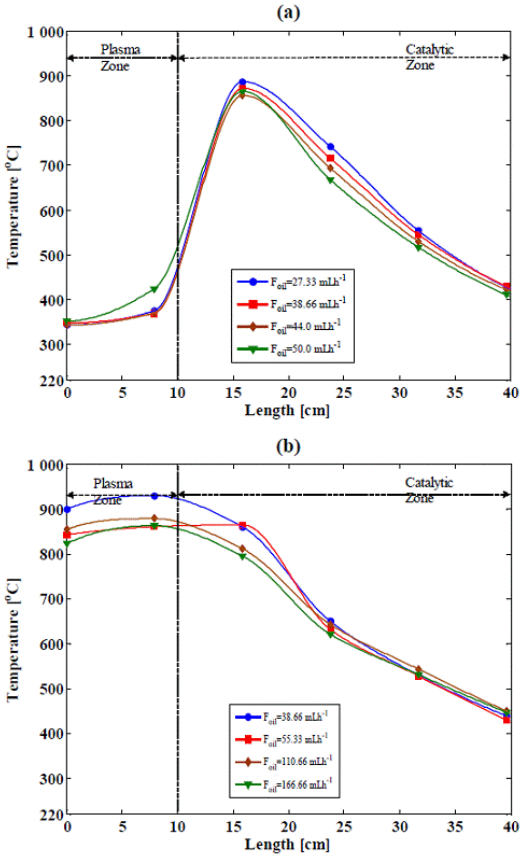

Figure 5.10: The axial temperature profiles as a function of the WCO flow rate, (a) after a time on stream of 2 h with hot WCO, (b) after a time on stream of 10 h with hot WCO.

Fig. 5.10a depicts the temperature profiles along the length of the GlidArc

reactor after 2 h of operation. Hot WCO with flow rates from 27.33 to 50.0 mL/h was used. These trends show that the point of maximum reactor temperature was located in the upper part of the catalyst bed. The effect of hot WCO with flow rates from 38.66 to 166.66 mL/h after 10 h of operation is shown in Fig. 5.10b. The amount of WCO was higher in Fig. 5.10b because after 10 h, the GlidArc reactor was stabilized; it's inside temperature increased, so the capability of the Arc to reform the WCO to soot free syngas was also improved. All of these profiles show that the temperature in the plasma zone was higher than it was in the catalyst zone. The results depicted in Fig. 5.10a show that most of the exothermic reactions (i.e., partial oxidation and complete oxidation) occurred in the upper part of the catalyst bed. These exothermic reactions create distinctive bed gradients, in which all the free oxygen was consumed. This was then followed by a second, but much slower, endothermic reforming stage (i.e., steam reforming and water gas shift). However, in Fig. 5.10b, the results show that after 10 h of operation and injection of the hot WCO, most of the exothermic reactions took place in the plasma zone. In the catalytic zone, mainly endothermic reforming reactions occurred.

The carbon conversion to gaseous products, O_2 conversion, CO and H_2 yield and thermal efficiency as a function of the hot WCO after 2 h of operation is depicted in Fig. 5.11a. The results indicate that the O_2 conversion, CO and H_2 yield and thermal efficiency increased, and the carbon conversion to gaseous products slightly decreased upon increasing the hot WCO flow rate. Fig. 5.11b shows the effect of the hot WCO on the carbon conversion to gaseous products, O_2 conversion, CO and H_2 yield and thermal efficiency after 10 h of operation. The results indicate that the O_2 conversion, CO and H_2 yield and thermal efficiency increased, and the carbon conversion to gaseous products increased with the increase in the hot WCO flow rate.

The results shown in Figs. 5.10 and 5.11 indicate that the time on stream and temperature inside the GlidArc reactor were important for the reforming characteristic of the WCO. The reactor achieved steady state operation after time on stream of 10 h. The product concentration changed, the temperature inside the GlidArc reactor increased as did the O_2 conversion, CO and H_2 yield of biosyngas and thermal efficiency with a decrease in the carbon conversion to gaseous products. The carbon conversion to gaseous products was not always complete, and carbon deposits were found on the catalyst surface. The H_2 and CO yields were lower at the lower temperature due to the formation of methane as a result of the hydrogenation of CO. The WGS and hydrogenation or methanation of CO consumed the CO produced at all WCO flow rates. With the progress of time, the temperature of the GlidArc increased, and that increased the yield of CO and H_2 as a result of an increase in the improved steam gasification of coke. WCO has a tendency to form higher amounts of coke compared to the ethanol or methanol. Therefore, an increasing temperature promoted coke gasification [169].

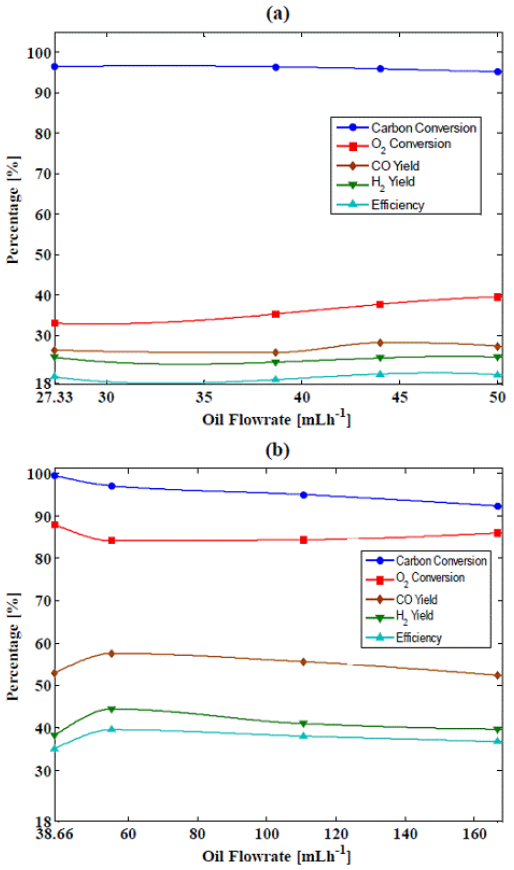

Figure 5.11: The carbon conversion, O_2 conversion, thermal efficiency, H_2 and CO yields profiles as a function of the WCO flow rate, (a) after a time on stream of 2 h with hot WCO, (b) after a time on stream of 10 h with hot WCO.

5.5 Paper E: Experimental and thermodynamic studies of the catalytic partial oxidation of model biogas using a plasma-assisted gliding arc reactor

The present work is an investigation of the influence of process conditions on the production of syngas from model biogas (molar ratio of CH_4/CO_2=60/40) through partial oxidation over a granular Ni-based catalyst. The investigations were performed in a partially adiabatic plasma-assisted (non-thermal) GlidArc reactor in a

transitional flow regime at a fixed pressure (1 bar) and electric power (0.3 kW). The emphasis of this investigation was on an experimental study and a comparative thermodynamic analysis. The equilibrium compositions were calculated using a Lagrange multiplier and resulted in the development of systems of non-linear algebraic equations, which were solved numerically using the MATLAB function "fmincon". Two cases were studied: normal air (molar ratio of O_2/N_2=21/79) and enriched air (O_2/N_2=40/60). The individual effects of the O_2/CH_4 molar ratio and the T_{exit} were studied in both cases. The main trends of the CH_4 conversion, the syngas yield, the H_2/CO ratio and the thermal efficiency of the reactor were analyzed.

Effect of O_2/CH_4 molar ratio

The equilibrium and experimental product molar concentrations on a dry basis for normal air are shown in Figs. 5.12a and b, respectively. To compare the equilibrium and experimental calculations, the molar concentration profiles were plotted for a given O_2/CH_4 molar ratio and its corresponding value of T_{exit} and GHSV, meaning that the value of T_{exit} and the GHSV were different at each O_2/CH_4 molar ratio. At a O_2/CH_4 ratio of 0.44, the measured values of T_{exit} and GHSV were 430 °C and 0.98 NL/(g_{cat}.h); at a ratio of 0.66, the measured values were 630 °C and 1.26 NL/(g_{cat}.h); at a ratio of 0.78, the measured values were 680 °C and 1.4 NL/(g_{cat}.h); at a ratio of 0.89, the measured values were 684.5 °C and 1.54 NL/(g_{cat}.h); and at a ratio of 1.33, the measured values were 800 °C and 2.1 NL/(g_{cat}.h). The equilibrium molar concentration result in Fig. 5.12a shows that when the molar ratio was increased from 0.44 to 0.66, the CH_4 and CO_2 molar concentrations dropped, and the H_2 and CO molar concentrations increased to reach their maximal values. When this molar ratio was further increased, the CH_4 molar concentration continued to decrease, but the CO_2 molar concentration began to increase, and the syngas molar concentration started to decrease. These results demonstrate that at higher ratios, the combustion reaction was more favorable than the other reforming reactions. The experimental results in Fig. 5.12b show similar trends as those in Fig. 5.12a with some deviations. Zhu et al. [145] showed a similar equilibrium trend for the product molar concentration; however, their study was performed at different initial molar ratios of CO_2/CH_4.

The syngas yield, thermal efficiency, CH_4 conversion and CO_2 conversion results are reported in Figs 5.13a and b for the normal air case. The equilibrium results in Fig. 5.13a show that the CH_4 conversion increased to 98%, and the CO_2 conversion was approximately 0% at a molar ratio of 0.78; as CO_2 was formed, CO_2 conversion became more negative. The H_2 and CO yields increase with increases in molar ratio up to 0.78, from this point the yields decrease with further increases in the molar ratio. The thermal efficiency was also dependant on the amount of syngas produced, reaching a maximum value of 69% at an O_2/CH_4 molar ratio of 0.78 (Fig. 5.13a). The experimental results in Fig. 5.13b show a similar trend as these equilibrium trends.

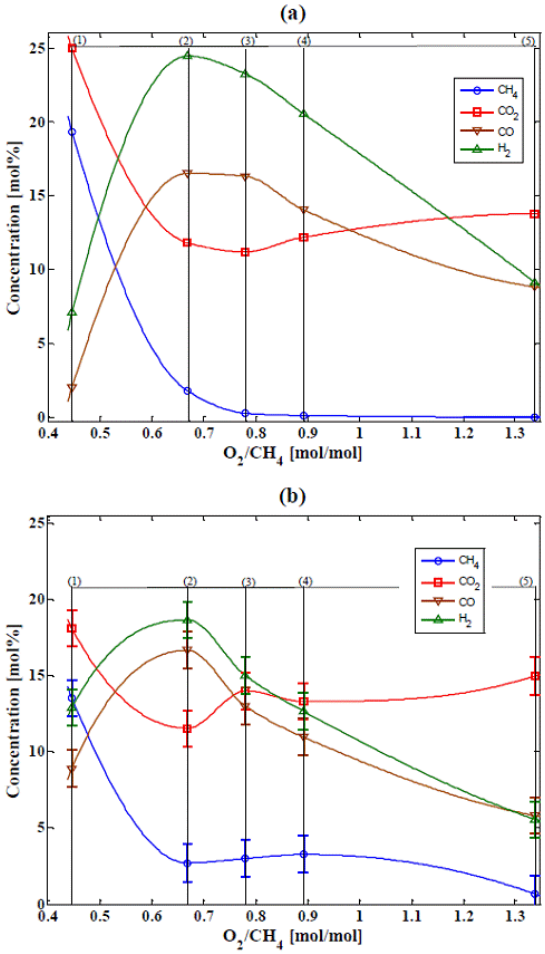

Figure 5.12: (a) Equilibrium and (b) experimental molar concentration profiles for the normal air case as a function of the initial O_2/CH_4 molar ratio at the corresponding T_{exit} and GHSV [(1) 430 °C, 0.98 NL/(g_{cat}.h), (2) 630 °C, 1.26 NL/(g_{cat}.h), (3) 680 °C, 1.4 NL/(g_{cat}.h), (4) 684.5 °C, 1.54 NL/(g_{cat}.h), (5) 800 °C, 2.1 NL/(g_{cat}.h)]. Pressure = 1 bar, CO_2/CH_4 = 0.66 and O_2/N_2 = 0.265.

The results shown in Figs. 5.12 and 5.13 indicate that although some of the experimental values at some O_2/CH_4 ratios were close to the equilibrium values, most of the values differed significantly from the equilibrium values. This difference could be related to irregular gas flow, which was primarily caused by an irregular catalyst particle size (granular form). In addition, the design of the GlidArc reactor allowed some of the model biogas to pass through the reactor without proper contact with the catalyst because the ratio of the inner reactor diameter (*i.d.* = 59 mm) to

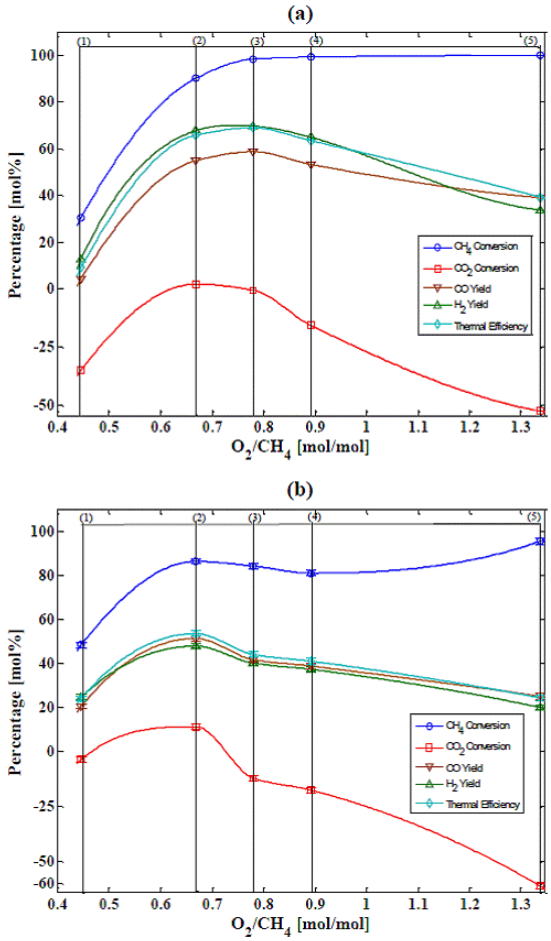

Figure 5.13: (a) Equilibrium and (b) experimental CH_4 conversion, CO_2 conversion, thermal efficiency, and H_2 and CO yield profiles for normal air as a function of the initial O_2/CH_4 molar ratio at the corresponding T_{exit} and GHSV [(1) 430 °C, 0.98 NL/(g_{cat}.h), (2) 630 °C, 1.26 NL/(g_{cat}.h), (3) 680 °C, 1.4 NL/(g_{cat}.h), (4) 684.5 °C, 1.54 NL/(g_{cat}.h), (5) 800 °C, 2.1 NL/(g_{cat}.h)]. Pressure =1 bar, CO_2/CH_4=0.66 and O_2/N_2=0.265.

the average catalyst particle size ($d_{p,avg}$ = 10 mm) was large [170]. An additional factor that might play a role in the observed temperature difference was the lack of perfect insulation of the GlidArc reactor, which created large temperature gradients between the arc and the surrounding area as well as a gradient along the length of the catalyst bed, possibly causing a strong radial shear stress on the reactor diameter [171].

Effect of temperature

In the second part of the study, a series of experiments were performed in a transitional regime. In these sets of experiments, the value of the O_2/CH_4 molar ratio was kept constant at 0.66 with a constant GHSV of 1.26 NL/(g_{cat}.h) for normal air. Additionally, the input power was kept constant. Partial oxidation is an exothermic reaction and therefore provides the energy that is needed to heat the catalyst to a certain temperature. Plasma also offers energy to the reaction gas. In other words, the catalyst temperature was self-maintained to an extent by both the elevated temperature of gas in the plasma region and the heat produced by the catalytic reactions [98]. Additionally, the rear side of the reactor was heated with a hot air blower system with a programmable temperature controller.

The equilibrium product molar concentrations of H_2 and CO increased and the CH_4 and CO_2 molar concentrations decreased with increasing T_{exit}, as shown in Fig 5.14a for the normal air case. The corresponding experimental values are shown in Fig 5.14b. The experimental trends are in accordance with the equilibrium results, but the values are somewhat lower, possibly because of temperature gradients inside the reactor. The equilibrium H_2 molar concentration decreased at temperatures greater than 700 °C because of the reverse WGS reaction.

As shown in Fig 5.15a, when the T_{exit} increased, equilibrium CH_4 conversion increased because more CH_4 was converted to syngas. The experimental results, shown in Fig 5.15b, are in good agreement with the equilibrium results. Between T_{exit} values of 380 °C to 540 °C, the CO_2 equilibrium and experimental conversions differed greatly. At a T_{exit} of 630 °C, the experimental results were comparable to the equilibrium results for both cases (approximately 0%). This 0% CO_2 conversion shows that a balance exists between the CO_2-consuming reactions and the CO_2-producing reactions. However, when the value of T_{exit} was further increased, the equilibrium CO_2 conversion increased, but the experimental trends were somewhat different.

The equilibrium H_2 yield, as shown in Fig 5.15a, increased with an increase in the value of T_{exit} from 380 °C to 700 °C. The equilibrium CO yield for both cases increased with an increase in T_{exit}. The thermal efficiency increased with an increase in T_{exit}. At low values of T_{exit}, the thermal efficiency was low; as the temperature increased, the selectivity to CO and H_2 increased, and the conversion of CH_4 increased. This resulted in high yields of syngas, which in turn increased the thermal efficiency of the process. The experimental trends were similar, but there were some deviations from the equilibrium calculations, suggesting that the temperature inside the reactor may not have been perfect.

The experimental and equilibrium results shown in Figs. 5.14 and 5.15 indicate that as the temperature of the catalyst bed increased, the oxidative reactions became more active. The H_2 yield decrease at temperatures greater than 700 °C. In addition to the oxidative reactions, endothermic reforming reactions, particularly a

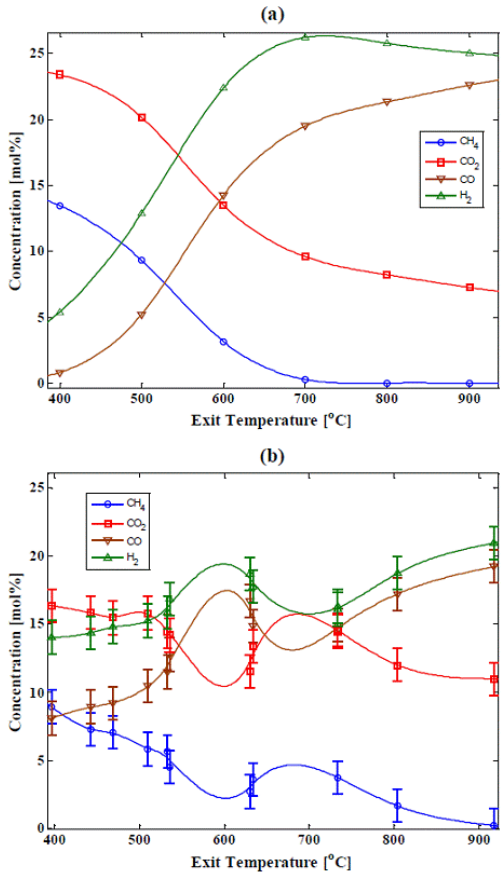

Figure 5.14: (a) Equilibrium and (b) experimental molar concentration profiles for the normal air case as a function of T_{exit} at a pressure of 1 bar [O_2/CH_4=0.66, CO_2/CH_4=0.66, O_2/N_2=0.265 and GHSV=1.26 NL/(g_{cat}.h)]. Additional heat was supplied by an electric hot air blower.

WGS reaction, occurred in this process. The WGS reaction operates favorably at temperatures of 200 °C to 350 °C. In this study, the T_{exit} was significantly higher than the typical temperature for a WGS reaction. Accordingly, the WGS reaction reversed and shifted the equilibrium to the left [98]. This reversed WGS reaction produced more CO, thereby increasing its yield. In addition, the H_2 yield decreased at temperatures greater than 700 °C, which was also attributed to the reverse WGS reaction.

The effects of the O_2/CH_4 molar ratio and T_{exit} were studied in detail through repeated preliminary experiments in the developed non-thermal plasma GlidArc reactor. From these investigations, the optimal conditions resulting in approximately

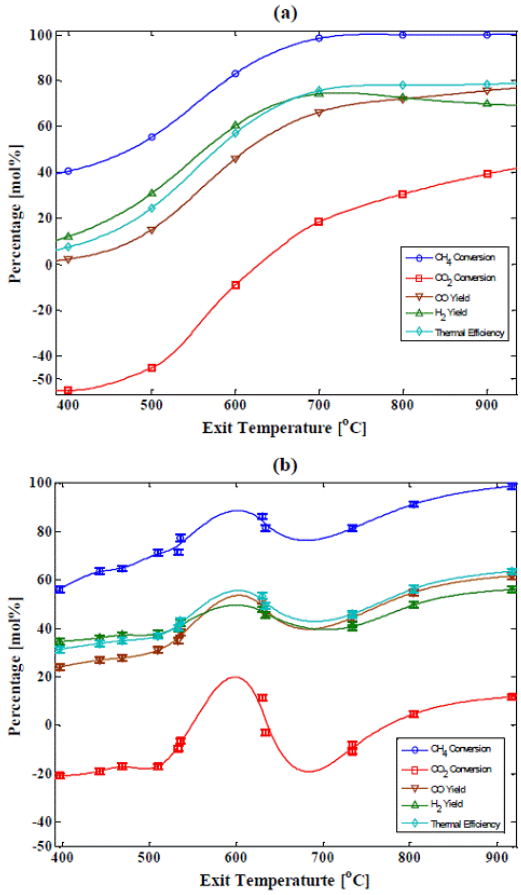

Figure 5.15: (a) Equilibrium and (b) experimental CH_4 conversion, CO_2 conversion, thermal efficiency, and H_2 and CO yield profiles for the normal air case as a function of T_{exit} at a pressure of 1 bar [O_2/CH_4=0.66, CO_2/CH_4=0.66, O_2/N_2=0.265 and GHSV=1.26 NL/(g_{cat}.h)]. Additional heat was supplied by an electric hot air blower.

0% CO_2 conversion were identified. The results are presented in Table 5.3. In addition, the results obtained in a study using a cold plasma jet developed by Long et al. [172] are shown to compare the reforming results with and without catalyst. The 12% Ni/γ-Al_2O_3 catalyst was placed after the plasma discharge zone. At the total flow rate of 16.7 L/min, a GHSV of 66.66 NL/(g_{cat}.h), a CO_2/CH_4 molar ratio of 1.5 and an input power of 0.77 kW, the conversions of CH_4 and CO_2 were 60% and 40% respectively, and the yield of CO and H_2 was 54% and 44%, respectively. Compared with that without catalysts, the conversions were 46% and 34%, and the yield was 36% and 33%, respectively. The efficiency also increased with the addition of catalyst from 63% to 80%. The results of study by Indarto et al. [173] using a

non-catalytic GlidArc discharge are also given. At a total feed gas flow rate of 1 L/min, a discharge power of 0.19 kW and a CO_2/CH_4 ratio of 1, the conversions of CH_4 and CO_2 were approximately 40% and 31%, respectively. The yields of CO and H_2 were 20% and 25%, respectively, and the corresponding efficiency was 28.

Table 5.3: Summary (error ±2.5%).

Paramters	Case 1: normal air		Other studies		
	Equilibrium	Experimental	Cold plasma jet $+Ni/Al_2O_3$	Cold plasma jet discharge	Gliding arc
O_2/CH_4 (mol/mol)	0.66	0.66	-	-	-
CO_2/CH_4 (mol/mol)	0.66	0.66	1.5	1.5	1.0
Gas flow rate (L/min)	16.7	16.7	16.66	16.66	1.0
GHSV ($NL/g_{cat}.h$)	1.26	1.26	-	66.66	-
T_{max} (°C)	870	870	-	-	-
T_{exit} (°C)	630	630	-	-	-
syngas comp. (mol%)				-	-
CH_4	2.0	2.71	-	-	-
CO_2	11.55	12	-	-	-
H_2	24	18.65	-	-	-
CO	16.8	16.6	-	-	-
N_2	45.5	49	-	-	-
C_2^+	<1	1	-	-	-
H_2/CO (mol/mol)	1.43	1.12	0.8	1.0	0.9
X_{CH_4} (mol%)	89	86	46	60	40
X_{CO_2} (mol%)	0	4	34	40	31
H_2 yield (mol%)	67	48	33	44	25
CO yield (mol%)	52	51	36	54	20
Thermal efficiency η (mol%)	65	54	63	80	28
Reference	This study	This study	[172]	[172]	[173]

Chapter 6

Conclusions and future work

The application of fixed-bed reactor for syngas production and FT synthesis was emphasized in this work.

GlidArc plasma-assisted reformers have several advantages, including a minimum start time, stable operation with a wide variety of heavy HCs fuels reforming and a low electrical energy consumption (2% to 5% of the total chemical energy of the system). The preceding text covered the thermodynamic analysis followed by the experimental verification for various syngas properties for two cases: (i) normal air and (ii) air enriched via CPO of CH_4 using a non-thermal plasma GlidArc reactor. For an increasing O_2/CH_4 molar ratio at a fixed GHSV, the trend demonstrated that the CH_4 conversion, T_p, T_{max} and T_{exit} increased for both cases, whereas the syngas yield and LHV efficiency first increased because of the reforming reactions, but then decreased due to the combustion reaction. The effect of the GHSV at a fixed O_2/CH_4 molar ratio showed that the reforming reactions were also influenced by an increase in the GHSV. The CH_4 conversion, reactor temperatures, syngas yield and reactor thermal efficiency increased, while the H_2/CO ratio decreased with an increase in the GHSV. The effect of the T_{exit} at fixed O_2/CH_4 molar ratio and GHSV for both cases showed that for an increasing T_{exit}, the H_2/CO ratio decreased, whereas the CH_4 conversion, the syngas yield and the LHV efficiency increased for both cases. The temperature along the reactor varied significantly, even for a constant GHSV. The syngas yield, CH_4 conversion and thermal efficiency of the reactor are temperature dependent and so are strongly affected due to temperature variations at a constant GHSV. The experimental results were in agreement with these thermodynamic calculations. The deviations from the thermodynamic calculations could be explained by temperature gradients along the length of the reactor because of heat losses and irregular gas flow due to an uneven and irregular catalyst diameter. The results showed that an H_2/CO ratio of 2 could be obtained. For the normal air case, an optimal value of the O_2/CH_4 molar ratio of 0.7, a GHSV of 1.8 NL/(g_{cat}.hr) and a maximum temperature (T_{max}) of 1065 °C were good reforming choices, while for enriched air, these values were 0.7, 1.8 and 1105 °C, respectively.

A 2D heterogeneous model was developed to simulate the CPO of methane to syngas using a GlidArc reactor. The main global surface reactions for methane were included in the model, which consisted of the total combustion, steam reforming, dry reforming and the water gas shift reaction. The governing equations included conservation of mass, momentum, energy and chemical species and the ideal gas mixture equation of the state and pressure drop equation. An in-house MATLAB code based on a finite difference method was developed to solve the non-linear, coupled governing equations. This reactor model was validated against the experimental data reported in the literature, and a good agreement was found between the experimental results and the model predictions. Furthermore, a comprehensive modeling study of the effects of process parameters on the CPO GlidArc reactor performance was also conducted. It was predicted that an increase in GHSV would increase the mole-fraction of CH_4, O_2, H_2O and CO_2, while it would decrease the mole-fraction of H_2 and CO. However, higher GHSV also reduced the reactants conversion and H_2 and CO yields. The temperature peak increased as the GHSV increased but was shifted toward the reactor exit. By increasing the RED, the predicted CH_4, H_2O and CO_2 mole-fractions decreased, whereas the H_2 and CO mole fractions increased. In addition, an increase in the RED also resulted in an increase in the reactants conversion and H_2 and CO yields. The hot spot also shifted up to the front part of the reactor. The CPO of methane in the reactor was predicted to be very sensitive to the O_2/CH_4 molar ratio. By increasing the O_2/CH_4 molar ratio, the CH_4, CO and H_2 mole-fractions decreased in a continuous manner, but a momentous increase in the H_2O mole-fraction and a slight increase in the CO_2 mole-fraction were observed. Moreover, increasing the O_2/CH_4 ratio increased the reactor temperature and improved the methane conversion, but decreased the overall syngas yield. With an increase in the O_2/N_2 molar ratio, the H_2, CO and H_2O mole-fractions increased, whereas the CH_4 and CO_2 mole-fractions slightly decreased. The results indicated that the temperature in the reactor increased, and the CO yield increased; however, the methane conversion and H_2 yield showed fluctuating behaviors with an increase in the O_2/N_2 molar ratio.

FT synthesis of model biosyngas at different GHSVs and a fixed wall temperature (493 K) and pressure (20 bars) was successfully evaluated in a fixed-bed reactor experimentally. Generally, CO and H_2 conversion reached a maximum at a low GHSV. The selectivities of CH_4 and C_1 to C_4 HCs decreased, while $C_5{}^+$ selectivity and productivity of HCs increased with an increase in the GHSV. A 2D pseudo-homogeneous model was also developed to simulate this fixed bed FT reactor. This reactor model was tested against the experimental data, and good agreement was found between the experimental results and model predictions. A comprehensive modeling study of the effects of process parameters on the FT synthesis performance was also conducted using industrial conditions. It was predicted that the increase of catalyst activity would increase the CO and H_2 conversion and enhance the overall productivity of $C_5{}^+$ and CH_4 products. A larger increase in temperature was observed upon the addition of more active catalyst material. An increase in

the tube diameter resulted in an increase of CO and H_2 conversion with a minor improvement in C_5^+ productivity but a major increase in the CH_4 productivity. The hot spot also shifted down to the rear part of the FT reactor. By increasing the wall temperature, the CO and H_2 conversion and C_5^+ productivity increased in a continuous manner, but a momentous increase in the CH_4 productivity was observed. However, upon increasing the wall temperature, the temperature runaway in the system was occurred most likely due to the release of extensive heat of reaction from the FT synthesis.

Experimental studies were performed for various synthesis properties for water, cold and hot WCO flow rate and time on stream using a non-thermal plasma GlidArc reactor. With an increase in the water flow rate and at the corresponding S/C molar ratio, the H_2, CO_2 and C_2^+ concentrations increased, whereas the CO and CH_4 concentrations decreased. In addition the carbon conversion to gaseous products, O_2 conversion, CO and H_2 yield and thermal efficiency decreased. The effect of the cold and hot WCO flow rate after a time on stream of 2 h and 10 h at a fixed propane and air flow rate showed that for an increased WCO flow rate at the corresponding C/O molar ratio, the H_2, CO and CO_2 concentrations increased, the C_2^+ concentration slightly decreased, but the CH_4 concentration almost remained constant. The results also indicated that the O_2 conversion, CO and H_2 yield and thermal efficiency increased, and the carbon conversion to gaseous products decreased with the increase in the cold and hot WCO flow rate after time on stream of 2 h and 10 h. By comparing the results of the time on stream, it can be observed that when the GlidArc reactor was stabilized (i.e., after 10 h of operation), the temperature in the GlidArc reactor increased. The H_2, CO, CO_2 and CH_4 concentrations increased, and the C_2^+ concentration decreased for the same WCO flow rates. In addition, the O_2 conversion, CO and H_2 yield of biosyngas and thermal efficiency increased, and the carbon conversion to gaseous products decreased. The carbon conversion to gaseous products was not always complete, and some carbon deposits were found on the catalyst surface. Finally, the results showed that GlidArc reactor reformed higher amount of water than hot and cold WCO.

The thermodynamic analysis and experimental verification for the production of syngas with (i) normal air and (ii) enriched air using CPO of a model biogas with a non-thermal plasma GlidArc reactor was analyzed. For an increasing O_2/CH_4 molar ratio and at a corresponding GHSV, the CH_4 conversion, T_{max} and T_{exit} increased for both normal and enriched air, and the syngas yield, thermal efficiency and the CO_2 conversion first increased because of the reforming reactions but then decreased due to the combustion reaction. For an increasing T_{exit} at a fixed O_2/CH_4 molar ratio and GHSV for both cases, the H_2/CO ratio decreased, and the CH_4 conversion, the CO_2 conversion, the syngas yield and the thermal efficiency increased. The temperature along the reactor varied significantly, even with a constant GHSV. The syngas yield, CH_4, CO_2 conversion and thermal efficiency of the reactor are temperature dependent and are therefore strongly affected by temperature variations at a constant GHSV. The experimental results deviated from the thermodynamic calcu-

lations, possibly because of temperature gradients along the length of the reactor as a result of heat losses and irregular gas flow due to an uneven and irregular catalyst diameter. The results demonstrated that CO_2 could be used as a neutral gas at the a T_{exit} of 630 °C , an O_2/CH_4 ratio of 0.66 and a GHSV of 1.26 NL/(g_{cat}.h) for normal air and at a T_{exit} of 635 °C, an O_2/CH_4 ratio of 0.64 and a GHSV of 0.76 NL/(g_{cat}.h) for enriched air.

Future work

Significant work remains to be done with regards to the comparison of the processes; in particular reforming without plasma, for which carbon formation will be expected to play an important role. For this purpose, a 60 kW non-thermal plasma-assisted GlidArc reforming system is designed and built. These investigations (i.e., with and with out plasma) should be conducted using different gaseous fuels, WCO and other liquid fuels such as low- and high-lignin biomass pyrolysis oils, waste tires pyrolysis oils and industrial/vehicle waste oils in the future to study and further compare the claims (i.e., with plasma) of increased products yield, efficiency and reactant conversions.

For some of the results, the carbon conversion to gaseous products was not always complete, and some carbon deposits were found on the catalyst surface. It appeared harmless to the catalyst, at least during relatively short tests. Carbon deposits accumulated on the front face of the catalyst and was brushed off periodically, allowing the catalyst to be reused. Many of the direct catalytic reforming experiments were performed on catalysts reused in this manner with good result. However, the time frame for the total life of the catalyst, several tens of hours, was too short to draw meaningful conclusions about the loss of catalyst activity. Future investigation into this issue is suggested.

For FT synthesis, the developed and validated reactor model is a valuable tool in predicting the performance of the reactor. In addition, the model gives a reasonable level of confidence for the scale-up of this laboratory reactor to a future industrial reactor. However, for the present time, the most important uncertainties are linked to the new active catalyst, its kinetic parameters and its range of operating conditions. To determine these parameters, experiments are recommended in a small-scale laboratory reactor.

Bibliography

[1] J.-P. Lange. Lignocellulose conversion: an introduction to chemistry, process and economics. Biofuels, Bioproducts and Biorefining. 1 (2007) 39-48.

[2] A. Steynberg, M. Dry, M.E. Davis, B.B. Breman. Fischer-Tropsch Technology. Elsevier, Amsterdam, 2004.

[3] A. Czernichowski. GlidArc assisted preparation of the synthesis gas from natural and waste hydrocarbons gases. Oil Gas Science and Technology - Rev IFP. 56 (2001) 181-98

[4] J.M. Cormier, I. Rusu. Syngas production via methane steam reforming with oxygen: plasma reactors versus chemical reactors Journal of Physics D: Applied Physics. 34 (2001) 2798-803.

[5] E.S. Lox, G.F. Froment. Kinetics of the Fischer-Tropsch reaction on a precipitated promoted iron catalyst. 1. Experimental procedure and results. Industrial Engineering Chemistry Research. 32 (1993) 61-70.

[6] A. Jess, R. Popp, K. Hedden. Fischer-Tropsch-synthesis with nitrogen-rich syngas: Fundamentals and reactor design aspects. Applied Catalysis A: General. 186 (1999) 321-42.

[7] K.-W. Jun, H.-S. Roh, K.-S. Kim, J.-S. Ryu, K.-W. Lee. Catalytic investigation for Fischer-Tropsch synthesis from bio-mass derived syngas. Applied Catalysis A: General. 259 (2004) 221-6.

[8] A. Lapidus, A. Krylova, Y. Paushkin, J. Rathouský, A. Zukal, J. Stárek. Synthesis of liquid fuels from products of biomass gasification. Fuel. 73 (1994) 583-90.

[9] J.H. Yang, H.J. Kim, D.H. Chun, H.T. Lee, J.C. Hong, H. Jung, et al. Mass transfer limitations on fixed-bed reactor for Fischer-Tropsch synthesis. Fuel Processing Technology. 91 (2010) 285-9.

[10] J.M. Fox. Fischer-Tropsch reactor selection. Catalysis Letters. 7 (1990) 281-92.

[11] J.R. Rostrup-Nielsen. New aspects of syngas production and use. Catalysis Today. 63 (2000) 159-64.

[12] K. Aasberg-Petersen, I. Dybkjær, C.V. Ovesen, N.C. Schjødt, J. Sehested, S.G. Thomsen. Natural gas to synthesis gas - Catalysts and catalytic processes. Journal of Natural Gas Science and Engineering. 3 (2011) 423-59.

[13] I. Wender. Reactions of synthesis gas. Fuel Processing Technology. 48 (1996) 189-297.

[14] D.J. Wilhelm, D.R. Simbeck, A.D. Karp, R.L. Dickenson. Syngas production for gas-to-liquids applications: technologies, issues and outlook. Fuel Processing Technology. 71 (2001) 139-48.

[15] J. Moulijn, M. Makkee, A.v. Diepen. Chemical Process Technology. John Wiley Sons Great Britain, 2001.

[16] S.S. Bharadwaj, L.D. Schmidt. Catalytic partial oxidation of natural gas to syngas. Fuel Processing Technology. 42 (1995) 109-27.

[17] F. Joensen, J.R. Rostrup-Nielsen. Conversion of hydrocarbons and alcohols for fuel cells. Journal of Power Sources. 105 (2002) 195-201.

[18] I. Dybkjaer. Tubular reforming and autothermal reforming of natural gas – an overview of available processes. Fuel Processing Technology. 42 (1995) 85-107.

[19] Ulman's Encyclopedia of Industrial Chemistry. 5th ed. VCH Germany, 1989.

[20] B. Christian Enger, R. Lødeng, A. Holmen. A review of catalytic partial oxidation of methane to synthesis gas with emphasis on reaction mechanisms over transition metal catalysts. Applied Catalysis A: General. 346 (2008) 1-27.

[21] M.W. Smith, D. Shekhawat. Catalytic Partial Oxidation. Fuel Cells: Technologies for Fuel Processing. Elsevier, Amsterdam, 2011. pp. 73-128.

[22] L. Basini, K. Aasberg-Petersen, A. Guarinoni, M. Østberg. Catalytic partial oxidation of natural gas at elevated pressure and low residence time. Catalysis Today. 64 (2001) 9-20.

[23] D.A. Hickman, L.D. Schmidt. Synthesis gas formation by direct oxidation of methane over Pt monoliths. Journal of Catalysis. 138 (1992) 267-82.

[24] D. Hickman, E. Haupfear, L. Schmidt. Synthesis gas formation by direct oxidation of methane over Rh monoliths. Catalysis Letters. 17 (1993) 223-37.

[25] D.A. Hickman, L.D. Schmidt. Production of syngas by direct catalytic oxidation of methane. Science. 259 (1993) 343-6.

[26] D. Dalle Nogare, N.J. Degenstein, R. Horn, P. Canu, L.D. Schmidt. Modeling spatially resolved profiles of methane partial oxidation on a Rh foam catalyst with detailed chemistry. Journal of Catalysis. 258 (2008) 131-42.

[27] D.D. Nogare, N.J. Degenstein, R. Horn, P. Canu, L.D. Schmidt. Modeling spatially resolved data of methane catalytic partial oxidation on Rh foam

catalyst at different inlet compositions and flowrates. Journal of Catalysis. 277 (2011) 134-48.

[28] Z. Ilsen Onsan, A.K. Avci. Reactor Design for Fuel Processing. Fuel Cells: Technologies for Fuel Processing. Elsevier, Amsterdam, 2011. pp. 451-516.

[29] T.S. Christensen, I.I. Primdahl. Hydrogen Processing. (1994) 39-46.

[30] T.S. Christensen, P.S. Christensen, I. Dybkjær, J.H.B. Hansen, I.I. Primdahl. Developments in autothermal reforming. 1998. pp. 883-8.

[31] A.C. Caputo, M. Palumbo, P.M. Pelagagge, F. Scacchia. Economics of biomass energy utilization in combustion and gasification plants: effects of logistic variables. Biomass and Bioenergy. 28 (2005) 35-51.

[32] C. Higman, M.v.d. Burgt. Gasification. 1st ed. Gulf Professional Publishing USA, 2003.

[33] J. Rezaiyan, N.P. Cheremisinoff. Gasification Technologies. 1st ed. CRC Press, USA, 2005.

[34] N.M. Laurendeau. Heterogeneous kinetics of coal char gasification and combustion. Progress in Energy and Combustion Science. 4 (1978) 221-70.

[35] H. Watanabe, M. Otaka. Numerical simulation of coal gasification in entrained flow coal gasifier. Fuel. 85 (2006) 1935-43.

[36] R. Warnecke. Gasification of biomass: comparison of fixed bed and fluidized bed gasifier. Biomass and Bioenergy. 18 (2000) 489-97.

[37] P. McKendry. Energy production from biomass (part 3): gasification technologies. Bioresource Technology. 83 (2002) 55-63.

[38] M. Barrio. Experimental investigation of small-scale gasification of woody biomass. Norwegian University of Science and Technology, Trondheim, 2002.

[39] J. Gil, M.P. Aznar, M.A. Caballero, E. Francés, J. Corella. Biomass gasification in fluidized bed at pilot scale with steam-oxygen mixtures. Product distribution for very different operating conditions. Energy Fuels. 11 (1997) 1109-18.

[40] I. Narvaez, A. Orío, M.P. Aznar, J. Corella. Biomass gasification with air in an atmospheric bubbling fluidized bed. Effect of six operational variables on the quality of the produced raw gas. Industrial Engineering Chemistry Research. 35 (1996) 2110-20.

[41] L. Wei, S. Xu, L. Zhang, C. Liu, H. Zhu, S. Liu. Steam gasification of biomass for hydrogen-rich gas in a free-fall reactor. International Journal of Hydrogen Energy. 32 (2007) 24-31.

[42] K. Umeki, K. Yamamoto, T. Namioka, K. Yoshikawa. High temperature steam-only gasification of woody biomass. Applied Energy. 87 (2010) 791-8.

[43] P. Lv, J. Chang, Z. Xiong, H. Huang, C. Wu, Y. Chen, et al. Biomass Air-Steam Gasification in a Fluidized Bed to Produce Hydrogen-Rich Gas. Energy Fuels. 17 (2003) 677-82.

[44] P. Lv, Z. Yuan, L. Ma, C. Wu, Y. Chen, J. Zhu. Hydrogen-rich gas production from biomass air and oxygen/steam gasification in a downdraft gasifier. Renewable Energy. 32 (2007) 2173-85.

[45] G. Gordillo, K. Annamalai. Adiabatic fixed bed gasification of dairy biomass with air and steam. Fuel. 89 (2010) 384-91.

[46] M. Siedlecki, R. Nieuwstraten, E. Simeone, W.D. Jong, A.H.M. Verkooijen. Effect of magnesite as bed material in a 100 kWth steam-oxygen blown circulating fluidized-bed biomass gasifier on gas composition and tar formation. Energy and Fuels. 23 (2009) 5643-54.

[47] J. Zhou, Q. Chen, H. Zhao, X. Cao, Q. Mei, Z. Luo, et al. Biomass-oxygen gasification in a high-temperature entrained-flow gasifier. Biotechnology Advances. 27 (2009) 606-11.

[48] G.T. Austin. Shreve's Chemical process industries. 5th ed. McGraw-Hill, Singapore, 1984.

[49] A.Y. Starikovskii. Plasma supported combustion. 2005. pp. 2405-17.

[50] M.J. Gallagher Jr, A. Fridman. Plasma Reforming for H_2-Rich Synthesis Gas. Fuel Cells: Technologies for Fuel Processing. Elsevier, Amsterdam, 2011. pp. 223-59.

[51] K. Tsukijihara, K. Okazaki, K. Nozaki. Hydrogen enrichment of low-calorie gas using DBD enhanced Ni/Al_2O_3 catalyst reactor: low-temperature reforming due to radical injection. 17th International symposium on plasma chemistry, Toronto, 2005.

[52] K. Bouamra, N.B. Simiand, F. Jorand, S. Pasquiers, C. Postel. Decomposition of isooctane using a dielectric barrier discharge. 16th International symposium on plasma chemistry, Taormina, 2003.

[53] M.G. Sobacchi, A.V. Saveliev, A.A. Fridman, L.A. Kennedy, S. Ahmed, T. Krause. Experimental assessment of a combined plasma/catalytic system for hydrogen production via partial oxidation of hydrocarbon fuels. International Journal of Hydrogen Energy. 27 (2002) 635-42.

[54] L. Bromberg, D.R. Cohn, A. Rabinovich, N. Alexeev, N. Samokhin, K. Hadidi. On-board plasmatron hydrogen production for improved vehicles. PSFC JA-06-03. (2006).

[55] K. Iskenderova, P. Porshnev, A. Gutsol, A. Saveliev, A. Fridman, L. Kennedy. Methane conversion into syn-gas in gliding arc discharge. 15th International symposium on plasma chemistry, Orleans, 2001.

[56] C.S. Kalra, A.F. Gutsol, A.A. Fridman. Gliding arc discharges as a source of intermediate plasma for methane partial oxidation. IEEE Trans Plasma Sci. 33 (2005).

[57] E.E. Ahmar, C. Met, O. Aubry, A. Khacef, J.M. Cormier. Hydrogen enrichment of a methane-air mixture by atmospheric pressure plasma for vehicle applications. Chemical Engineering Journal. 116 (2006) 13-8.

[58] T. Paulmier, L. Fulcheri. Use of non-thermal plasma for hydrocarbon reforming. Chemical Engineering Journal. 106 (2005) 59-71.

[59] T. Kappes, W. Schiene, T. Hammer. Energy balance of a dielectric barrier discharge for hydrocarbon steam reforming. 8th international symposium of high pressure low temperature plasma chemistry, Pyhajarve, Estonia, 2002.

[60] H. Sekiguchi, Y. Mori. Steam plasma reforming using microwave discharge. Thin Solid Films. 435 (2003) 44-8.

[61] V. Rusanov, A. Babaritskii, E. Gerasimov, M. Deminskii, S. Demkin, V. Zhivotov, et al. Stimulation of the partial oxidation of methane in a microwave discharge. Doklady Physics. 48 (2003) 119-22.

[62] A.I. Babaritskii, I.E. Baranov, M.B. Bibikov, S.A. Demkin, V.K. Zhivotov, G.M. Konovalov, et al. Partial hydrocarbon oxidation processes induced by atmospheric-pressure microwave-discharge plasma. High Energy Chemistry. 38 (2004) 407-11.

[63] Y. Sekine, S. Asai, K. Urasaki, S. Kado, E. Kikuchi, M. Matsukata. Development of liquid fuel reformer using low energy pulse discharge at room temperature. 16th International symposium on plasma chemistry, Taormina, 2003.

[64] L. Bromberg, D.R. Cohn, A. Rabinovich, N. Alexeev. Plasma catalytic reforming of methane. International Journal of Hydrogen Energy. 24 (1999) 1131-7.

[65] F. Ouni, A. Khacef, J.M. Cormier. Methane steam reforming with oxygen in a sliding discharge reactor. 17th International symposium on plasma chemistry, Toronto, 2005.

[66] L. Bromberg, A. Rabinovich. Homogeneous charge compression ignition control by the use of plasmatron fuel converter technology. PSFC/JA- 01-18. (2001).

[67] L. Bromberg, D.R. Cohn, K. Hadidi. Plasmatron reformation of renewable fuels. PSFC/JA-05-03. (2005).

[68] O. Aubry, C. Met, A. Khacef, J.M. Cormier. On the use of a non-thermal plasma reactor for ethanol steam reforming. Chemical Engineering Journal. 106 (2005) 241-7.

[69] A. Czernikowski, M. Czernikowski, K. Wesolowska. Glidarc-assisted production of synthesis gas from rapeseed oil. 1st European hydrogen energy conference, Grenoble, France, 2003.

[70] H. Hocker. Plasma treatment of textile fibers. Pure and Applied Chemistry. 74 (2002) 423-7.

[71] U. Kogelschatz. Dielectric-barrier discharges: Their History, Discharge Physics, and Industrial Applications. Plasma Chemistry and Plasma Processing. 23 (2003) 1-46.

[72] M.J. Gallagher Jr, N. Vaze, S. Gangoli, V.N. Vasilets, A.F. Gutsol, T.N. Milovanova, et al. Rapid inactivation of airborne bacteria using atmospheric pressure dielectric barrier grating discharge. IEEE Transactions on Plasma Science. 35 (2007) 1501-10.

[73] K. Thanyachotpaiboon, S. Chavadej, T.A. Caldwell, L.L. Lobban, R.G. Mallinson. Conversion of methane to higher hydrocarbons in AC nonequilibrium plasmas. AIChE Journal. 44 (1998) 2252-7.

[74] L.M. Zhou, B. Xue, U. Kogelschatz, B. Eliasson. Nonequilibrium plasma reforming of greenhouse gases to synthesis gas. Energy Fuels. 12 (1998) 1191-9.

[75] U. Kogelschatz, L.M. Zhou, B. Xue, B. Eliasson. Greenhouse Gas Control Technologies. Elsevier, Amsterdam, 1999.

[76] K. Okazaki, T.Nozaki. Atmospheric pressure non-equilibrium plasma chemistry by nanosecond high-voltage pulses. Thermal Science and Engineering 7(1999) 109-14.

[77] M. Kraus, B. Eliasson, U. Kogelschatz, A. Wokaun. CO_2 reforming of methane by the combination of dielectric-barrier discharges and catalysis. Physical Chemistry Chemical Physics. 3 (2001) 294-300.

[78] H.K. Song, H. Lee, J.-W. Choi, B.-k. Na. Effect of electrical pulse forms on the CO_2 reforming of methane using atmospheric dielectric barrier discharge. Plasma Chemistry and Plasma Processing. 24 (2004) 57-72.

[79] B. Eliasson, U. Kogelschatz, B. Xue, L.-M. Zhou. Hydrogenation of carbon dioxide to methanol with a discharge-activated catalyst. Industrial Engineering Chemistry Research. 37 (1998) 3350-7.

[80] M.-W. Li, Y.-L. Tian, G.-H. Xu. Characteristics of carbon dioxide reforming of methane via alternating current (AC) corona plasma reactions. Energy Fuels. 21 (2007) 2335-9.

[81] X.-S. Li, C. Shi, Y. Xu, X.-L. Zhang, K.-J. Wang, A.-M. Zhu. Pulsed streamer discharge plasma over Ni/HZSM-5 catalysts for methane conversion to aromatics at atmospheric pressure. Plasma Processes and Polymers. 4 (2007) 15-8.

[82] T. Nozaki, N. Muto, S. Kado, K. Okazaki. Dissociation of vibrationally excited methane on Ni catalyst: Part 1. Application to methane steam reforming. Catalysis Today. 89 (2004) 57-65.

[83] T. Nozaki, N. Muto, S. Kadio, K. Okazaki. Dissociation of vibrationally excited methane on Ni catalyst: Part 2. Process diagnostics by emission spectroscopy. Catalysis Today. 89 (2004) 67-74.

[84] B. Pietruszka, K. Anklam, M. Heintze. Plasma-assisted partial oxidation of methane to synthesis gas in a dielectric barrier discharge. Applied Catalysis A: General. 261 (2004) 19-24.

[85] T. Kappesa, W. Schiene, T. Hammer. Energy balance of a dielectric barrier discharge reactor for hydrocarbon steam reforming. 18th International Symposium on High Pressure, Low Temperature Plasma Chemistry 2002.

[86] S. Masuda. Pulse corona induced plasma chemical process: a horizon of new plasma chemical technologies. Pure Appl Chem. 60 (1988) 727-31.

[87] A. Schutze, J.Y. Jeong, S.E. Babayan, P. Jaeyoung, G.S. Selwyn, R.F. Hicks. The atmospheric-pressure plasma jet: a review and comparison to other plasma sources. Plasma Science, IEEE Transactions on. 26 (1998) 1685-94.

[88] A. Fridman, A. Chirokov, A. Gutsol. Non-thermal atmospheric pressure discharges Journal of Physics D: Applied Physics. 38 (2005) R1-R24.

[89] M. Wolf, Y. Yankelevich, A. Pokryvailo, R.B. Baksht, S. Singer. Modeling of a Streamer Plasma Reactor Energized by a Pulse Compression Modulator. Plasma Science, IEEE Transactions on. 38 (2010) 2793-8.

[90] M. Moisan, G. Sauve, Z. Zakrzewski, J. Hubert. An atmospheric pressure waveguide-fed microwave plasma torch: the TIA design. Plasma Sources Science and Technology. 3 (1994) 584-92.

[91] K.M. Green, M.C. Borras, P.P. Woskov, G.J. Flores, III, K. Hadidi, P. Thomas. Electronic excitation temperature profiles in an air microwave plasma torch. Plasma Science, IEEE Transactions on. 29 (2001) 399-406.

[92] H. Nowakowska, M. Jasinski, J. Mizeraczyk. Electromagnetic field distributions in waveguide-based axial-type microwave plasma source. The European Physical Journal D - Atomic, Molecular, Optical and Plasma Physics. 54 (2009) 511-8.

[93] J.D. Rollier, J. Gonzalez-Aguilar, G. Petitpas, A. Darmon, L. Fulcheri, R. Metkemeijer. Experimental study on gasoline reforming assisted by nonthermal arc discharge. Energy and Fuels. 22 (2008) 556-60.

[94] S. Delagrange, L. Pinard, J.-M. Tatibouët. Combination of a non-thermal plasma and a catalyst for toluene removal from air: Manganese based oxide catalysts. Applied Catalysis B: Environmental. 68 (2006) 92-8.

[95] T. Nozaki, T. Hiroyuki, K. Okazaki. Hydrogen Enrichment of Low-Calorific Fuels Using Barrier Discharge Enhanced Ni/Al_2O_3 Bed Reactor: Thermal and Nonthermal Effect of Nonequilibrium Plasma. Energy Fuels. 20 (2005) 339-45.

[96] H.L. Chen, H.M. Lee, S.H. Chen, Y. Chao, M.B. Chang. Review of plasma catalysis on hydrocarbon reforming for hydrogen production-Interaction, integration, and prospects. Applied Catalysis B: Environmental. 85 (2008) 1-9.

[97] L. Bromberg, D.R. Cohn, A. Rabinovich, J.E. Surma, J. Virden. Compact plasmatron-boosted hydrogen generation technology for vehicular applications. International Journal of Hydrogen Energy. 24 (1999) 341-50.

[98] Y. Chao, C.T. Huang, H.M. Lee, M.B. Chang. Hydrogen production via partial oxidation of methane with plasma-assisted catalysis. International Journal of Hydrogen Energy. 33 (2008) 664-71.

[99] R.F. Horng, H.H. Huang, M.P. Lai, C.S. Wen, W.C. Chiu. Characteristics of hydrogen production by a plasma-catalyst hybrid converter with energy saving schemes under atmospheric pressure. International Journal of Hydrogen Energy. 33 (2008) 3719-27.

[100] R. Marques, S. Da Costa, P. Da Costa. Plasma-assisted catalytic oxidation of methane. On the influence of plasma energy deposition and feed composition. Applied Catalysis B: Environmental. 82 (2008) 50-7.

[101] K. Tao, N. Ohta, G. Liu, Y. Yoneyama, T. Wang, N. Tsubaki. Plasma enhanced catalytic reforming of biomass tar model compound to syngas. Fuel. In Press, Corrected Proof (2010).

[102] J.G. Speight. Hydrocarbons from Synthesis Gas. Handbook of Industrial Hydrocarbon Processes. Gulf Professional Publishing, Boston, 2011. pp. 281-323.

[103] H. Schulz. Short history and present trends of Fischer-Tropsch synthesis. Applied Catalysis A: General. 186 (1999) 3-12.

[104] M.E. Dry. The Fischer-Tropsch process: 1950-2000. Catalysis Today. 71 (2002) 227-41.

[105] R. Guettel, U. Kunz, T. Turek. Reactors for Fischer-Tropsch Synthesis. Chemical Engineering Technology. 31 (2008) 746-54.

[106] B.H. Davis. Fischer-Tropsch synthesis: Overview of reactor development and future potentialities. Topics in Catalysis. 32 (2005) 143-68.

[107] E. Iglesia, S.C. Reyes, R.J. Madon, S.L. Soled. Adv. Catal. 39. Academic Press, New York 1993.

[108] H. Schulz, M. Claeys. Kinetic modelling of Fischer-Tropsch product distributions. Applied Catalysis A: General. 186 (1999) 91-107.

[109] R. Oukaci, A.H. Singleton, J.G. Goodwin. Comparison of patented Co F-T catalysts using fixed-bed and slurry bubble column reactors. Applied Catalysis A: General. 186 (1999) 129-44.

[110] M.E. Dry. Catalytic aspects of industrial Fischer-Tropsch synthesis. Journal of Molecular Catalysis. 17 (1982) 133-44.

[111] S.T. Sie. Process development and scale up: IV. Case history of the development of a Fischer-Tropsch synthesis process. Rev Chem Eng. 14 (1998) 109-57.

[112] R. Krishna, S.T. Sie. Design and scale-up of the Fischer-Tropsch bubble column slurry reactor. Fuel Processing Technology. 64 (2000) 73-105.

[113] R.L. Espinoza, A.P. Steynberg, B. Jager, A.C. Vosloo. Low temperature Fischer-Tropsch synthesis from a Sasol perspective. Applied Catalysis A: General. 186 (1999) 13-26.

[114] R. Krishna. A scale-up strategy for a commercial scale bubble column slurry reactor for Fischer-Tropsch synthesis. Oil Gas Science and Technology - Rev IFP. 55 (2000) 359-93.

[115] R. Krishna, J.M. van Baten. A Strategy for Scaling Up the Fischer-Tropsch Bubble Column Slurry Reactor. Topics in Catalysis. 26 (2003) 21-8.

[116] M.N. Kashid, A. Renken, L. Kiwi-Minsker. Gas-liquid and liquid-liquid mass transfer in microstructured reactors. Chemical Engineering Science. 66 (2011) 3876-97.

[117] Y.H. Chin, J. Hu, C. Cao, Y. Gao, Y. Wang. Preparation of a novel structured catalyst based on aligned carbon nanotube arrays for a microchannel Fischer-Tropsch synthesis reactor. Catalysis Today. 110 (2005) 47-52.

[118] J. Knochen, R. Güttel, C. Knobloch, T. Turek. Fischer-Tropsch synthesis in milli-structured fixed-bed reactors: Experimental study and scale-up considerations. Chemical Engineering and Processing: Process Intensification. 49 (2010) 958-64.

[119] D. Schanke, E. Bergene, A. Holmen. International Patent Number WO9838147. 1998.

[120] L. Guillou, D. Balloy, P. Supiot, V. Le Courtois. Preparation of a multilayered composite catalyst for Fischer-Tropsch synthesis in a micro-chamber reactor. Applied Catalysis A: General. 324 (2007) 42-51.

[121] Y. Wang. International Patent Number WO2005075606. 2005.

[122] T. Boger, A.K. Heibel. Heat transfer in conductive monolith structures. Chemical Engineering Science. 60 (2005) 1823-35.

[123] M.P. Rohde, D. Unruh, G. Schaub. Membrane application in Fischer-Tropsch synthesis reactors–Overview of concepts. Catalysis Today. 106 (2005) 143-8.

[124] M.A. Marvast, M. Sohrabi, S. Zarrinpashne, G. Baghmisheh. Fischer-Tropsch synthesis: Modeling and performance study for Fe-HZSM5 bifunctional catalyst. Chemical Engineering and Technology. 28 (2005) 78-86.

[125] R. Philippe, M. Lacroix, L. Dreibine, C. Pham-Huu, D. Edouard, S. Savin, et al. Effect of structure and thermal properties of a Fischer-Tropsch catalyst in a fixed bed. Catalysis Today. 147 (2009) S305-S12.

[126] B.W. Wojciechowski. Kinetics of the Fischer-Tropsch synthesis. Catalysis reviews. 30 (1988) 629-702.

[127] G.F. Froment, K.B. Bischoff. Chemical Reactor Analysis and Design. 2nd ed. J.Wiley and Sons, New York, 1990.

[128] D.G. Loffler, L.D. Schmidt. Catalytic activity and selectivity on heterogeneous surfaces with mass transfer. AIChE Journal. 21 (1975) 786-91.

[129] S.T. Kolaczkowski. Modelling catalytic combustion in monolith reactors - challenges faced. Catalysis Today. 47 (1999) 209-18.

[130] L.D. Pfefferle. Heterogeneous/homogeneous reactions and transport coupling for catalytic combustion systems: a review of model alternatives. Catalysis Today. 26 (1995) 255-65.

[131] L.L. Raja, R.J. Kee, O. Deutschmann, J. Warnatz, L. D. Schmidt. A critical evaluation of Navier-Stokes, boundary-layer, and plug-flow models of the flow and chemistry in a catalytic-combustion monolith. Catalysis Today. 59 (2000) 47-60.

[132] M.H. Rafiq, J.E. Hustad. Biosyngas production by autothermal reforming of waste cooking oil with propane using a plasma-assisted gliding arc reactor. International Journal of Hydrogen Energy. 36 (2011) 8221-33.

[133] R.C. Ramaswamy, P.A. Ramachandran, M.P. Dudukovic. Modeling Catalytic Partial Oxidation of Methane to Syngas in Short-Contact-Time Packed-Bed Reactors. Industrial Engineering Chemistry Research. 46 (2007) 8638-51.

[134] M. Minutillo. On-board fuel processor modelling for hydrogen-enriched gasoline fuelled engine. International Journal of Hydrogen Energy. 30 (2005) 1483-90.

[135] M.S. Benilov, G.V. Naidis. Modeling of hydrogen-rich gas production by plasma reforming of hydrocarbon fuels. International Journal of Hydrogen Energy. 31 (2006) 769-74.

[136] R.C. Reid, J.M. Prausnitz, B.E. Poling. The Properties of Gases and Liquids 4th ed. McGraw-Hill, New York 1988.

[137] A.L. Lydersen. Fluid Flow and Heat Transfer. John Wiley and Sons, New York 1979.

[138] J. Xu, G.F. Froment. Methane steam reforming, methanation and water-gas shift: I. Intrinsic kinetics. AIChE Journal. 35 (1989) 88-96.

[139] J. Xu, G.F. Froment. Methane steam reforming: II. Diffusional limitations and reactor simulation. AIChE Journal. 35 (1989) 97-103.

[140] E.L. Cussler. Diffusion: mass transfer in fluid systems. Cambridge University Press 1984.

[141] S.H. Skaare. Reaction and heat transfer in a wall-cooled fixed bed reactor. Norwegian University of Science and Technology, Trondheim, 1993.

[142] J.D. Rollier, J. Gonzalez-Aguilar, G. Petitpas, A. Darmon, L. Fulcheri, R. Metkemeijer. Experimental study on gasoline reforming assisted by nonthermal arc discharge. Energy and Fuels. 22 (2008) 556-60.

[143] R. Mungen, M.B. Kratzer. Partial combustion of methane with oxygen Ind Eng Chem. 43 (1951) 2782.

[144] E.P.J. Mallens, J.H.B.J. Hoebink, G.B. Marin. The reaction mechanism of the partial oxidation of methane to synthesis gas: A transient kinetic study over rhodium and a comparison with platinum. Journal of Catalysis. 167 (1997) 43-56.

[145] J. Zhu, D. Zhang, K.D. King. Reforming of CH_4 by partial oxidation: Thermodynamic and kinetic analyses. Fuel. 80 (2001) 899-905.

[146] J.R. Rostrup-Nielsen. Syngas in perspective. Catalysis Today. 71 (2002) 243-7.

[147] M.J. Gallagher, R. Geiger, A. Polevich, A. Rabinovich, A. Gutsol, A. Fridman. On-board plasma-assisted conversion of heavy hydrocarbons into synthesis gas. Fuel. 89 (2010) 1187-92.

[148] P.B. Weisz, C.D. Prater. Interpretation of Measurements in Experimental Catalysis. 6 (1954) 143-96.

[149] D.E. Mears. Tests for transport limitations in experimental catalytic reactors. Industrial and Engineering Chemistry: Process Design and Development. 10 (1971) 541-7.

[150] B.r.C. Enger, R.L. Lødeng, A. Holmen. Modified cobalt catalysts in the partial oxidation of methane at moderate temperatures. Journal of Catalysis. 262 (2009) 188-98.

[151] M. Bizzi, L. Basini, G. Saracco, V. Specchia. Short contact time catalytic partial oxidation of methane: Analysis of transport phenomena effects. Chemical Engineering Journal. 90 (2002) 97-106.

[152] M. Prettre, C. Eichner, M. Perrin. The catalytic oxidation of methane to carbon monoxide and hydrogen. Transactions of the Faraday Society. 43 (1946) 6.

[153] W.J.M. Vermeiren, E. Blomsma, P.A. Jacobs. Catalytic and thermodynamic approach of the oxyreforming reaction of methane. Catalysis Today. 13 (1992) 427-36.

[154] C.R.H. de Smet, M.H.J.M. de Croon, R.J. Berger, G.B. Marin, J.C. Schouten. Design of adiabatic fixed-bed reactors for the partial oxidation of methane to synthesis gas. Application to production of methanol and hydrogen-for-fuel-cells. Chemical Engineering Science. 56 (2001) 4849-61.

[155] R.B. Anderson. The Fischer-Tropsch synthesis. Academic Press, Orlando,FL, 1984.

[156] T. Riedel, M. Claeys, H. Schulz, G. Schaub, S.S. Nam, K.W. Jun, et al. Comparative study of Fischer-Tropsch synthesis with H_2/CO and H_2/CO_2 syngas using Fe- and Co-based catalysts. Applied Catalysis A: General. 186 (1999) 201-13.

[157] T. Riedel, G. Schaub. Low-temperature Fischer-Tropsch synthesis on cobalt catalysts effects of CO_2. Topics in Catalysis. 26 (2003) 145-56.

[158] D. Xu, H. Duan, W. Li, H. Xu. Investigation on the Fischer-Tropsch synthesis with nitrogen-containing syngas over $CoPtZrO_2/Al_2O_3$ catalyst. Energy and Fuels. 20 (2006) 955-8.

[159] A.K. Dalai, B.H. Davis. Fischer-Tropsch synthesis: A review of water effects on the performances of unsupported and supported Co catalysts. Applied Catalysis A: General. 348 (2008) 1-15.

[160] V.A. de la Pena OShea, J.M. Campos-Martín, J.L.G. Fierro. Strong enhancement of the Fischer-Tropsch synthesis on a Co/SiO_2 catalyst activate in syngas mixture. Catalysis Communications. 5 (2004) 635-8.

[161] R.C. Everson, H. Mulder. Fischer-Tropsch reaction Studies with supported ruthenium catalysts .III. The production of alkenes and high molecular weight hydrocarbons in a fixed bed reactor. Journal of Catalysis. 143 (1993) 166-74.

[162] A. Sari, Y. Zamani, S.A. Taheri. Intrinsic kinetics of Fischer-Tropsch reactions over an industrial Co-Ru/γ-Al_2O_3 catalyst in slurry phase reactor. Fuel Processing Technology. 90 (2009) 1305-13.

[163] E. Iglesia, S.C. Reyes, R.J. Madon. Transport-enhanced α-olefin readsorption pathways in Ru-catalyzed hydrocarbon synthesis. Journal of Catalysis. 129 (1991) 238-56.

[164] E. Rytter, S. Eri, T.H. Skagseth, D. Schanke, E. Bergene, R. Myrstad, et al. Catalyst particle size of cobalt/rhenium on porous alumina and the effect on

Fischer - Tropsch catalytic performance. Industrial and Engineering Chemistry Research. 46 (2007) 9032-6.

[165] S. Krishnamoorthy, M. Tu, M.P. Ojeda, D. Pinna, E. Iglesia. An investigation of the effects of water on rate and selectivity for the Fischer-Tropsch synthesis on cobalt-based catalysts. Journal of Catalysis. 211 (2002) 422-33.

[166] A.A. Adesina. Hydrocarbon synthesis via Fischer-Tropsch reaction: Travails and triumphs. Applied Catalysis A: General. 138 (1996) 345-67.

[167] J. Xu, W. Wei, A. Tian, Y. Fan, X. Bao, C. Yu. Temperature profile in a two-stage fixed bed reactor for catalytic partial oxidation of methane to syngas. Catalysis Today. 149 (2010) 191-5.

[168] M. Huff, L.D. Schmidt. Production of olefins by oxidative dehydrogenation of propane and butane over monoliths at short contact times. Journal of Catalysis. 149 (1994) 127-41.

[169] G.A. Nahar. Hydrogen rich gas production by the autothermal reforming of biodiesel (FAME) for utilization in the solid-oxide fuel cells: A thermodynamic analysis. International Journal of Hydrogen Energy. 35 (2010) 8891-911.

[170] P. Kolbitsch, C. Pfeifer, H. Hofbauer. Catalytic steam reforming of model biogas. Fuel. 87 (2008) 701-6.

[171] J. Gonzalez-Aguilar, G. Petitpas, A. Lebouvier, J.-D. Rollier, A. Darmon, L. Fulcheri. Three stages modeling of n-octane reforming assisted by a nonthermal arc discharge. Energy Fuels. 23 (2009) 4931-6.

[172] H. Long, S. Shang, X. Tao, Y. Yin, X. Dai. CO_2 reforming of CH_4 by combination of cold plasma jet and Ni/Al_2O_3 catalyst. International Journal of Hydrogen Energy. 33 (2008) 5510-5.

[173] A. Indarto, J.-W. Choi, H. Lee, H.K. Song. Effect of additive gases on methane conversion using gliding arc discharge. Energy. 31 (2006) 2986-95.

Appendix A

List of papers

PAPER A

Synthesis Gas from Methane by Using a Plasma-Assisted Gliding Arc Catalytic Partial Oxidation Reactor

M.H. Rafiq[a], J.E. Hustad[a]

[a] Department of Energy and Process Engineering,

Norwegian University of Science and Technology, Kolbjorn Hejes v 1B,

7491 Trondheim, Norway.

This paper is published in Industrial Engineering Chemistry Research, Volume 50, Issue 9, May 2011, Pages 5428-5439.

Is not included due to copyright

PAPER B

Modeling and Simulation of Catalytic Partial Oxidation of Methane to Synthesis Gas by Using a Plasma-Assisted Gliding Arc Reactor

M.H. Rafiq[a], H.A. Jakobsen[b], J.E. Hustad[a]

[a] Department of Energy and Process Engineering,

Norwegian University of Science and Technology (NTNU),

N-7491 Trondheim, Norway.

[b] Department of Chemical Engineering,

Norwegian University of Science and Technology (NTNU),

N-7491 Trondheim, Norway.

This paper is submitted to Fuel Processing Technology.

Is not included due to copyright

PAPER C

Experimental Studies and Modeling of a Fixed Bed Reactor for Fischer−Tropsch Synthesis Using Biosyngas

M.H. Rafiq[a], H.A. Jakobsen[b], R. Schmid[c], J.E. Hustad[a]

[a] Department of Energy and Process Engineering,

Norwegian University of Science and Technology (NTNU),

N-7491 Trondheim, Norway.

[b] Department of Chemical Engineering,

Norwegian University of Science and Technology (NTNU),

N-7491 Trondheim, Norway.

[c] Department of Chemistry,

Norwegian University of Science and Technology (NTNU),

N-7491 Trondheim, Norway.

This paper is published in Fuel Processing Technology, Volume 92, Issue 5, May 2011, Pages 893-907.

Is not included due to copyright

PAPER D

Biosyngas Production by Autothermal Reforming of Waste Cooking Oil with Propane Using a Plasma-Assisted Gliding Arc Reactor

M.H. Rafiq[a], J.E. Hustad[a]

[a] Department of Energy and Process Engineering,

Norwegian University of Science and Technology (NTNU),

N-7491 Trondheim, Norway.

This paper is published in International Journal of Hydrogen Energy, Volume 36, Issue 14, July 2011, Pages 8221-8233.

Is not included due to copyright

PAPER E

Experimental and Thermodynamic Studies of the Catalytic Partial Oxidation of Model Biogas Using a Plasma-Assisted Gliding Arc Reactor

M.H. Rafiq[a], J.E. Hustad[a]

[a] Department of Energy and Process Engineering,

Norwegian University of Science and Technology, Kolbjorn Hejes v 1B,

7491 Trondheim, Norway.

This paper is published in Renewable Energy, Volume 36, Issue 11, November 2011, Pages 2878-2887.

Is not included due to copyright